

**WATER- AND CO₂-BASED OIL RECOVERY PROCESSES IN THE
TIGHT MAIN PAY ZONE AND VUGGY RESIDUAL OIL ZONE**

A Thesis

Submitted to the Faculty of Graduate Studies and Research

In Partial Fulfillment of the Requirements for the

Degree of Master of Applied Science in

Petroleum Systems Engineering

University of Regina

by

Yanbin Gong

Regina, Saskatchewan

April 2015

© Copyright 2015: Yanbin Gong

UNIVERSITY OF REGINA
FACULTY OF GRADUATE STUDIES AND RESEARCH
SUPERVISORY AND EXAMINING COMMITTEE

Yanbin Gong, candidate for the degree of Master of Applied Science in Petroleum Systems Engineering, has presented a thesis titled, ***Water- and CO₂-Based Oil Recovery Processes in the Tight Main Pay Zone and Vuggy Residual Oil Zone***, in an oral examination held on December 5, 2014. The following committee members have found the thesis acceptable in form and content, and that the candidate demonstrated satisfactory knowledge of the subject material.

External Examiner: Dr. Hussameldin Ibrahim, Industrial Systems Engineering

Supervisor: Dr. Yongan Gu, Petroleum Systems Engineering

Committee Member: Dr. Fashid Torabi, Petroleum Systems Engineering

Committee Member: Dr. Fanhua Zeng, Petroleum Systems Engineering

Chair of Defense: Dr. Zhou Zhang, Faculty of Business Administration

ABSTRACT

In this thesis, water- and CO₂-based flooding processes in the upper tight main pay zone (MPZ) and in the lower vuggy residual oil zone (ROZ) of a carbonate light oil reservoir were studied and compared. In particular, the oil recovery performance of miscible CO₂ simultaneous water-and-gas (CO₂-SWAG) injection in the tight Bakken formation was experimentally examined.

More specifically, first, several carbonate reservoir rock samples from the MPZ and ROZ in the Steelman oilfield (Canada) were characterized by using thin-section analysis and X-ray diffraction (XRD). Second, the minimum miscibility pressure (MMP) between the light crude oil and CO₂ at the actual reservoir temperature was determined by applying the vanishing interfacial tension (VIT) technique. Third, a total of ten coreflood tests were conducted with the tight dolostone or vuggy limestone core plugs to evaluate the effects of the production pressure, rock properties, and CO₂ injection timing on the water- and CO₂-based oil recovery processes in the two different zones. Then the effective viscosities of high-salinity water and supercritical CO₂ mixtures with twelve different water volume fractions were measured at the actual reservoir conditions by using a capillary viscometer. Finally, six more coreflood tests were carried out with different CO₂-EOR schemes and different injected water–gas ratios (WGRs) in volume to determine the optimum miscible CO₂-SWAG injection in the tight Bakken formation.

The MMP between the light crude oil and CO₂ at the actual reservoir temperature of $T_{\text{res}} = 51.1$ °C was determined to be 10.8 MPa. The coreflood test results showed that for the CO₂ secondary flooding in the non-waterflooded tight MPZ, the oil recovery factor (RF) increased almost linearly with the production pressure, whether it was lower or

higher than the MMP. For the CO₂ flooding in the waterflooded vuggy ROZ, however, much less residual oil was recovered in the immiscible case than that in the miscible case, especially after CO₂ breakthrough (BT). Moreover, the petrographic properties of these two types of core plugs had rather different effects on the miscible CO₂ secondary flooding, whereas the miscible CO₂ tertiary flooding had similar production trends in the two zones. In comparison with waterflooding or miscible CO₂ secondary flooding alone, waterflooding and miscible CO₂ tertiary flooding together were the most effective method to recover the light crude oil from the upper tight MPZ and lower vuggy ROZ of the carbonate reservoir.

In addition, it was found that the measured effective viscosity of the saline water–CO₂ mixture was increased with the water volume fraction and can be well modelled by using the Arrhenius equation. In the tight Bakken formation, the miscible CO₂-SWAG injection with an injected WGR of 1:3 in volume achieved the highest oil RF, in comparison with miscible CO₂ secondary flooding, waterflooding together with miscible CO₂ tertiary flooding, and miscible CO₂ water-alternating-gas (CO₂-WAG) injection. The WGR also showed strong effects on the fluid production trends and the oil RF of the miscible CO₂-SWAG injection. A water bank might be formed ahead of the water–CO₂ mixture in the miscible CO₂-SWAG injection with a higher injected WGR of 1:1 or 3:1. Furthermore, the calculated mobility ratios of the injected fluids to the light crude oil indicated that in comparison with water or CO₂ alone, the water–CO₂ mixture had the lowest mobility in the tight reservoir core plugs. Hence, the highest oil RF of the optimum CO₂-SWAG injection with the injected WGR of 1:3 was attributed to a substantially weakened waterblocking effect and a well-controlled CO₂ mobility.

ACKNOWLEDGMENTS

I wish to acknowledge the following individuals and organizations:

- Dr. Yongan (Peter) Gu, my academic advisor, for his excellent guidance, valuable advice, strong support, and continuous encouragement throughout the course of this thesis study;
- My past and present research group members, Mr. Zeya Li, Mr. Lixing Lin, Mr. Pengcheng Hou, Mr. Longyu Han, Mr. Hongze Ma, Ms. Fengshuang Du, and Mr. Kaiqiang Zhang, for their useful technical discussions and assistance during my Master's program;
- My thesis defense committee members: Dr. Hussameldin Ibrahim, Dr. Farshid Torabi, Dr. Fanhua (Bill) Zeng, and Dr. Zhou Zhang;
- Petroleum Technology Research Centre (PTRC) for the Innovation Fund to Dr. Yongan (Peter) Gu;
- Natural Sciences and Engineering Research Council (NSERC) of Canada for the discovery grant to Dr. Yongan (Peter) Gu; and
- Faculty of Graduate Studies and Research (FGSR) at the University of Regina for awarding the Graduate Student Scholarships.

DEDICATION

This thesis is dedicated to my beloved parents, Weitao Gong and Hongju Li,
for their unconditional love, constant support, and timely encouragement.

TABLE OF CONTENTS

ABSTRACT.....	ii
ACKNOWLEDGMENTS	iv
DEDICATION.....	v
TABLE OF CONTENTS.....	vi
LIST OF TABLES	ix
LIST OF FIGURES	x
NOMENCLATURE	xv
CHAPTER 1 INTRODUCTION.....	1
1.1 Waterflooding and CO ₂ -Based Enhanced Oil Recovery Processes	1
1.2 CO ₂ -EOR in a Carbonate Reservoir with an Underlying Vuggy ROZ.....	2
1.3 CO ₂ -SWAG Injection in a Tight MPZ.....	5
1.4 Purpose of the Thesis Study	8
1.5 Scope of the Thesis Study	8
1.6 Outline of the Thesis	9
CHAPTER 2 LITERATURE REVIEW.....	11
2.1 CO ₂ -Based EOR Processes in the MPZ	11
2.2 CO ₂ -Based EOR Processes in the ROZ	13
2.3 CO ₂ -EOR Mechanisms	15
2.4 Pressure Effect on CO ₂ -EOR Process	17

2.5 SWAG Injection	20
2.5.1 Laboratory studies.....	20
2.5.2 Numerical simulations	24
2.5.3 Pilot tests.....	24
2.6 Problem Statement	26
CHAPTER 3 EXPERIMENTAL	29
3.1 Materials.....	29
3.2 Thin-Section Analysis of Rock Samples.....	33
3.3 XRD Evaluation of Rock Samples.....	33
3.4 Oil Density Measurement.....	34
3.5 Oil Viscosity Measurement.....	34
3.6 Interfacial Tension Measurements	35
3.7 Oil-Swelling Effect and Ligh-HCs Extraction by CO ₂	38
3.8 Effective Viscosity Measurements.....	38
3.9 Coreflood Tests	42
CHAPTER 4 RESULTS AND DISCUSSION	50
4.1 Petrographic and Mineralogical Properties	50
4.2 Mutual Interactions Between the Light Crude Oil and CO ₂	54
4.2.1 Measured equilibrium IFTs and MMP	54
4.2.2 Oil-swelling effect and light-HCs extraction phenomenon	56

4.3 CO ₂ -EOR in a Tight MPZ and in a Vuggy ROZ	60
4.3.1 Production pressure effect	60
4.3.2 Permeability and vug effects	70
4.3.3 Miscible CO ₂ secondary/tertiary flooding.....	73
4.4 Miscible CO ₂ -SWAG Injection in a Tight MPZ.....	77
4.4.1 Effective viscosities of the saline water–CO ₂ mixtures.....	77
4.4.2 Three CO ₂ -EOR processes	80
4.4.3 WGR effects	87
4.4.4 Mobilities of water, CO ₂ , and water–CO ₂ mixtures	92
4.4.5 Oil RFs.....	96
CHAPTER 5 CONCLUSIONS AND RECOMMENDATIONS	99
5.1 Conclusions	99
5.2 Recommendations	102
REFERENCES	104
APPENDIX A.....	116
APPENDIX B	119

LIST OF TABLES

<p>Table 3.1 Compositional analysis result of the cleaned Steelman original light crude oil ($\rho_o = 0.819 \text{ g/cm}^3$, $\mu_o = 0.76 \text{ cP}$ at the atmospheric pressure and $T_{\text{res}} = 51.1 \text{ }^\circ\text{C}$, $MW_{\text{oil}} = 188.8 \text{ g/mol}$, Well No.: 3-29-3-4W2) with the asphaltene content of $w_{\text{asp}} = 0.15 \text{ wt.}\%$ (<i>n</i>-pentane insoluble).....</p>	31
<p>Table 3.2 Physical and chemical properties of the cleaned Steelman reservoir brine at $P = 1 \text{ atm}$ (Well No.: 3-29-3-4W2).....</p>	32
<p>Table 4.1 (a) Petrographic properties of five Steelman rock samples.....</p>	51
<p>Table 4.1 (b) Mineralogical properties of five Steelman rock samples.....</p>	51
<p>Table 4.2 Physical properties of the composite carbonate reservoir core plugs from the Steelman oilfield, experimental conditions, oil recovery factors of ten CO_2-based coreflood tests at $q_{\text{brine}} = 0.025 \text{ cm}^3/\text{min}$, $q_{\text{CO}_2} = 0.1 \text{ cm}^3/\text{min}$, $T_{\text{res}} = 51.1 \text{ }^\circ\text{C}$, and the MMP = 10.8 MPa.</p>	61
<p>Table 4.3 Physical properties of the composite reservoir core plugs collected from the Tatagwa oilfield, experimental conditions, oil recovery factors of six water- and CO_2-based coreflood tests at $q_{\text{mix}} = 0.1 \text{ cm}^3/\text{min}$, $P_{\text{prod}} = 15.0 \text{ MPa}$, and $T_{\text{res}} = 51.1 \text{ }^\circ\text{C}$.....</p>	81

LIST OF FIGURES

Figure 2.1	(a) A simple model system for diffusion of CO ₂ through a water-barrier phase; and (b) CO ₂ concentration profiles in the simple model system [Grogan and Pinczewski, 1987].	18
Figure 2.2	Snapshots of fluid distribution within a micro-model of (a) Continuous gas injection; (b) SWAG injection with a gas volume fraction of 0.2; and (c) SWAG injection with a gas volume fraction of 0.5 [Sohrabi <i>et al.</i> , 2008].	21
Figure 3.1	Schematic diagram of the experimental set-up used for measuring the equilibrium interfacial tension (IFT) between the light crude oil and CO ₂ by applying the axisymmetric drop shape analysis (ADSA) technique for the pendant drop case.	36
Figure 3.2	Schematic diagram of the high-pressure capillary viscometer used for measuring the effective viscosity (μ_{mix}) of each water–CO ₂ mixture.....	40
Figure 3.3	Schematic diagram of the high-pressure CO ₂ -based coreflood apparatus..	43
Figure 3.4	Calculated isothermal compressibility and density of CO ₂ versus the pressure data at the reservoir temperature of $T_{\text{res}} = 51.1$ °C by using the CMG WinProp module.	49
Figure 4.1	(a) Digital photograph of two rock samples from the Midale layer (tight core plug) and the Frobisher layer (vuggy core plug); (b) Photomicrograph of the tight rock sample with pin-point vugs; (c) Photomicrograph of the vuggy rock sample with a vug; and (d) Photomicrograph of the vuggy rock sample with a natural fracture.	52

Figure 4.2	Measured equilibrium interfacial tensions (IFTs) between the Steelman light crude oil and CO ₂ at different equilibrium pressures and $T_{res} = 51.1$ °C.	55
Figure 4.3	Sequential digital images of the Steelman crude oil pendant drops surrounded by CO ₂ at (a) $P_{eq} = 4.1$ MPa during the initial oil-swelling process (e.g., at $t = 0, 850$ s) and the subsequent slow light-hydrocarbons (HCs) extraction process (e.g., at $t = 900, 3,600$ s); (b) $P_{eq} = 7.5$ MPa during the initial almost constant-volume stage (e.g., at $t = 0, 100$ s) and the subsequent slow light-HCs extraction process (e.g., at $t = 130, 3,600$ s)...	57
Figure 4.4	Sequential digital images of the initial and quick light-hydrocarbons (HCs) extraction by the supercritical CO ₂ ($P_{eq} = MMP = 10.8$ MPa and $T_{res} = 51.1$ °C) at different times.	59
Figure 4.5	(a) Measured oil RFs of CO ₂ secondary flooding versus the PV of injected CO ₂ in Tests #1–4 with the tight core plugs.....	62
Figure 4.5	(b) Measured final oil RFs of CO ₂ secondary flooding in terms of the OOIP versus the production pressure at $P_{prod} = 2.0$ MPa (Test #1), 6.5 MPa (Test #2), 11.0 MPa (Test #3), and 14.0 MPa (Test #4) with the tight core plugs.	63
Figure 4.6	(a) Measured oil RFs, gas production rates (q_g), and cumulative water production data (Q_w) versus the PV of injected brine and CO ₂ in Test #8 (waterflooding + immiscible CO ₂ tertiary flooding) with the vuggy core plugs at $P_{prod} = 6.5$ MPa.	65

Figure 4.6	(b) Measured oil RFs, gas production rates (q_g), and cumulative water production data (Q_w) versus the PV of injected brine and CO ₂ in Test #9 (waterflooding + miscible CO ₂ tertiary flooding) with the vuggy core plugs at $P_{\text{prod}} = 11.0$ MPa.	66
Figure 4.6	(c) Measured oil RFs, gas production rates (q_g), and cumulative water production data (Q_w) versus the PV of injected brine and CO ₂ in Test #10 (waterflooding + miscible CO ₂ tertiary flooding) with the vuggy core plugs at $P_{\text{prod}} = 14.0$ MPa.	67
Figure 4.6	(d) Measured total oil RFs of waterflooding and CO ₂ tertiary flooding in terms of the OOIP, oil RFs of CO ₂ tertiary flooding in terms of the ROIP, and oil RFs of CO ₂ tertiary flooding after CO ₂ -BT in terms of the ROIP versus the production pressure at $P_{\text{prod}} = 6.5$ MPa (Test #8), 11.0 MPa (Test #9), and 14.0 MPa (Test #10) with the vuggy core plugs.	69
Figure 4.7	Measured oil RFs of CO ₂ secondary flooding versus the PV of injected CO ₂ in Test #3 ($k = 0.086$ mD for the tight core plugs and $P_{\text{prod}} = 11.0$ MPa), Test #5 ($k = 0.019$ mD for the tight core plugs and $P_{\text{prod}} = 9.0$ MPa), and Test #7 ($k = 6.631$ mD for the vuggy core plugs and $P_{\text{prod}} = 11.0$ MPa), as well as measured gas production rates (q_g) versus the PV of injected CO ₂ in Tests #3 and #5.	71
Figure 4.8	Measured oil RFs and gas production rates (q_g) versus the PV of injected CO ₂ in Test #3 (miscible CO ₂ secondary flooding) and injected brine and CO ₂ in Test #6 (waterflooding + miscible CO ₂ tertiary flooding) with the	

tight core plugs at $P_{\text{prod}} = 11.0$ MPa, as well as measured cumulative water production data (Q_w) versus the PV of injected brine and CO₂ in Test #6. 74

Figure 4.9 Measured oil RFs versus the PV of injected CO₂ in Test #7 (miscible CO₂ secondary flooding) and injected brine + CO₂ in Test #9 (waterflooding + miscible CO₂ tertiary flooding) with the vuggy core plugs at $P_{\text{prod}} = 11.0$ MPa. 76

Figure 4.10 Measured and predicted effective viscosities (μ_{mix}) of the water–CO₂ mixtures at twelve increasing water volume fractions (ϕ_{brine}) at $P = 15.0$ MPa and $T_{\text{res}} = 51.1$ °C..... 78

Figure 4.11 Measured oil RFs and average gas production rates (q_g) versus the PVs of injected CO₂ in Test #11 (miscible CO₂ secondary flooding)..... 82

Figure 4.12 Measured oil RFs, average gas production rates (q_g), and cumulative water production data (Q_w) versus the PVs of injected brine and CO₂ in Test #12 (waterflooding followed by miscible CO₂ tertiary flooding). 83

Figure 4.13 Measured oil RFs, average gas production rates (q_g), and cumulative water production data (Q_w) versus the PVs of injected brine and CO₂ in Test #13 (miscible CO₂-WAG injection with a slug size of 0.222 PV and a slug ratio of 1:3). 84

Figure 4.14 (a) Measured oil RFs, average gas production rates (q_g), and cumulative water production data (Q_w) versus the PVs of injected brine and CO₂ in Test #14 (miscible CO₂-SWAG injection with the injected WGR of 1:3 in volume)..... 88

Figure 4.14 (b)	Measured oil RFs, average gas production rates (q_g), and cumulative water production data (Q_w) versus the PVs of injected brine and CO ₂ in Test #15 (miscible CO ₂ -SWAG injection with the injected WGR of 1:1 in volume).....	89
Figure 4.14 (c)	Measured oil RFs, average gas production rates (q_g), and cumulative water production data (Q_w) versus the PVs of injected brine and CO ₂ in Test #16 (miscible CO ₂ -SWAG injection with the injected WGR of 3:1 in volume).....	90
Figure 4.15	Measured pressure drops (ΔP) between the inlet and outlet of the coreholder versus the PVs of injected CO ₂ in Test #11 (miscible CO ₂ secondary flooding) or injected brine + CO ₂ in Test #12 (waterflooding followed by miscible CO ₂ tertiary flooding), Test #13 (miscible CO ₂ -WAG injection), and Tests #14–16 (miscible CO ₂ -SWAG injection).	93
Figure 4.16	Mobility ratios (M) of injected CO ₂ to oil in Test #11 (miscible CO ₂ secondary flooding) and Test #12 (miscible CO ₂ tertiary flooding); injected water–CO ₂ mixtures to oil in Test #14 (miscible CO ₂ -SWAG injection with the injected WGR = 1:3), Test #15 (miscible CO ₂ -SWAG injection with the injected WGR = 1:1), and Test #16 (miscible CO ₂ -SWAG injection with the injected WGR = 3:1); and injected water to oil in Test #12 (waterflooding).....	95
Figure 4.17	Comparison of the measured oil RFs in six coreflood tests, each of which used the same amount of 2.0 PV of injected CO ₂	97

NOMENCLATURE

Notations

A	Cross-sectional area of the composite reservoir core plugs, cm^2
f_g	Gas volume fraction
k	Permeability, mD
k'_o	End-point effective permeability to the light crude oil, mD
k'_f	End-point effective permeability to the injected fluid(s), mD
L	Length, cm
M	Mobility ratio
MW_{oil}	Molecular weight of the light crude oil, g/mol
P_{eq}	Equilibrium pressure, MPa
P_{inj}	Initial CO_2 injection pressure at the inlet of coreholder, MPa
P_{max}	First-contact miscibility pressure, MPa
P_{prod}	Production pressure at the outlet of coreholder, MPa
q_{brine}	Brine injection rate, cm^3/min
q_{CO_2}	CO_2 injection rate, cm^3/min
q_g	Gas production rate, cm^3/min
q_{mix}	Total injection rate of the saline water– CO_2 mixture, cm^3/min
Q_w	Cumulative water production, cm^3
R^2	Correlation coefficient
r_{eff}	Effective radius of the capillary tubing, cm
RF_{CO_2}	Oil recovery factor of CO_2 flooding, %
RF_{total}	Oil recovery factor of waterflooding and CO_2 tertiary flooding, %

RF_w	Oil recovery factor of waterflooding, %
S_{oi}	Initial oil saturation, %
S_{or}	Residual oil saturation, %
t	Time, s
T_{lab}	Laboratory ambient temperature, °C
T_{res}	Reservoir temperature, °C
V	Volume of pendant oil drop, mm ³
w_{asp}	Asphaltene content of the light crude oil, wt. %

Greek letters

γ_{eq}	Equilibrium interfacial tension between the light crude oil and CO ₂ , mJ/m ²
ΔP	Pressure drop between the inlet and outlet of the coreholder, kPa
ΔP_{ave}	Average steady-state pressure drop between the inlet and outlet of the coreholder, kPa
λ_f	Apparent mobility of the injected fluid(s), D·cP ⁻¹
λ_o	Mobility of the light crude oil, D·cP ⁻¹
μ_{mix}	Effective viscosity of the water–CO ₂ mixture, cP
μ_o	Viscosity of the light crude oil, cP
μ_f	Effective viscosity of the injected fluid(s), cP
ρ_o	Density of the light crude oil, g/cm ³
ϕ	Porosity, %

Superscript

' Effective

Subscripts

a Apparent

asp Asphaltene

ave Average

brine Brine

CO₂ Carbon dioxide

eff Effective

eq Equilibrium

f Fluid

g Gas

inj Injection

lab Laboratory

max Maximum

mix Water–CO₂ mixture

oi Initial oil

oil Crude oil

or Residual oil

prod Production

r Relative

res Reservoir

total Total

w Water

Acronyms

atm	Atmospheric pressure
ADSA	Axisymmetric drop shape analysis
API	American Petroleum Institute
ASTM	American Society for Testing and Materials
BHP	Bottom-hole pressure
BPR	Back-pressure regulator
BT	Breakthrough
CGI	Continuous gas injection
CGOR	Cumulative gas–oil ratio
CMG	Computer Modelling Group
CWI	Carbonated water injection
CWOR	Cumulative water–oil ratio
EOR	Enhanced oil recovery
EOS	Equation of state
FCM	First-contact miscibility
FGSR	Faculty of Graduate Studies and Research
GOR	Gas–oil ratio
HCPV	Hydrocarbon pore volume
HCs	Hydrocarbons
IFT	Interfacial tension
MCM	Multi-contact miscibility
MMP	Minimum miscibility pressure

MPZ	Main pay zone
MW	Molecular weight
NSERC	Natural Sciences and Engineering Research Council
OIP	Oil-in-place
OOIP	Original oil-in-place
OWC	Oil–water contact
P–R	Peng–Robinson
PTRC	Petroleum Technology Research Centre
PV	Pore volume
RF	Recovery factor
ROIP	Residual oil-in-place
ROZ	Residual oil zone
SRC	Saskatchewan Research Council
SWAG	Simultaneous water-and-gas
TDS	Total dissolved solids
TIFF	Tagged image file format
TZ	Transition zone
VIT	Vanishing interfacial tension
WAG	Water-alternating-gas
WGR	Water–gas ratio
WOR	Water–oil ratio
XRD	X-ray diffraction

CHAPTER 1 INTRODUCTION

1.1 Waterflooding and CO₂-Based Enhanced Oil Recovery Processes

Since the first accident in the 1890s that occurred due to improperly plugged wells and corroded casings, waterflooding has long become the most widely applied secondary oil recovery process to improve the oil recovery [Willhite, 1986]. The major oil recovery mechanism of waterflooding is voidage replacement or volumetric displacement by injecting water to maintain the reservoir pressure and displace the crude oil from the pore space. With a high capillary pressure between water and the crude oil, however, the oil recovery factor (RF) of waterflooding is usually rather low. In a typical light or medium oil reservoir, the residual oil saturation after the secondary waterflooding can be in the range of 50–60% of the original oil-in-place (OOIP) [Moritis, 2006]. On the other hand, CO₂ flooding has been studied as an important enhanced oil recovery (EOR) method since the 1950s. Over six decades of development and practice, CO₂ flooding has become a leading EOR method. By 2012, a total of 129 CO₂-EOR projects were conducted in USA and Canada [Kuuskraa, 2012]. In CO₂ flooding process, the oil recovery can be further increased through miscible or immiscible displacement, interfacial tension (IFT) reduction, light-hydrocarbons (HCs) extraction, oil-swelling effect, oil viscosity reduction, and possible asphaltene precipitation [Green and Willhite, 1998; Wang and Gu, 2011]. Moreover, CO₂-EOR projects not only effectively recover the residual crude oil but also considerably reduce the greenhouse gas emissions. Based on the field production data from the CO₂-EOR projects in USA, it is estimated that up to 60% of the injected

CO₂ can be stored in a depleted oil reservoir if reinjection of CO₂ is not accounted for. [Gozalpour *et al.*, 2005].

1.2 CO₂-EOR in a Carbonate Reservoir with an Underlying Vuggy ROZ

Approximately 60% of the oil reserves worldwide are found in the carbonate reservoirs [Akbar *et al.*, 2000]. Unfortunately, most carbonate oil reservoirs are highly heterogeneous in terms of their diverse reservoir characteristics, such as porosity and permeability. At least fifteen basic porosity types are found and classified for the carbonate rocks, which can co-exist in many cases [Choquette and Pray, 1970]. Many naturally fractured reservoirs and vuggy carbonate reservoirs are known as dual-porosity reservoirs with the primary porosity and the secondary porosity, the latter of which is generated during a long and complex diagenetic process. With various porosity types, rock textures, and mineral compositions in different zones, a carbonate reservoir can have large permeability variations [Dou *et al.*, 2011]. For example, the Mississippian Midale formation in the Midale–Steelman oilfield of Southeastern Saskatchewan (Canada) consists of the low-permeability Marly zone above the high-permeability Vuggy zone [McDow and Kent, 1993]. The Marly zone is an earthy-appearing dolostone dominated by intercrystalline porosity, whereas the Vuggy zone is a limestone that has vuggy, moldic, fenestral, interparticle and intraparticle porosity. In general, these complicated lithological characteristics result in a low oil recovery factor (RF) in the carbonate oil reservoir. A number of enhanced oil recovery (EOR) techniques, such as CO₂ flooding, chemical flooding, and steam flooding, have been studied and developed to achieve the best oil recovery in the carbonate reservoirs. In particular, CO₂ flooding has been proven to be an effective oil recovery method through some laboratory studies [Hamouda and

Alipour Tabrizy, 2013] and numerical simulations [Brinkman and Kane, 1999]. Also CO₂ flooding has been applied as the dominant EOR process in the carbonate reservoirs since the 1980s in USA [Moritis, 2004]. In Canada, four of the six CO₂-EOR projects were conducted in the carbonate formations in 2012 [Kuuskraa, 2012].

With relatively low critical properties, CO₂ and its interaction with the reservoir fluids (i.e., CO₂-EOR mechanisms) are greatly affected by the operating pressure and CO₂ flooding scheme. Depending on the operating pressure, a CO₂ displacement process in a reservoir formation can be either miscible or immiscible. In the miscible CO₂ flooding process, CO₂ is injected at a reservoir pressure that is equal to or higher than the minimum miscibility pressure (MMP). Thus the miscibility is developed in the oil reservoir through in-situ oil and gas compositional changes, which are resulted from multi-contact mass transfer between the reservoir oil and the injected CO₂ [Green and Willhite, 1998]. In the laboratory studies, miscible CO₂ flooding can recover more than 90% of the original oil-in-place (OOIP) in the slim-tube test [Wu and Batycky, 1990]. Immiscible CO₂ flooding is considered as an alternative to miscible CO₂ flooding when the reservoir pressure is below the MMP at the reservoir temperature. In this case, the oil recovery is mainly attributed to the IFT reduction, oil-swelling effect, and oil viscosity reduction [Bargas *et al.*, 1992; Rojas and Farouq Ali, 1988]. From economic and operational points of view, low-pressure CO₂ flooding is more attractive as long as a reasonable oil RF can be achieved because less CO₂ is needed and CO₂ compression cost is lower. In the miscible or immiscible CO₂ flooding process, nevertheless, a low volumetric sweep efficiency is always a concern due to an extremely low viscosity and a relatively low density of CO₂ in comparison with those of the other reservoir fluids [Orr

et al., 1982]. Waterflooding, as an economical secondary oil recovery method, has been commonly combined with CO₂ flooding to effectively reduce the mobility of CO₂ and control its viscous fingering [Juanes and Blunt, 2007].

More recently, CO₂-EOR also emerges as a viable and effective technology for recovering the stranded light crude oil in the lower residual oil zones (ROZs) of the carbonate reservoirs, in addition to their upper main pay zones (MPZs). By definition, the ROZs can represent either waterflooded intervals of the MPZ (man-made ROZs) or the middle and lower portions of an oil reservoir below the oil–water contact (OWC), the latter of which are waterflooded by nature in a geological time (nature-created ROZs) [Melzer *et al.*, 2006]. Due to low to moderate residual oil saturations, nevertheless, the oil resources in the ROZs are uneconomical or ineffective to recover through the primary production or waterflooding alone. In fact, CO₂ flooding may be effective to recover the water-shielded residual oil in the ROZ through CO₂ dispersion process and oil-swelling effect [Do and Pinczewski, 1993].

Many man-made or nature-created ROZs of the carbonate reservoirs are under relatively tight MPZs. In the waterflooded Midale formation, for example, the injected water tends to pass through the lower high-permeability Vuggy zone and leave the upper low-permeability Marly zone almost untouched [Dong *et al.*, 2002]. In the nature-created ROZs below the OWC, porosity and permeability are gradually increased in a geological time. Both laboratory and field studies have shown that the zone sequence or layout in this kind of carbonate reservoirs provides a favourable scenario for CO₂ flooding to fully take advantage of CO₂ gravity overriding and concurrently recover the untouched original oil in the upper tight MPZ and the stranded residual oil in the lower vuggy ROZ

[Dong *et al.*, 2002; Beliveau and Payne, 1991]. However, the geological characteristics, fluid properties and saturations, and fluid flow patterns in these two zones are rather different. Moreover, the oil recovery processes of CO₂-based EOR methods in the tight MPZ with an ultra-low permeability and especially in the vuggy ROZ with a much higher permeability are neither well studied nor fully differentiated. It is also expected that the high-permeability vugs and natural fractures in the vuggy ROZ can lead to an early CO₂ breakthrough (BT) and a low oil RF. In order to achieve the maximum total oil recovery from both the upper tight MPZ and the lower vuggy ROZ, it is of fundamental and practical importance to better understand how the production conditions, CO₂ flooding schemes, and rock properties affect the actual performance of CO₂-EOR in each zone.

1.3 CO₂-SWAG Injection in a Tight MPZ

Several CO₂-based EOR processes have been developed in order to effectively control CO₂ mobility and increase the sweep efficiency of CO₂ flooding. These CO₂-based EOR processes include carbonated water injection (CWI), CO₂ cyclic solvent injection (CO₂-CSI), and CO₂ water-alternating-gas (CO₂-WAG) injection. In the CWI process, CO₂ is dissolved into the water phase prior to its injection. As a result, the mobility of the displacing phase (i.e., the carbonated water) is greatly reduced by eliminating the gas phase. In this process, finite oil recovery is achieved mainly through water volumetric displacement, oil swelling and viscosity reduction due to limited CO₂ dissolution. With a minimal CO₂ consumption, this EOR method is particularly attractive for the oilfields with little access to CO₂ source [Riazi *et al.*, 2011]. Nevertheless, the CWI performance is considerably compromised because of a low CO₂ solubility in water phase, especially in the deep reservoir brine with a high salinity. In CO₂-CSI, CO₂

injection period is followed by a shut-in or soaking period, during which CO₂ phase can be further dissolved into the crude oil before the oil production period starts. Gas molecular diffusion and oil viscosity reduction play important roles in the oil recovery process. This EOR method can be successfully applied in the oil reservoirs with poor inter-well connectivity [Zhang *et al.*, 2006]. In the CO₂-WAG injection, the flooding front is stabilized by injecting small water and CO₂ slugs alternately. The water injection process improves the volumetric sweep efficiency, whereas the CO₂ injection process enhances the microscopic displacement efficiency [Kulkarni and Rao, 2005]. In the field applications, however, a large amount of the residual oil is still left behind after CO₂-WAG injection in the oil reservoir. Moderately enhanced oil RFs in the range of 5–10% of the OOIP are obtained for the successful CO₂-WAG projects [Christensen *et al.*, 2001]. In comparison with continuous CO₂ flooding, CO₂-WAG injection requires more parameters (e.g., slug size and ratio) to be optimized and may cause some operational problems due to frequent water–gas alternation.

Laboratory studies and pilot tests have shown that the oil RF can be increased by reducing the slug size of a CO₂-WAG injection [Han and Gu, 2014; Robie *et al.*, 1995]. In this regard, CO₂ simultaneous water-and-gas (CO₂-SWAG) injection can be considered as a modified or special CO₂-WAG injection, in which water and CO₂ are co-injected simultaneously rather than alternately. By means of co-injecting CO₂ with more viscous water, it is anticipated that CO₂ mobility is substantially reduced due to the CO₂ effective permeability reduction and water–CO₂ mixture viscosity increase [Caudle and Dyes, 1958]. Furthermore, it is well known that the performance of CO₂-WAG injection is strongly dependent on the slug ratio [Chen *et al.*, 2010]. Similarly, the water–CO₂ ratio

of the co-injected water–CO₂ mixture in CO₂-SWAG injection is expected to have a strong effect on its oil recovery process. Here, the co-injected water–gas ratio (WGR) is defined as the volume ratio of injected water phase to co-injected CO₂ phase under the actual reservoir conditions. If the WGR is too high, the excessive water phase may block the crude oil from being contacted by CO₂ phase directly and prevent the multi-contact miscibility development [Tiffin and Yellig, 1983]. On the other hand, if the WGR is too low or a large amount of CO₂ is injected, CO₂ mobility control by co-injected water may not be effective enough and an early CO₂-BT can occur.

Caudle and Dyes [1958] conducted the first SWAG injection study in the lab in 1958. Their laboratory test results showed that for a five-spot flooding model, the ultimate sweep efficiency was increased from about 60% for continuous gas flooding to about 90% for SWAG injection. More recently, Sohrabi *et al.* [2008] conducted visualization tests to compare the displacement efficiency of near-miscible continuous methane (CH₄) injection and that of CH₄-SWAG injection. They concluded that the oil RF of CH₄-SWAG injection was almost the same as that of continuous CH₄ injection, whereas the methane consumption for CH₄-SWAG was much lower. Aleidan and Mamora [2010] carried out three coreflood tests of miscible CO₂-SWAG injection in carbonate core plugs with an average permeability of $k = 90$ mD. It was found that the CO₂-SWAG injection resulted in a higher oil RF than continuous CO₂ flooding or CO₂-WAG injection. In the field scale, few applications of CO₂-SWAG injection have been reported. In the Joffre Viking pool (Canada), CO₂-WAG injection offered little improvement on CO₂ flooding. On the other hand, a CO₂-SWAG injection pilot project showed the best sweep efficiency and the highest oil RF, in comparison with continuous CO₂ flooding and CO₂-WAG

injection [Stephenson *et al.*, 1993]. Higher oil recovery and more stabilized water and gas production were also experienced for CO₂-SWAG injection field trial in the Rangely Weber oilfield, Colorado, USA, in comparison with CO₂-WAG injection [Robie *et al.*, 1995].

Although CO₂-SWAG injection provides more stabilized water and gas production and better CO₂ mobility control than CO₂-WAG injection [Heidari *et al.*, 2013a], no laboratory tests have been conducted to study its performance and explore its potential for recovering the light crude oil in a tight oil formation. Moreover, in consideration of the adverse and beneficial effects of the injected water flow on the overall performance of a CO₂-SWAG injection process, it is necessary to identify an optimum WGR in order to achieve the best oil recovery under given reservoir conditions.

1.4 Purpose of the Thesis Study

The primary purpose of the thesis study is to compare water- and CO₂-based oil recovery processes in the tight main pay zone (MPZ) and in the vuggy residual oil zone (ROZ) and examine the effects of some major flooding parameters on the oil recovery process. Furthermore, the potential of conducting the miscible CO₂ simultaneous water-and-gas (CO₂-SWAG) injection in the tight MPZ is to be explored.

1.5 Scope of the Thesis Study

The following research tasks are conceived in the scope of the thesis study in order to meet its research objectives:

- 1) To measure the equilibrium interfacial tensions (IFTs) between a light crude oil–CO₂ system by applying the axisymmetric drop shape analysis (ADSA) technique for the

- pendant drop case and determine its minimum miscibility pressure (MMP) by using the vanishing interfacial tension (VIT) technique;
- 2) To analyze the oil-swelling effect and initial quick light-hydrocarbons (HCs) extraction from the light crude oil to CO₂ phase;
 - 3) To conduct a series of water- and CO₂-based coreflood tests at four different production pressures ($P_{\text{prod}} = 2.0, 6.5, 11.0, \text{ and } 14.0 \text{ MPa}$) with different CO₂ injection timings (i.e, with or without waterflooding prior to CO₂ flooding) and two kinds of carbonate reservoir core plugs and evaluate different CO₂-based oil recovery processes in the tight MPZ and in vuggy ROZ;
 - 4) To measure the effective viscosities of high-salinity water–CO₂ mixtures with different water volume fractions from 0 (i.e, pure CO₂) to 1 (i.e., pure brine) at the actual reservoir pressure and temperature by using a high-pressure capillary tubing; and
 - 5) To carry out a series of coreflood tests with different injection schemes (i.e., miscible CO₂ secondary flooding, waterflooding followed by miscible CO₂ tertiary flooding, CO₂-WAG injection, and CO₂-SWAG injection with different injected water–gas ratios in volume) and examine the oil recovery potential, average gas production rate, cumulative water production, and mobilities of the injection fluids of CO₂-SWAG injection in the tight MPZ.

1.6 Outline of the Thesis

This thesis is composed of five chapters. More specifically, Chapter 1 is an introduction to the thesis topic together with the purpose and scope of this thesis. Chapter 2 provides an updated literature review on CO₂-based EOR processes in the MPZ and

ROZ, CO₂-EOR mechanisms in these two zones, pressure effect on a CO₂ flooding process, and the SWAG injection. Chapter 3 describes the experimental setups and experimental procedures for the oil density and viscosity measurements, IFT measurement tests, and coreflood tests. In Chapter 4, first, the petrographic and mineralogical properties of different rock samples collected from the MPZ and ROZ of a carbonate reservoir are presented. Second, the mutual interactions between the light crude oil and CO₂, including IFT measurement, MMP determination, and visualizations of the oil swelling and light-HCs extraction, are described. Third, different CO₂-EOR processes in a tight MPZ and a vuggy ROZ are compared and discussed. Last, the effective viscosities of water–CO₂ mixtures with different water volume fractions, miscible CO₂-SWAG injection versus continuous CO₂ flooding or CO₂-WAG injection, and the WGR effects on the oil recovery process of the miscible CO₂-SWAG injection in a tight MPZ, are analyzed. Chapter 5 summarizes the major scientific findings of this study and makes several technical recommendations for future studies.

CHAPTER 2 LITERATURE REVIEW

2.1 CO₂-Based EOR Processes in the MPZ

Carbon Dioxide flooding has been studied as an EOR method since the 1950s. Its first commercial project was operated in 1972 at the SACROC oilfield, West Texas [Crameik and Plassey, 1972]. Many other projects have been conducted since then and in 2012, a total of 129 CO₂-EOR projects were ongoing in USA and Canada [Kuuskraa, 2012]. In particular, CO₂-based EOR has become a leading EOR technique for light and medium oil reservoirs, where miscibility can be easily achieved under the reservoir pressure [Espie, 2005]. In the past four decades, several major EOR processes have been developed, such as CO₂-CGI, CO₂-WAG injection, CO₂-SWAG injection, CWI, CO₂-CSI, and chemical assisted CO₂-EOR.

With a simple injection system, CO₂-CGI is especially suitable for the reservoirs that either have a minimized gravity segregation problem when CO₂ is injected or have detrimental effects when water injection is applied [Poole, 1988; Bellavance, 1996]. In the laboratory study, the miscible CO₂-CGI could recover about 80% of the OOIP from the tight MPZ [Wang and Gu, 2011]. The CO₂-WAG method is commonly employed in the commercial gas injection projects since it combines a higher microscopic displacement efficiency of gas displacement with a better macroscopic sweep efficiency of waterflooding [Kulkarni and Rao, 2005]. Therefore, CO₂-WAG injection is usually conducted with the purposes of reducing the mobility of CO₂ and controlling its viscous fingering [Juanes and Blunt, 2007]. Its performance is largely affected by the injection parameters (e.g., slug size and slug ratio) and production parameters (e.g., production pressure) [Chen et al., 2010]. For the field applications, an increased oil RF about 5–10%

of the OOIP is common for the successful CO₂-WAG processes [Christensen *et al.*, 2001]. Similarly, CO₂-SWAG injection is another EOR method that uses water to control the mobility of CO₂ phase. It is a process, in which water and CO₂ are co-injected simultaneously, instead of injecting water and CO₂ alternately. CO₂-SWAG injection seems more challenging than CO₂-WAG injection. The increased monitoring of the injection system and reduced injectivity are the two major technical concerns for its field application [Awan *et al.*, 2008]. In CWI process, CO₂ is pre-dissolved into the water phase and injected into an oil reservoir together with water as a single phase. In comparison with that of CGI or WAG injection, the mobility ratio between the carbonated water and oil is more favorable by eliminating the gas phase [Sohrabi *et al.*, 2012]. The oil-swelling effect and oil viscosity reduction through CO₂ diffusion are the two major oil recovery mechanisms in CWI process [Riazi *et al.*, 2011]. In addition to oil recovery, the CO₂ storage potential of CWI was also discussed by Sohrabi *et al.* [2012]. In CO₂-CSI or CO₂ huff-n-puff, CO₂ injection is followed by a shut-in or soaking period. Monger and Coma [1988] conducted CO₂-CSI laboratory tests and evaluated 14 oilfield tests in Louisiana, USA. They concluded that the soaking period was required to increase the oil RF but the correlation between the production performance and soaking duration was weak. Other laboratory studies proved that CO₂-CSI is an effective EOR method for both tight and naturally fractured reservoirs [Song and Yang, 2013; Asghari and Torabi, 2007]. Extensive studies have also been carried out to explore chemical assisted CO₂-EOR process, such as surfactant-stabilized CO₂ and polymer-thickened CO₂ [Kim *et al.*, 2005; Zhang *et al.*, 2011]. Effective CO₂ mobility control was reported in these studies.

More recently, novel techniques are proposed to improve the performance of CO₂-EOR. Nanoparticle-stabilized CO₂ foam, for instance, is studied based on new technologies developed in nano-science. In the nanoparticle-stabilized CO₂ foam, nanoparticles, instead of surfactant, were used to generate and stabilize the CO₂ foam [Espinoza *et al.*, 2010; Aroonsri *et al.*, 2013]. The thermodynamical instability of surfactant-stabilized CO₂ foam system is expected to be eliminated in the nanoparticle-stabilized emulsions [Yu *et al.*, 2012]. This technology is still in its testing stage and no field application is implemented to date.

2.2 CO₂-Based EOR Processes in the ROZ

Over decades, waterflooding has been the most commonly used secondary oil recovery method to recover the crude oil and maintain the reservoir pressure. The low oil displacement efficiency and reservoir heterogeneities, however, usually result in a significant quantity of the residual crude oil left behind in the reservoir after waterflooding [Grattoni and Dawe, 2002]. In a typical light or medium oil reservoir, the residual oil saturation after the primary and secondary production is still in the range of 50–60% of the OOIP [Moritis, 2006]. After years of development, many reservoirs have already reached their economic limit for oil production through waterflooding alone [Warner Jr., 1977; Pyo *et al.*, 2003]. The waterflooded layers in these reservoirs are known as the ROZs. In addition to this kind of man-made ROZs, the ROZs can also represent the middle and lower portions of the reservoir below the traditional OWC, which are waterflooded by nature in a geological time (nature-created ROZs) [Melzer *et al.*, 2006]. In the basal portion of each oil reservoir, there is an interval of ROZ or transition zone (TZ) where the oil saturation falls rapidly. This TZ is controlled by the

capillary pressure. Instead of these thin capillary-pressure based TZs, the nature-created ROZs studied in this thesis are the non-capillary origin and much thicker ROZs. In the study of Melzer *et al.*, they listed three origins of these nature-created ROZs: regional or local basin tilt, breached and reformed seals, and altered hydrodynamic flow fields. These ROZs can be extensive and have large amounts of the residual oil. In USA, it is estimated that the oil-in-place (OIP) in the ROZs is about 140 billion barrels [Kuuskraa *et al.*, 2013].

In the field-wide ROZs, the residual oil saturations of 20–40% are common and the most possible oil saturations are in the range of 28–32% [Honarpour *et al.*, 2010]. Through CO₂ diffusion process and oil-swelling effect, CO₂ flooding has emerged as a viable EOR technique to recover these stranded but significant oil resources [Do and Pinczewski, 1993; Koperna *et al.*, 2006]. In Alberta, Canada, the Joffre Viking pool, which was discovered in 1953, was unitized in 1957 to initiate waterflooding. By the mid 1970s, 42% of the OOIP had been recovered through the primary and secondary waterflooding processes and the pool reached its economic limit of waterflooding. Since 1984, miscible CO₂ flooding has been conducted and progressively expanded in this man-made ROZ. A final oil RF about 16% of the OOIP was achieved by successfully applying CO₂ tertiary flooding process [Pyo *et al.*, 2003]. In USA, three CO₂-EOR projects are under way in the nature-created ROZs of the Permian Basin, West Texas. They are conducted in the Denver Unit of the Wason Field (300 feet ROZ with a dominant oil saturation above 30%), the San Andres Unit of the Seminole Field (197 feet ROZ with an oil saturation of 32%), and the Bennett Ranch Unit of the Wason Field (75 feet ROZ) [Melzer *et al.*, 2006].

2.3 CO₂-EOR Mechanisms

The major CO₂-EOR mechanisms include miscible or immiscible displacement, IFT reduction, light-HCs extraction, oil-swelling effect, oil viscosity reduction, and possible asphaltene precipitation [Green and Willhite, 1998; Wang and Gu, 2011]. In comparison with hydrocarbon solvent, CO₂ can be miscible with the crude oil at a relatively low pressure. As an excellent EOR agent, CO₂ is also highly soluble in the crude oil above certain pressure. It can expand the volume of the crude oil by 10–60% and reduce its viscosity by 5 to 10 folds [Holm, 1982].

The ability to extract HCs from the crude oil is the most important characteristic of CO₂ [Holm and Josendal, 1974]. It is also the principal mechanism in the multi-contact miscibility development process of CO₂-EOR. Many laboratory studies have been done to investigate CO₂ extraction ability. Wang [1986] studied the extraction processes of CO₂ with three different crude oil samples (17°, 41°, and 45°API) at elevated pressures and different temperatures. It was found that CO₂ could extract the HCs up to C₃₆, though most HCs were in the range of C₅–C₂₀. The extraction process was more active in the lighter crude oil with more light to intermediate HCs. CO₂ extraction ability was also found to be increased with the increased pressure and decreased temperature. Shyeh-Yung [1991] conducted some slim-tube tests and coreflood tests to analyze the miscible and near-miscible CO₂ flooding mechanisms. It was concluded that the extraction process started from lower molecular weight (MW) HCs and gradually advanced to heavier HCs in the displacement process. After gas BT, HCs extraction by CO₂ became the dominant oil recovery mechanism. Nevertheless, this process requires a large amount of CO₂. Siagian and Grigg [1998] performed an extended CO₂ extraction test by using a light

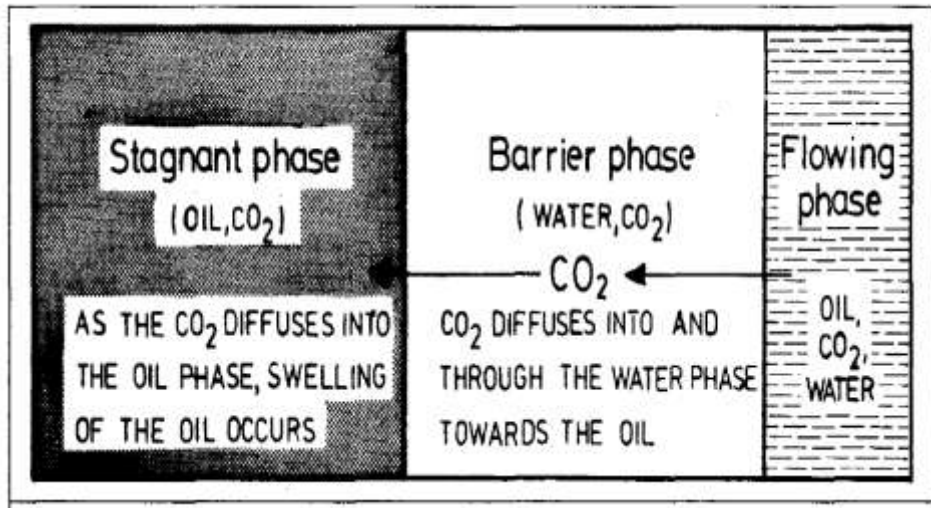
crude oil sample (40°API). The MMP between the light crude oil and CO₂ was measured to be 1100 psi at 95 °F. The test was conducted at 1200 psi and 95 °F. After 103 hours of CO₂ injection, 64 wt.% or 70 vol.% oil was extracted and produced by CO₂. The extraction ability was decreased from about 0.3 g oil/g CO₂ at the beginning to 0.005 g oil/g CO₂ at the time of termination.

Different from the MPZs, the ROZs have high water saturations and the residual oil is usually shielded by water. The water phase will block the residual oil from being directly contacted by the injected CO₂ phase and prevent the miscibility development [Tiffin and Yellig, 1983]. Besides oil-swelling and HCs extraction effects, CO₂ molecular diffusion also plays an important role in CO₂-EOR in the ROZs [Huang and Tracht, 1974; Grogan and Princzewski, 1987]. Huang and Tracht [1974] conducted phase behaviour tests of the West Texas crude oil (36°API) and CO₂ system, as well as CO₂ flooding tests in the waterflooded Berea core plugs with the permeabilities of $k = 440$ and 470 mD. The coreflood tests were conducted under reservoir conditions of 1250 psi and 90 °F. They concluded that in CO₂ flooding process, CO₂ displaced and dissolved into the mobile water phase. Simultaneously, CO₂ diffused into and swelled the initial immobile residual oil. The portion of the swollen oil in excess of the residual oil saturation then became mobile and continuously extracted by CO₂. This diffusion, swelling, and extraction processes continued until a CO₂-riched oil phase, which was miscible with CO₂, was formed. Grogan and Princzewski [1987] built a 1-D numerical model to further study the role of CO₂ molecular diffusion in the residual oil recovery process. In their model, it was assumed that a trapped oil phase was separated from a flowing CO₂ phase by an initially stagnant water-barrier phase. CO₂ diffusion caused the CO₂ concentration to increase

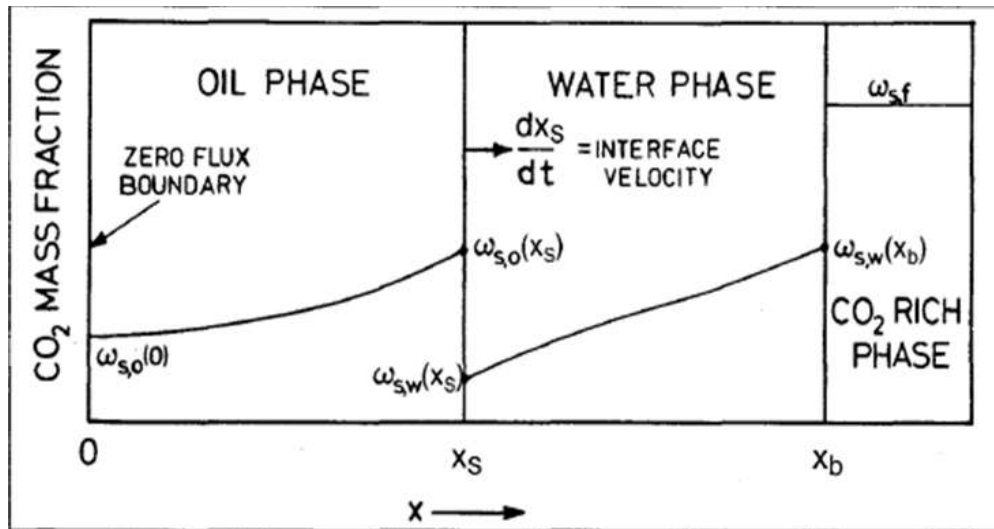
with time in both the water and oil phases. The swelling of the trapped oil caused the movements of the oil–water and water–CO₂ boundaries. All the water that crossed the initial water–CO₂ boundary was removed by the CO₂ flux. Eventually, all the water-barrier phase was moved away and then the residual oil could directly contact the CO₂ phase. Their model system and CO₂ concentration profiles are shown in Figures 2.1 a and b. Results from the lab coreflood tests were used to validate their model. It was concluded that CO₂ molecular diffusion was important for the residual oil recovery at the pore scale and a sufficiently long contact time was needed in order for the CO₂ diffusion and oil-swelling processes to take place.

2.4 Pressure Effect on CO₂-EOR Process

For a CO₂ flooding process, its EOR mechanisms are greatly affected by the operating pressure. Under a different operating pressure, a CO₂ displacement process in a reservoir formation can be either miscible or immiscible. Slim-tube test has been used and accepted by the petroleum industry to study the pressure effect on CO₂ flooding process and to determine the MMP of the crude oil–CO₂ system. Most oil recovery factors of the slim-tube tests show that there is a sharp oil recovery increase below the MMP and that a sudden slope change occurs at the MMP [Wu and Batycky, 1990; Grigg *et al.*, 1997]. In the slim-tube test, however, the porous medium is homogeneous sand or bead pack with a high permeability and water is not present during the test process. As a result, the pressure effect on the CO₂ flooding process in a real reservoir case cannot be fully modelled by using the slim-tube test, especially in a tight oil reservoir.



(a)



(b)

Figure 2.1 (a) A simple model system for diffusion of CO₂ through a water-barrier phase; and (b) CO₂ concentration profiles in the simple model system [Grogan and Pinczewski, 1987].

Shyen-Yung [1991] conducted CO₂ secondary and tertiary flooding tests in carbonate core plugs with the permeability of $k = 160$ mD to study the pressure effect on the oil RF. The test results showed that the oil RF of the CO₂ tertiary flooding decreased linearly as pressure decreased and that there was no sudden oil RF reduction below the MMP. Unlike CO₂ tertiary flooding, the CO₂ secondary flooding in Shyen-Yung's study had similar pressure-effect trend to that of slim-tube test. This study concluded that CO₂ mobility decreases at a decreased pressure, which offers mobility control benefits for near-miscible CO₂ flooding. Later, Schechter *et al.* [1998] conducted gravity-stable CO₂ coreflooding tests by injecting CO₂ from the top of a vertical coreholder. The permeability of the core plugs was in the range of $k = 12.7$ – 15.4 mD. The MMP of the light crude oil–CO₂ system was measured to be 1600 psi at the test temperature of $T = 151$ °F. They found that the oil RF was not reduced considerably by reducing the pressure from 1650 psi (above the MMP) to 1543 psi (near the MMP) under their test conditions. Cao and Gu [2013a] investigated the pressure and temperature effects on the oil recovery of CO₂ flooding. A series of CO₂ secondary coreflooding tests were conducted in tight core plugs with permeabilities in the range of $k = 0.8$ – 2.5 mD. Their results suggested that a rapid decrease of the oil RF took place as the test pressure was below the MMP in either low-temperature liquid CO₂ flooding or high-temperature supercritical CO₂ flooding.

2.5 SWAG Injection

2.5.1 Laboratory studies

The first SWAG injection study was conducted by Caudle and Dyes [1958]. They found that the mobility of miscible gas displacement can be decreased by co-injecting water along with the miscible gas. A five-spot flooding model with 0.25 inch in thick and 10 inch in width was used in their study. The test results showed that the ultimate sweep efficiency was increased from about 60% by a continuous gas drive to about 90% by a SWAG injection. They also concluded that the desired water–gas injection ratio is reached when the water phase and gas phase flow at the same speed. Since then, more efforts were further made to explore the oil recovery mechanisms and find the optimum operating parameters of SWAG injection.

Visualization test

Sohrabi *et al.* [2008] studied the residual oil displacement mechanisms of near-miscible methane and simultaneous water-and-methane injection by conducting high-pressure micro-model visualization tests. The total injection rate was kept the same in each test and two different gas volume fractions of 0.2 and 0.5 were tested for the SWAG injection process. Figure 2.2 shows the snapshots of fluid distribution in the micro-model during methane injection, SWAG injection with a gas volume fraction of 0.2, and SWAG injection with a gas volume fraction of 0.5. This study showed that in the gas-only injection process, only the gas–oil interface advanced. In the SWAG injection process, nevertheless, both the water–oil and gas–oil interfaces advanced and squeezed the oil out together. This experimental study also concluded that the near-miscible SWAG recovered

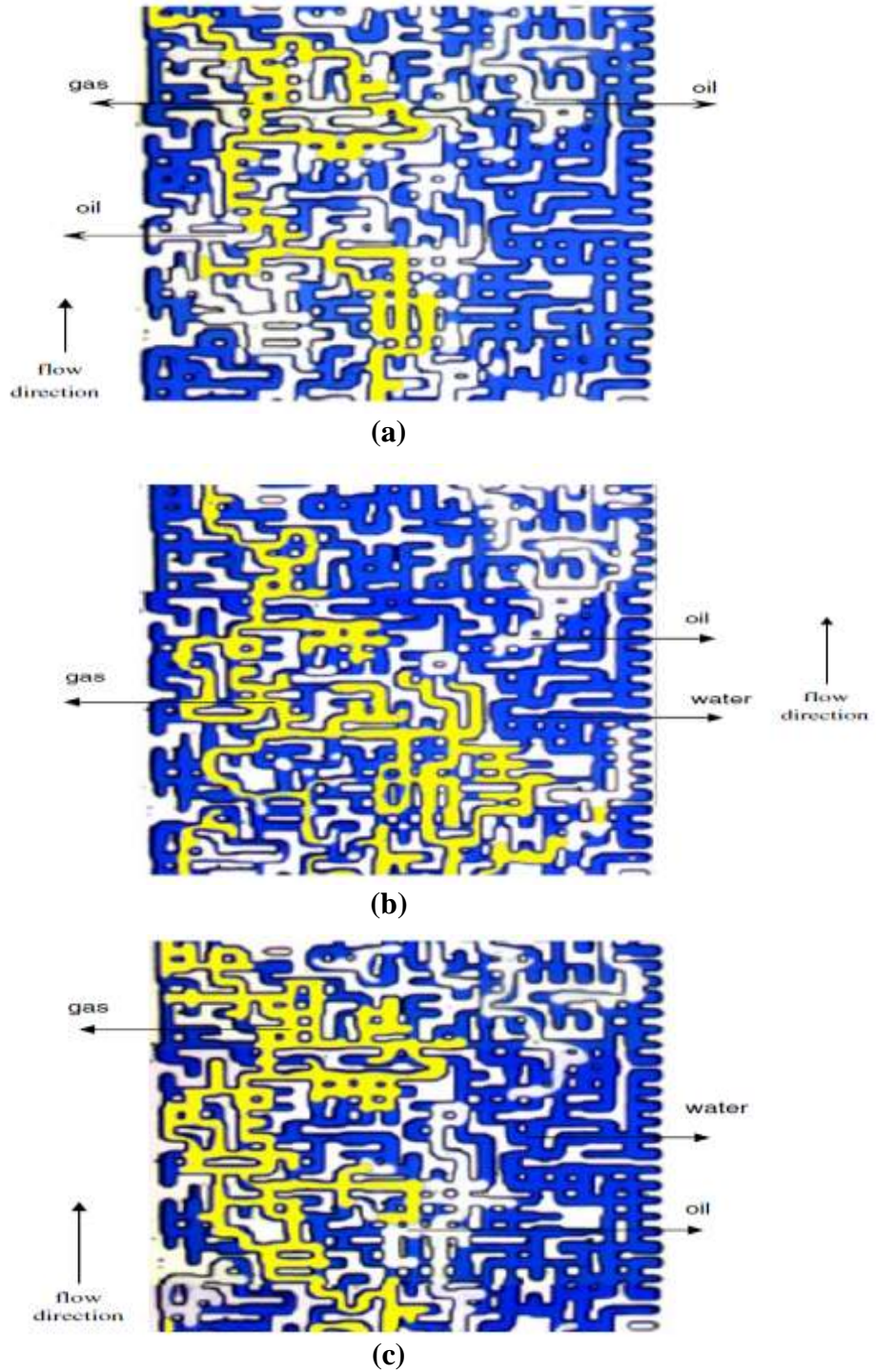


Figure 2.2 Snapshots of fluid distribution within a micro-model of (a) Continuous gas injection; (b) SWAG injection with a gas volume fraction of 0.2; and (c) SWAG injection with a gas volume fraction of 0.5 [Sohrabi *et al.*, 2008].

as much residual oil as the near-miscible gas injection, whereas the SWAG injection consumed much less gas. With the two different gas volume fractions of 0.2 and 0.5, the final oil recovery for the SWAG injection is found to be independent of the gas fraction, which is also concluded in another experimental study [Heidari *et al.*, 2013a].

Gas fraction

In the paper published by Sohrabi and Fatemi [2012], two near-miscible simultaneous water-and-methane tests with gas volume fractions of $f_g = 0.2$ and 0.5 were conducted in mixed-wet core plugs with the permeability of $k = 65$ mD. These two tests achieved almost the same final oil recovery factor but the oil recovery rate was decreased by increasing the gas fraction. Tiffin and Yellig [1983] presented the results of coreflood tests to address the CO_2 fraction effect on miscible CO_2 -SWAG tertiary flooding after waterflooding in Berea core plugs with different wettabilities. In water-wet cores with the permeability of $k = 386$ mD, the oil RFs increased with the increased gas fraction and decreased injection rate. In the oil-wet cores with the permeability of $k = 187$ mD, the gas fraction had no significant effect on the oil RF. It was concluded that in the water-wet cores, water prevented the residual oil phase from being contacted by CO_2 . More CO_2 and a longer diffusion time are needed to recover the oil droplets. On the other hand, the residual oil in the oil-wet cores was far more continuous and much easier to be displaced out by miscible CO_2 . More recently, Shetty *et al.* [2014] conducted CO_2 -SWAG tertiary coreflood tests with four different CO_2 volume fractions of $f_g = 0.2, 0.4, 0.6,$ and 0.8 in Berea sandstone core plugs with the permeability of $k = 29.15\text{--}46.43$ mD. All the SWAG injection tests were conducted until 2.0 PV of CO_2 was injected and the same total volume injection rate was used in each test. They found an optimal gas volume fraction

of $f_g = 0.4$, at which the best oil recovery factor was obtained. An increase or decrease in the gas fraction flow resulted in a decreased oil RF.

Injection scheme

Some experimental studies have been done to compare CO₂-SWAG injection with other injection schemes [Aleidan and Mamora, 2010; Heidari *et al.*, 2013a; Sohrabi and Fatemi, 2012]. In Aleidan and Mamora's study, waterflooding, CGI, CO₂-WAG injection, and CO₂-SWAG injection were carried out in carbonate core plugs with an average permeability of $k = 90$ mD. Different brine salinities were tested in their tests. According to the test results, CO₂-SWAG injection always achieved the highest oil RF among the four injection schemes at each salinity level. The oil RF of the SWAG injection was increased as the brine salinity was decreased. Aleidan and Mamora also found that the pressure drop across the core was much more stable in the CO₂-SWAG injection than that in the CO₂-WAG injection. CO₂-SWAG injection also achieved the best oil RF in the study of Heidari *et al.* [2013a]. They compared CGI, CO₂-WAG injection, and CO₂-SWAG injection in an oil-wet core plug with a permeability of $k = 8$ mD. With the most delayed gas BT, CO₂-SWAG injection showed the best mobility control of CO₂. Tapering strategy for SWAG injection was also tested and it showed promising results with further postponed gas BT and less CO₂ consumption. Sohrabi and Fatemi's study, however, indicated that the CO₂-SWAG injection recovered less oil than CO₂-WAG injection and even less than the waterflooding process. A high pressure drop across the core plugs was also recorded, which illustrated a low injectivity problem for the SWAG injection. As a result, Sohrabi and Fatemi concluded that CO₂-SWAG injection had the worst performance in the mix-wet rocks, in comparison with waterflooding, CGI, and CO₂-

WAG injection. SWAG-tail gas injection and SWAG-tail WAG injection process were also investigated in their study.;

2.5.2 Numerical simulations

Attanucci *et al.* [1993] performed numerical simulations to study the water and gas slug size effect on WAG process and their research results indicated that reducing the slug size had a favourable economic potential with an increased oil RF. Stone [2004] developed an approximate quasi-steady state reservoir simulator to study the vertical sweep efficiency of water and gas co-injection. A new SWAG injection scheme of injecting gas near the bottom of the formation and injecting water above the gas with a high injection rate was proposed. The simulation results showed that the vertical sweep efficiency of this modified SWAG injection was three times higher than that of WAG injection. Similar numerical simulations about the optimization of SWAG injection have been performed to study the water injector location, gas fraction, and reservoir heterogeneity [Jamshidnezhad, 2008] as well as sensitivity analysis, such as mobility ratio and injection rate [Algharaib *et al.*, 2007]. Injected gas type for the SWAG injection was also investigated by using numerical simulations [Heidari *et al.*, 2013b]. In their study, the SWAG injection schemes by using CO₂, N₂, or CH₄ gas were compared. The simulation results showed that CO₂-SWAG injection achieved the highest oil RF, whereas N₂- or CH₄-SWAG injection recovered almost no oil after the gas BT.

2.5.3 Pilot tests

In comparison with continuous gas flooding or WAG injection, relatively few SWAG injection oilfield applications have been reported [Christensen *et al.*, 2001]. In 1963, the

first SWAG injection project was tried in Seeligson field, aiming to improve sweep efficiency [Walker and Turner, 1968]. Propane- and ethane-enriched gas was applied until 1965 when the injection gas was converted to dry gas. The SWAG injection in Seeligson was unsuccessful with injection difficulties and no significant additional oil recovery. In 1966, this project was terminated as the injection pressure exceeded the equipment capability. Although the recovery process in Seeligson field was considerably below the anticipation, the SWAG injection applications in Joffre Viking [Stephenson *et al.*, 1993], Rangely Weber [Robie *et al.*, 1995], Kuparuk River [Ma *et al.*, 1995], and Siri field [Quale *et al.*, 2000] had optimistic outcomes.

In the Joffre Viking pool, three injection strategies were conducted and compared, namely CO₂-CGI, CO₂-WAG injection, and CO₂-SWAG injection. The test data showed that the CGI contacted less than 50% of the sandstone formation because of gravity overriding and an adverse mobility ratio. The CO₂-WAG injection with a water slug size of 10% hydrocarbon pore volume (HCPV) offered little improvement on continuous CO₂ injection. On the other hand, CO₂-SWAG injection with a CO₂ volume fraction approaching 0.5 gave the best sweep efficiency and oil recovery performance. In this pilot test, a CO₂ slug was injected prior to the SWAG injection to enhance injectivity near the well bore. In the Rangely Weber oilfield, CO₂-SWAG injection was proposed because a CO₂-WAG project with a reduced slug size showed an increased oil recovery factor. In comparison with CO₂-WAG injection, the CO₂-SWAG injection had a higher oil RF as well as more stabilized gas and water production. Besides, the injectivity of water-CO₂ mixture was not affected in this oilfield test. An increased investment for the installation of a monitoring system and a backflow control system, however, was required.

In both the Kuparuk River oilfield and Siri offshore oilfield, the produced gas was mixed with injection water to conduct the SWAG injection. A better controlled gas mobility and a more stable gas–oil ratio (GOR) of SWAG injection were reported in both cases. In the Kuparuk River, the mixing of the water and gas phases was done before injection by adopting static mixers and the wellhead pressure was kept stable in the injection process. It was found that the injection rate was decreased with an increased gas fraction of the injected mixture. The authors concluded that it was caused by the decrease of the bottom-hole pressure (BHP). Lastly, for the SWAG application in the Siri oilfield, the injectivity problem was also experienced as the injectivity depended on the gas fraction, whether the injection pressure was below or above the fracturing pressure. The injectivity increased for small gas fractions until reached a maximum value. With a further increase of the gas fraction, the injectivity declined rapidly. It was speculated that above the fracturing pressure, gas had a higher tendency to escape into the formation and a lower efficiency in hydraulically wedging, in comparison with water. Therefore, the increase of the gas fraction resulted in the decrease of the fracture length and the effective permeability, which led to the injectivity reduction.

2.6 Problem Statement

As described in the preceding sections of this chapter, for a CO₂-based EOR process, its EOR mechanisms and oil recovery process are different in the MPZ and ROZ, especially when rock properties of these two zones are different. Thus it is of fundamental and practical importance to understand how the production conditions and rock properties affect the actual CO₂-EOR performance in each of these two zones. Besides, for CO₂-SWAG injection, which is a promising EOR technique, no laboratory

tests have been conducted to study its performance and explore its potential for recovering the light crude oil in a tight oil formation. Moreover, it is necessary to identify an optimum WGR in order to achieve the best oil recovery under the light oil reservoir conditions. Therefore, the main objective of this thesis is to differentiate CO₂-base EOR processes in the tight MPZ and in the vuggy ROZ and further study the feasibility of conducting miscible CO₂-SWAG injection in the tight MPZ.

This thesis studies the mutual interactions between the light crude oil and CO₂, water- and CO₂-based EOR processes in the tight dolostone and in the vuggy limestone core plugs, and miscible CO₂-SWAG injection with different injected WGRs in the tight reservoir core plugs. First, the equilibrium IFTs between the crude oil and CO₂ were measured under different equilibrium pressures and the actual reservoir temperature by applying the axisymmetric drop shape analysis (ADSA) technique for the pendant drop case. Second, the oil-swelling effect and light-HCs extraction by supercritical CO₂ were observed by using a see-through windowed IFT cell and a microscope camera. Third, a series of ten water- and CO₂-based coreflood tests were carried out at different production pressures with different CO₂ injection timings and two kinds of carbonate reservoir core plugs collected from the upper tight MPZ and the lower vuggy ROZ of the Steelman oilfield. Fourth, the effective viscosities of water-CO₂ mixtures with twelve different water volume fractions from 0 to 1 at the actual reservoir pressure and temperature were measured by using a high-pressure capillary viscometer. Finally, another six coreflood tests were undertaken to compare and examine the overall oil recovery process of miscible CO₂-SWAG injection in the tight MPZ. They are miscible CO₂ secondary flooding, waterflooding followed by miscible CO₂ tertiary flooding,

miscible CO₂-WAG injection and three miscible CO₂-SWAG injection tests with different injected WGRs of 1:3, 1:1, and 3:1.

CHAPTER 3 EXPERIMENTAL

3.1 Materials

In this study, first, a number of carbonate reservoir core plugs were collected from several wells located in the Steelman oilfield, Saskatchewan, Canada. These core plugs were purposely taken from two different layers at the reservoir depths of 1,426.2–1,492.9 m, the upper Midale layer above and the lower Frobisher layer below the OWC. The Midale layer, which contains about 83% of the oil reserves of the pool, is the MPZ of the Steelman oilfield [Dong *et al.*, 2001]. The core plugs were cut with a diameter of one inch and their two ends were trimmed. The thin-section analysis was conducted to estimate the porosities and permeabilities, and qualitatively indicate the petrographic properties of five rock samples. The X-ray diffraction (XRD) was undertaken to quantitatively determine the compositions of these rock samples. Then, for the CO₂-SWAG injection study, a number of tight reservoir core plugs were taken from wells located in the Tatagwa oilfield, Weyburn–Estevan area, Saskatchewan, Canada. These core plugs of the Bakken formation were also cut with a diameter of one inch and had two ends trimmed.

The original light crude oil was also collected from the Steelman oilfield. The obtained light crude oil was cleaned by using a centrifuge (Allegra X-30 Series, Beckman Coulter, USA) to remove any sands and brine. Also, an inline filter (SS-2TF-0.5, Swagelok, Canada) with a pore size of 0.5 μm was used to further remove any fine solids from the light oil. The density and viscosity of the cleaned light oil were measured to be $\rho_o = 0.819 \text{ g/cm}^3$ by using a densitometer (DMA 512P, Anton Paar, USA) and $\mu_o = 0.76$

cP by using a viscometer (DV-II+, Brookfield, USA) at the atmospheric pressure and $T_{\text{res}} = 51.1$ °C. The molecular weight of the light oil was measured to be 188.8 g/mol by using an automatic high-sensitivity wide-range cryoscopy (Model 5009, Precision Systems Inc., USA), which was conducted by the Core Laboratories, Calgary, Canada. The asphaltene content of the cleaned light oil was measured to be $w_{\text{asp}} = 0.15$ wt.% (*n*-pentane insoluble) by using the standard ASTM D2007-03 method and filter papers (No. 5, Whatman, England) with a pore size of 2.5 μm . The compositional analysis result of the cleaned light oil was obtained by using the standard ASTM D86 method and conducted by the Saskatchewan Research Council (SRC), Regina, Canada. Its detailed results are given in Table 3.1. The total molar percentage of C_{1-10} is 49.55%. The high percentage of the light to intermediate HCs indicates that this light crude oil is especially suitable for CO_2 -EOR.

The reservoir brine sample was collected from the Steelman oilfield, cleaned, and analyzed. The detailed physicochemical properties were analyzed by the SRC. Its detailed physicochemical properties are listed in Table 3.2. The concentration of its total dissolved solids (TDS) was measured to be 180,000 mg/L at 110 °C. The dominant cation is sodium and the dominant anion is chloride. In this study, however, a synthetic brine was prepared by dissolving sodium chloride (NaCl) into a deionized water to reach the same TDS or salinity and used in all coreflood tests to substitute the reservoir brine. This is because fine solids in the reservoir brine might further reduce the ultra-low permeability of the tight core plugs during the reservoir brine injection process. The purity of carbon dioxide (Praxair, Canada) used in this study was equal to 99.998 mol.%.

Table 3.1 Compositional analysis result of the cleaned Steelman original light crude oil ($\rho_o = 0.819 \text{ g/cm}^3$, $\mu_o = 0.76 \text{ cP}$ at the atmospheric pressure and $T_{\text{res}} = 51.1 \text{ }^\circ\text{C}$, $MW_{\text{oil}} = 188.8 \text{ g/mol}$, Well No.: 3-29-3-4W2) with the asphaltene content of $w_{\text{asp}} = 0.15 \text{ wt.}\%$ (*n*-pentane insoluble).

Carbon No.	mol.%	Carbon No.	mol.%
C ₁	0.00	C ₂₇	0.84
C ₂	0.72	C ₂₈	0.80
C ₃	0.40	C ₂₉	0.65
C ₄	1.59	C ₃₀	0.57
C ₅	3.94	C ₃₁	0.57
C ₆	8.26	C ₃₂	0.53
C ₇	12.27	C ₃₃	0.37
C ₈	8.19	C ₃₄	0.34
C ₉	7.66	C ₃₅	0.41
C ₁₀	6.52	C ₃₆	0.31
C ₁₁	6.04	C ₃₇	0.30
C ₁₂	4.58	C ₃₈	0.21
C ₁₃	4.41	C ₃₉	0.27
C ₁₄	3.92	C ₄₀	0.27
C ₁₅	3.65	C ₄₁	0.13
C ₁₆	2.95	C ₄₂	0.12
C ₁₇	2.55	C ₄₃	0.17
C ₁₈	2.43	C ₄₄	0.17
C ₁₉	2.12	C ₄₅	0.10
C ₂₀	1.66	C ₄₆	0.10
C ₂₁	1.84	C ₄₇	0.09
C ₂₂	1.02	C ₄₈	0.08
C ₂₃	1.31	C ₄₉	0.08
C ₂₄	1.12	C ₅₀₊	1.34
C ₂₅	1.07	Total	100.00
C ₂₆	0.96		

Table 3.2 Physical and chemical properties of the cleaned Steelman reservoir brine at $P = 1$ atm (Well No.: 3-29-3-4W2).

Temperature (°C)	15	20	40
Density (g/cm ³)	1.091	1.089	1.081
Viscosity (cP)	1.52	1.34	0.81
pH at 20.0 °C	7.81		
Specific conductivity (µS/cm) at 25.0 °C	245,000		
Refractive index at 20.0 °C	1.3611		
Chloride (mg/L)	122,000		
Sulphate (mg/L)	4,800		
Potassium (mg/L)	2,190		
Sodium (mg/L)	59,700		
Calcium (mg/L)	2,190		
Magnesium (mg/L)	510		
Iron (mg/L)	2.1		
Manganese (mg/L)	<0.05		
Barium (mg/L)	0.14		
Total dissolved solids (mg/L) at 110 °C	180,000		

The densities, viscosities, and compressibilities of pure CO₂ at different pressures and temperatures were calculated by using the CMG WinProp module (Version 2013.20, Computer Modelling Group Limited, Canada) with Peng–Robinson equation of state (P–R EOS) [Peng and Robinson, 1976].

3.2 Thin-Section Analysis of Rock Samples

Five Steelman rock thin-sections were prepared by impregnating selected rock slugs with epoxy that contained blue Orasol dye. This was done to identify porosity and to reduce the likelihood of delicate structures from being destroyed during preparation. The rock samples were stained with alizarin red S, potassium ferricyanide, and sodium cobaltinitrite to distinguish calcite, ferron carbonates, and alkali feldspars, respectively. Photomicrographs were taken for the rock thin-sections. Porosity and permeability of the rock sample were estimated petrographically.

3.3 XRD Evaluation of Rock Samples

To identify crystalline materials of each rock sample, approximately 5–10 g of the bulk rock sample was ground into homogeneous powders. A goniometer (Rigaku Miniflex II, Rigaku Corporation, Japan) was used to scan the rock powders and produce spectra. Then, percentages of mineral types were determined by interpretation of the spectra. The thin-section analysis and XRD evaluation of the Steelman rock samples were undertaken by Calgary Rock and Materials Services Inc..

3.4 Oil Density Measurement

The density of the original Steelman crude oil was measured by using a digital high-pressure densitometer (DMA 512P, Anton Paar, USA) at the atmosphere pressure and reservoir temperature of $T_{\text{res}} = 51.1$ °C. Only a small amount of fluid sample (approximately 1 cm^3) is required for the density measurement. A water bath (Polystat 3W11, Core-Parmer, Canada) with an accuracy of 0.1 °C was connected to the densitometer sampler to maintain the constant temperature of $T_{\text{res}} = 51.1$ °C.

Prior to each density measurement, the densitometer sampler was cleaned with kerosene and ethanol in sequence and dried by using high-pressure air. Then the liquid, whose density needs to be measured, was injected into the densitometer sampler by using a syringe pump (100 DX, ISCO Inc., USA). After the liquid came out from the outlet of the densitometer sampler, the injection was kept for 5 minutes to ensure that any air inside the sampler was displaced out. Two standard liquids, N4 and S20 (Hoskin Scientific Ltd, Canada), were used to calibrate the densitometer before the crude oil density measurement. The respective densities of N4 and S20 are 0.7665 and 0.8439 g/cm^3 at the temperature of $T = 50$ °C. The density of the crude oil was measured three times at the atmosphere pressure and reservoir temperature of $T_{\text{res}} = 51.1$ °C. The average value of the three measured oil densities is presented in this study.

3.5 Oil Viscosity Measurement

The viscosity of the original crude oil was measured by using a cone-plate viscometer (DV-II +, Brookfield Engineering Laboratories, USA) at the atmosphere pressure and reservoir temperature of $T_{\text{res}} = 51.1$ °C, the latter of which was maintained by using the water bath. A cone spindle of model CPE-40 was chosen for the measurement. Prior to

the viscosity measurement of the original crude oil, a sample cup of the viscometer and the cone spindle were cleaned with kerosene and ethanol and dried by using high-pressure air. The original crude oil sample of 0.5 cm^3 was then placed and sheared between the flat sample cup and cone spindle for its viscosity measurement.

3.6 Interfacial Tension Measurements

Figure 3.1 shows a schematic diagram of the experimental set-up used for measuring the equilibrium IFT between a crude oil and CO_2 by applying the ADSA technique for the pendant drop case [Cheng et al., 1990]. The major component of the ADSA system was a see-through windowed high-pressure IFT cell (IFT-10, Temco, USA), which had a cell volume of 49.5 cm^3 . A stainless steel syringe needle was installed at the top of the IFT cell and used to form a pendant oil drop. The maximum operating pressure and temperature of this IFT cell are equal to 10,000 pisa and $177 \text{ }^\circ\text{C}$, respectively. The temperature during the IFT measurements was maintained by wrapping the IFT cell with a heating tape (TBSO-101-060, BriskHeat, USA) and controlled by using a stepless temperature controller (3PN1010B, Staco, USA). A light source and a glass diffuser (240-341, Dyna-Lume, USA) were used to provide uniform and sufficient illumination for the pendant oil drop. A monochrome microscope camera (MZ6, Leica, Germany) was used to observe and capture the sequential digital images of the dynamic pendant oil drop inside the IFT cell at different times. The IFT cell was positioned horizontally between the light source and the microscope camera. The entire ADSA system and the IFT cell were placed on a vibration-free table (RS4000, Newport, USA). The digital image of the dynamic pendant oil drop surrounded by CO_2 at any time was acquired in a tagged image file format (TIFF) by using a digital frame grabber (Ultra II, Coreco Imaging, Canada)

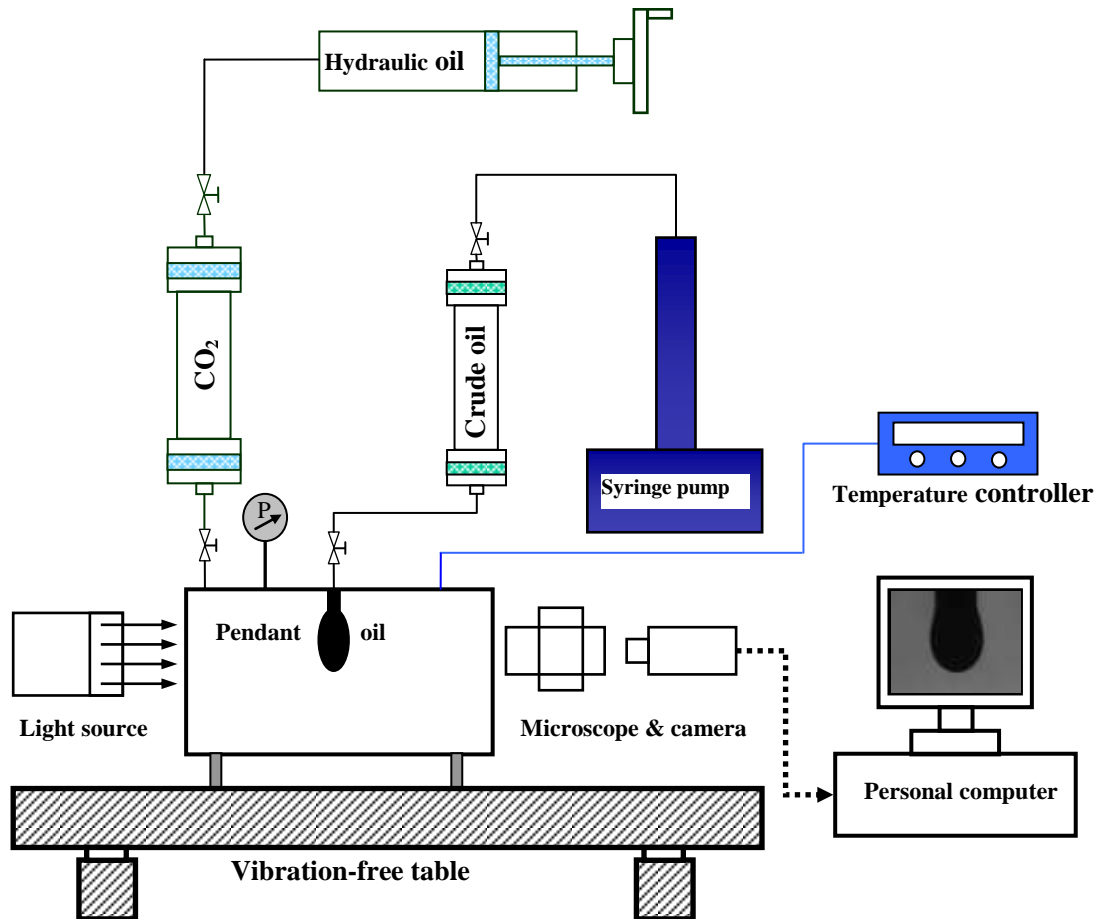


Figure 3.1 Schematic diagram of the experimental set-up used for measuring the equilibrium interfacial tension (IFT) between the light crude oil and CO₂ by applying the axisymmetric drop shape analysis (ADSA) technique for the pendant drop case.

and automatically stored in a Dell desktop computer, which was used to perform the subsequent pendant drop image analysis, digitization, and computation. The crude oil and pure CO₂ were stored in two transfer cylinders (500-10-P-316-2, DBR, Canada).

Prior to each test, the IFT cell was tested for leakage and flushed with CO₂ 3–5 times to remove any air from the entire system. Then CO₂ was injected slowly into the IFT cell from its bottom port by using a manual displacement pump (PMP-500-1-10-HB-316-MO-CO, DBR, Canada) at a pre-specified pressure and a constant temperature of $T_{\text{res}} = 51.1$ °C. After the pressure and temperature inside the pressure cell reached their stable values, the crude oil was introduced from the original crude oil sample cylinder to the high-pressure IFT cell by using a programmable syringe pump (100 DX, ISCO Inc., USA) to form a pendant oil drop at the tip of the syringe needle. Once a well-shaped pendant oil drop was formed, the sequential digital images of the dynamic pendant oil drop at different times were acquired and stored automatically in the personal computer. Then the ADSA program for the pendant drop case was executed to determine the dynamic IFT of the dynamic pendant oil drop. The IFT experimental error is equal to 0.05 mJ/m². The IFT measurement was repeated for at least three different pendant oil drops to obtain a satisfactory repeatability at each pre-specified pressure and constant temperature. In this study, the crude oil–CO₂ dynamic and equilibrium IFTs for three different pendant oil drops were measured at seventeen different equilibrium pressures $P_{\text{eq}} = 1.08$ –18.66 MPa and a constant temperature of $T_{\text{res}} = 51.1$ °C. Only the average value of the equilibrium IFTs of three repeated IFT measurements at each equilibrium pressure is presented in this study. Then the VIT technique was applied to determine the MMP from the measured average equilibrium IFT versus equilibrium pressure data at $T_{\text{res}} = 51.1$ °C.

3.7 Oil-Swelling Effect and Ligh-HCs Extraction by CO₂

The interfacial interactions between the light crude oil and CO₂ phase at high pressures and the reservoir temperature of $T_{\text{res}} = 51.1$ °C were visualized and recorded by using the see-through windowed IFT cell and the microscope camera. Once the pendant drop of the original light crude oil was introduced into the pressurized CO₂ inside the IFT cell, its volume and shape continued to change. It was found that at low equilibrium pressures, there was an initial oil-swelling process, which was followed by the subsequent slow light-HCs extraction process. The former process was revealed by volume increase of the dynamic pendant oil drop as CO₂ was gradually dissolved into the oil phase. The latter process was characterized by its volume reduction as the light components of the pendant oil drop were slowly extracted into CO₂ phase. At high equilibrium pressures, the initial quick light-HCs extraction was observed as the interactions between the oil and the CO₂ phases became strong. At the beginning, the light components of the crude oil were rapidly extracted from the pendant oil drop to CO₂ phase. During this process, the light crude oil was continuously introduced from the original light crude oil sample cylinder and added into the existing pendant oil drop by using the programmable syringe pump. Afterwards, the subsequent slow light-HCs extraction occurred. In this study, the initial quick and strong light-HCs extraction process at the MMP and $T_{\text{res}} = 51.1$ °C was observed and recorded.

3.8 Effective Viscosity Measurements

In this study, the co-injected water–CO₂ mixture with different water volume fraction was assumed to be a pseudo single-phase fluid. To measure the effective viscosity of the water–CO₂ mixture at the tight oil reservoir conditions, a capillary viscometer was

constructed and its schematic diagram is shown in Figure 3.2. A 23-ft long stainless steel tubing (15-9A1-006, High Pressure Equipment Co., USA) was coiled to form a capillary tubing. The outer diameter (OD) and inner diameter (ID) of the capillary tubing were equal to 1/16 in. and 0.006 in., respectively. This long and small capillary tubing was chosen to ensure that a pressure drop along it was large enough to accurately measure the low effective viscosity of the water–CO₂ mixture, including water or CO₂ alone. Two programmable syringe pumps (100DX, ISCO Inc., USA) were used to displace the synthetic brine and CO₂, respectively. The separately and concurrently injected synthetic brine and CO₂ were commingled together at a T-union (SS-200-3, Swagelok, Canada) before the water–CO₂ mixture was injected through the capillary viscometer. Two high-pressure cylinders (500-10-P-316-2, DBR, Canada) were used to store and deliver the synthetic brine and CO₂, respectively. To prevent any backflow of either synthetic brine or CO₂ during the co-injection process, two high-pressure check valves (SS-CHS2-1/3, Swagelok, Canada) were installed in the synthetic brine and CO₂ injection lines respectively in front of the T-union, where the two injection lines were converged. When the water–CO₂ mixture passed through the capillary tubing, the pressures at the inlet and outlet of the capillary viscometer were measured by using a digital pressure indicator (PM, Heise, USA) and recorded in a personal computer at a preset time interval of 15 s. Another syringe pump was used to apply a high pressure at the outlet of a back-pressure regulator (BPR) (BPR-50, Temco, USA). The constant temperature of $T_{res} = 51.1$ °C during each effective viscosity measurement was maintained by placing the capillary viscometer inside an oven (OF-21E, JEIO Tech, Korea). In addition, the synthetic brine and CO₂ cylinders were wrapped with two heating tapes (TBSO-101-060, BriskHeat,

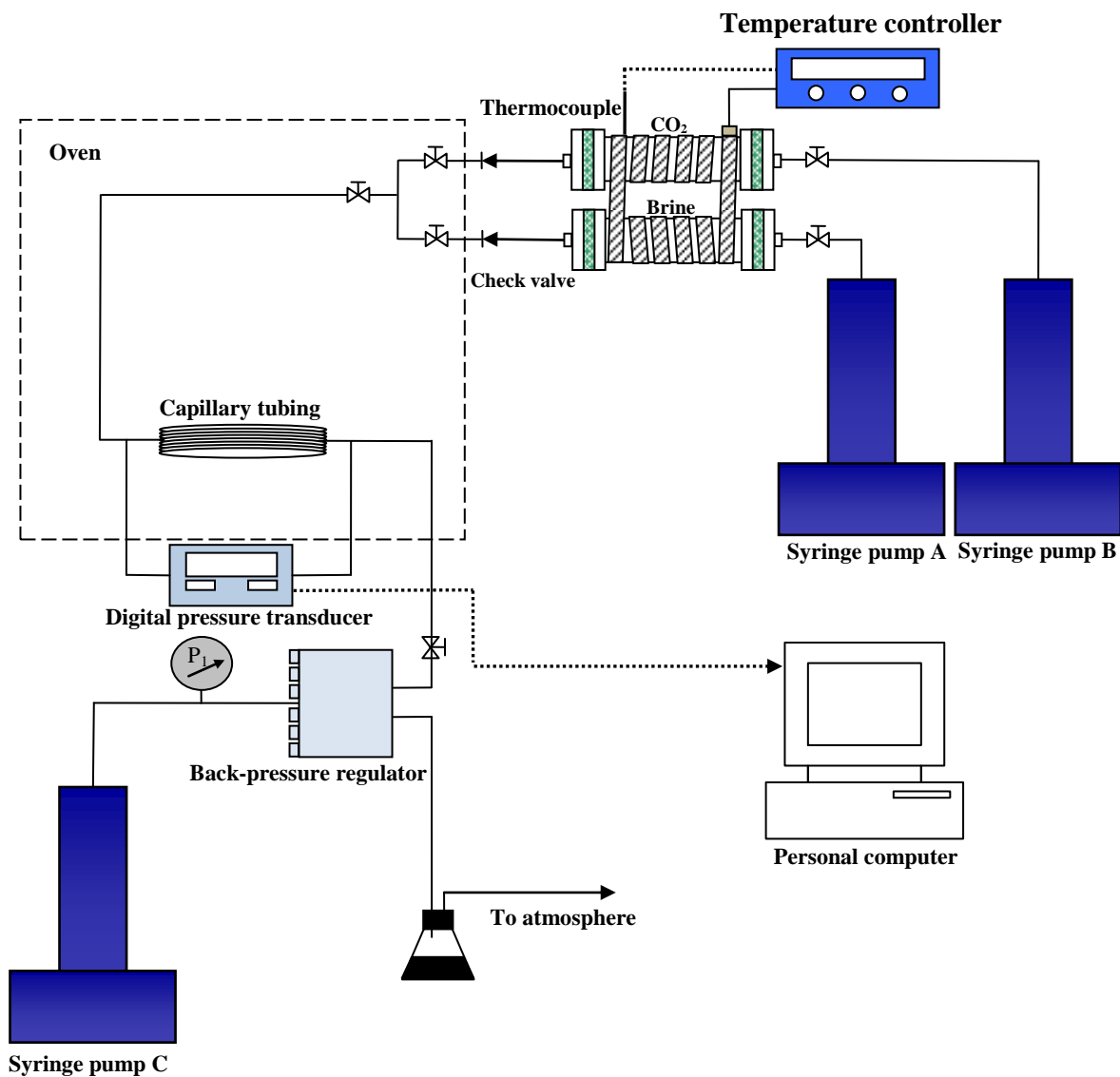


Figure 3.2 Schematic diagram of the high-pressure capillary viscometer used for measuring the effective viscosity (μ_{mix}) of each water–CO₂ mixture.

USA), whose temperatures were controlled by using a temperature controller (Standard-89000-00, Digi-Sense, USA) and kept at $T_{\text{res}} = 51.1$ °C.

Prior to each effective viscosity measurement, the temperatures of the injected fluid(s) and capillary tubing were increased to and maintained at the reservoir temperature of $T_{\text{res}} = 51.1$ °C for at least 12 h. Then the entire injection system was pressurized by gradually increasing the working pressure of the BPR until the outlet pressure of the capillary viscometer reached 15.0 MPa, which was equal to the production pressure used in each coreflood test as described later. Afterward, the synthetic brine and CO₂ were co-injected at different rates so that a series of twelve different water volume fractions can be obtained. The effective viscosities reported in this study were measured by gradually increasing the water volume fraction in the water–CO₂ mixture from 0 (i.e., pure CO₂) to 1 (i.e., pure synthetic brine). For each water–CO₂ mixture, three total constant volume flow rates ($q_{\text{mix}} = q_{\text{brine}} + q_{\text{CO}_2} = 0.1, 0.2, 0.3$ cm³/min) were used. In this study, a distilled water with $\mu_w = 0.537$ cP at the atmospheric pressure and $T_{\text{res}} = 51.1$ °C was used as a standard viscosity liquid and injected through the capillary tubing at different constant volume flow rates ($q_w = 0.1$ – 1.0 cm³/min) to calibrate the capillary viscometer. The Hagen–Poiseuille equation was applied to determine the so-called “effective radius” of the capillary tubing. With the determined “effective radius” of $r_{\text{eff}} = 0.018$ cm, this equation was finally applied to determine the effective viscosity of each water–CO₂ mixture:

$$\mu_{\text{mix}} = \frac{\pi(r_{\text{eff}})^4 \Delta P}{8 q_{\text{mix}} L}, \quad (3.1)$$

where μ_{mix} is the effective viscosity of the water–CO₂ mixture at $P = 15.0$ MPa and $T_{\text{res}} = 51.1$ °C; ΔP and q_{mix} are the measured steady pressure drop and pre-specified total constant volume flow rate of the water–CO₂ mixture through the capillary tubing; r_{eff} and L are the “effective radius” and the actual length of the capillary tubing. In addition, the respective viscosities of the pure CO₂ and synthetic brine (TDS = 180,000 mg/L) at $P = 15.0$ MPa and $T_{\text{res}} = 51.1$ °C were calculated by using the CMG WinProp module.

3.9 Coreflood Tests

A schematic diagram of the coreflood apparatus used in the coreflood tests is shown in Figure 3.3. Prior to each test, reservoir core plugs from the Steelman or Tatagwa oilfield were cleaned by applying Dean–Stark extractor (09-556D, Fisher Scientific, Canada). An automatic displacement pump (PMP-1000-1-10-MB, DBR, Canada) was used to displace the crude oil, synthetic brine, or CO₂ through the composite reservoir core plugs inside a coreholder (RCHR-1.0, Temco, USA). The tap water was pumped by using a syringe pump (100DX, ISCO Inc., USA) to apply the so-called overburden pressure, which was always kept 5 MPa higher than the inlet pressure (i.e., the injection pressure, P_{inj}) of the coreholder. Four high-pressure cylinders (500-10-P-316-2, DBR, Canada) were used to store and deliver the crude oil, synthetic brine, CO₂, and tap water, respectively. These four sample cylinders and the coreholder were placed inside an air bath. A heating gun (HG 100, Thankia, USA) and a temperature controller (Standard-89000-00, Cole–Parmer, Canada) were used to heat the air bath and keep its constant temperature of $T_{\text{res}} = 51.1$ °C. A BPR (BPR-50, Temco, USA) was used to maintain the outlet pressure (i.e., the production pressure, P_{prod}) of the coreholder during water and/or

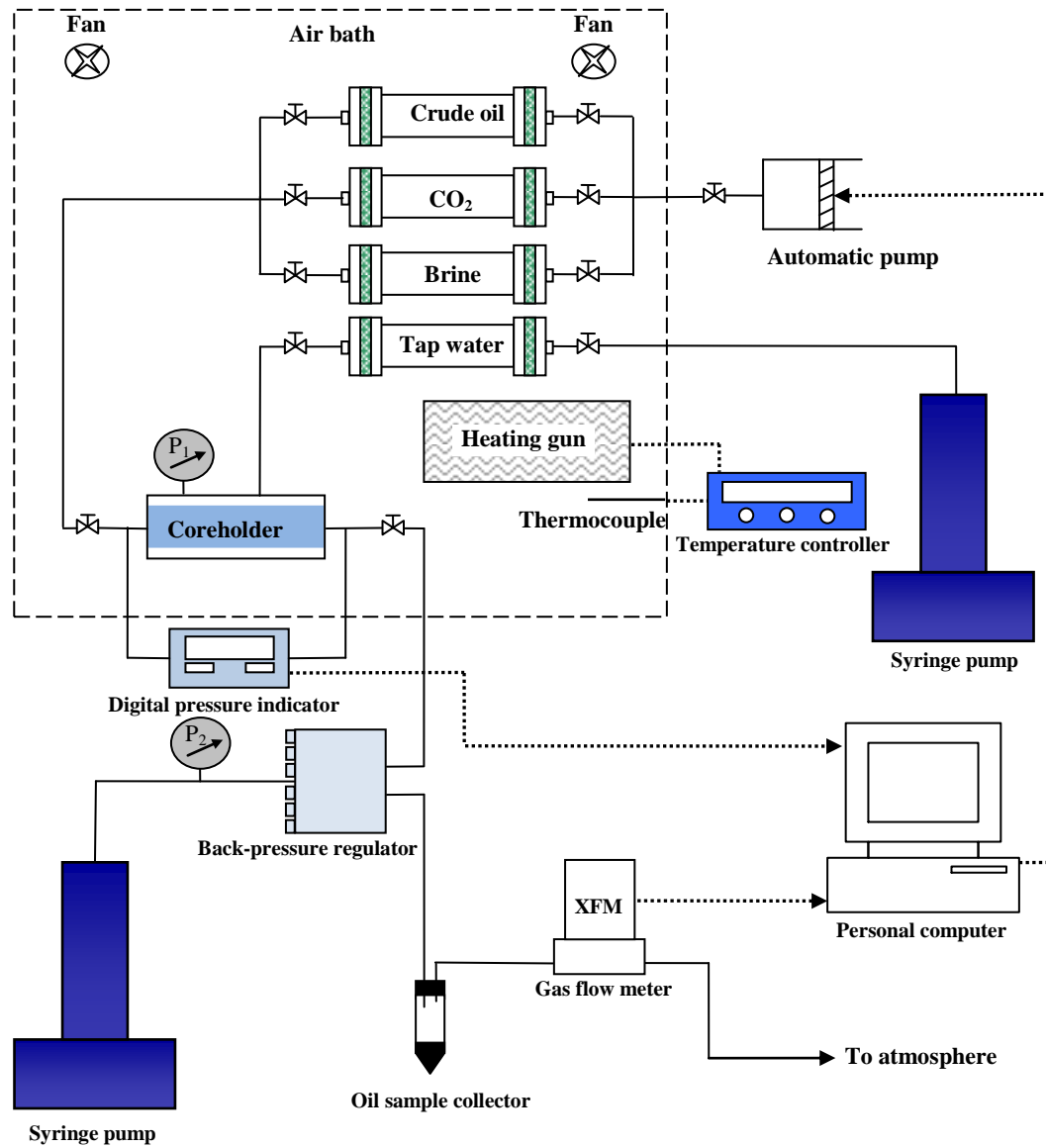


Figure 3.3 Schematic diagram of the high-pressure CO₂-based coreflood apparatus.

CO₂ flooding processes. During the synthetic brine, original light oil, and CO₂ injection processes, the injection and production pressures were measured by using the digital pressure indicator. The instantaneous gas production rate from the outlet of the coreholder was measured every second by using a gas flow meter (XFM-17, Aalborg, USA). An average produced gas flow rate was determined in every five minutes. After the produced oil passed through the BPR and flowed to a graduated sample collector, a digital video camera was used to record the respective cumulative volumes of the produced oil and water at different times. The injection and production pressures and gas production rates were measured and stored automatically in a personal computer.

The general procedure for preparing each water- and CO₂-based coreflood test in this work is briefly described below. First, the composite reservoir core plugs were placed inside the Dean–Stark extractor and thoroughly cleaned with toluene, methanol, and chloroform in sequence to remove hydrocarbons, salts, and clays, respectively. After the reservoir core plugs were cleaned and dried, they were assembled in series in a horizontal coreholder and vacuumed for 24 h. Then, the synthetic brine was used as a working fluid and injected to measure the porosity of the composite reservoir core plugs. Afterwards, the synthetic brine was injected at different flow rates ($q_{\text{brine}} = 0.01\text{--}0.1 \text{ cm}^3/\text{min}$) to measure the absolute permeability of the composite reservoir core plugs. Next, the original light crude oil was injected at $q_{\text{oil}} = 0.025 \text{ cm}^3/\text{min}$ through the synthetic brine-saturated reservoir core plugs at the ambient temperature of $T_{\text{lab}} = 22 \text{ }^\circ\text{C}$ until no more brine was produced or the connate water saturation was achieved. After the initial oil saturation and the connate water saturation were reached, the heating gun and the temperature controller were used to increase the temperature inside the airbath to $T_{\text{res}} =$

51.1 °C and maintained this temperature for at least two days. Finally, a total of 3–5 pore volumes (PVs) of the original light crude oil was further injected to pressurize the reservoir core plugs by gradually increasing the working pressure of the BPR until the pre-specified production pressure (P_{prod}) at the outlet of the coreholder was reached.

In order to investigate the feasibility of CO₂-based EOR in the tight carbonate reservoir with an underlying ROZ and differentiate its performance in the tight MPZ and in the vuggy ROZ, a total of ten coreflood tests (Tests #1–10) were conducted in the tight carbonate reservoir core plugs collected from the Steelman oilfield. The reservoir core plugs used in these ten coreflood tests were 4.4–4.9 in. long. Six coreflood tests (Tests #1–6) were first conducted through the tight dolostone core plugs collected from the upper Midale layer to examine the performance of CO₂-based EOR in the tight MPZ. First, the production pressure effect on CO₂ secondary flooding process was studied in Tests #1–4 at four different production pressures of $P_{\text{prod}} = 2.0, 6.5, 11.0, \text{ and } 14.0$ MPa. As described later, the MMP between the light crude oil and pure CO₂ at the actual reservoir temperature was determined to be 10.8 MPa. Hence, CO₂ flooding processes were considered to be miscible along the entire coreholder in Tests #3 and #4. In each test, two reservoir core plugs with similar permeabilities of $k = 0.082\text{--}0.091$ mD were used. Then another miscible CO₂ secondary flooding test (Test #5) was conducted by using two core plugs with a much lower permeability of $k = 0.019$ mD. In this test, the production pressure was set at 9.0 MPa instead of 11.0 MPa as the overburden pressure reached 30.0 MPa, which was close to the pressure rating of 34 MPa for the coreholder used in the coreflood tests. The permeability effect was studied by comparing Tests #3 and #5, though they had slightly different production pressures. Lastly, a miscible CO₂

tertiary flooding test (Test #6) was conducted and compared with the miscible CO₂ secondary flooding test (Test #3) to study CO₂ injection timing (i.e., with or without the initial waterflooding). In these six coreflood tests, CO₂ was injected at a constant volume injection rate of $q_{\text{CO}_2} = 0.1 \text{ cm}^3/\text{min}$. In Test #6, the initial waterflooding was purposely conducted at a relatively low volume injection rate of $q_{\text{brine}} = 0.025 \text{ cm}^3/\text{min}$ until no more oil was produced. In this way, a relatively high secondary oil RF of waterflooding was achieved and a relatively low residual oil saturation prior to the subsequent CO₂ flooding was reached.

Four coreflood tests (Tests #7–10) were carried out through the vuggy limestone core plugs collected from the lower Frobisher layer to study CO₂ flooding in the vuggy ROZ. In Test #7, the feasibility of miscible CO₂ secondary flooding process in the vuggy zone was examined at the production pressure of $P_{\text{prod}} = 11.0 \text{ MPa}$. The vug effect on the miscible CO₂ secondary flooding was analyzed by comparing Tests #7 and #3. In three CO₂ tertiary flooding tests (Tests #8–10), waterflooding was conducted first at a constant volume injection rate of $q_{\text{brine}} = 0.025 \text{ cm}^3/\text{min}$ to create the ROZ. The residual oil saturation after the initial waterflooding was in the range of $S_{\text{or}} = 34.33\text{--}36.86\%$. Three different production pressures of $P_{\text{prod}} = 6.5, 11.0, \text{ and } 14.0 \text{ MPa}$ were used in these three tests to study the production pressure effect on CO₂ tertiary flooding in the vuggy ROZ. Also, CO₂ injection timing effect was examined by comparing Tests #7 and #9. The constant CO₂ volume injection rate of $q_{\text{CO}_2} = 0.1 \text{ cm}^3/\text{min}$ was used in Tests #7–10. It is worthwhile to point out that all the above-mentioned coreflood tests were conducted at the same reservoir temperature of $T_{\text{res}} = 51.1 \text{ }^\circ\text{C}$. In each CO₂ secondary flooding test, CO₂ injection was terminated after a total of 2.00 PV was injected when no more oil was

produced. No water was produced in any CO₂ secondary flooding test. In each CO₂ tertiary flooding test, CO₂ injection was continued until no more oil was produced at the end.

To further study the possibility of conducting miscible CO₂-SWAG injection in the tight MPZ and examine the effect of the WGR on CO₂-SWAG injection process, additional six coreflood tests (Tests #11–16) were conducted to study and compare miscible CO₂-SWAG injection in the tight Bakken formation. The composite reservoir core plugs used in these six tests had a length of 5.9 inch. Three different miscible CO₂-EOR schemes were tested: miscible CO₂ secondary flooding (Test #11), waterflooding followed by miscible CO₂ tertiary flooding (Test #12), and miscible CO₂-WAG injection with a slug size of 0.222 PV and a water-to-CO₂ slug ratio of 1:3 (Test #13). A constant volume injection rate of $q_{\text{brine}} = q_{\text{CO}_2} = 0.1 \text{ cm}^3/\text{min}$ was used in the water or CO₂ injection process. In Test #12, a total of 2.0 PV water was injected before the miscible CO₂ tertiary flooding was initiated. Then three miscible CO₂-SWAG injection tests (Tests #14–16) with different injected WGRs of 1:3, 1:1, and 3:1 were carried out to study the WGR effect on the oil recovery process. Based on the prediction from the CMG WinProp module, a minimum injected WGR of 24:1 has to be reached in order for the CO₂ phase to be completely dissolved into the co-injected synthetic brine phase under the test conditions used in this study. Hence, supercritical CO₂ phase existed as a separate phase in the co-injected immiscible water–CO₂ mixtures in the three CO₂-SWAG injection tests. The same total volume injection rate of $q_{\text{mix}} = q_{\text{brine}} + q_{\text{CO}_2} = 0.1 \text{ cm}^3/\text{min}$ was used in Tests #14–16 and three different injected WGRs of 1:3, 1:1, and 3:1 were obtained by choosing the water and CO₂ volume injection rates properly.

Prior to the coreflooding process in each of Tests #11–16, the oil mobility in the presence of the connate water saturation was obtained from the pre-set oil injection rate ($q_o = 0.025 \text{ cm}^3/\text{min}$) and the measured stable pressure drop (ΔP_o) between the inlet and outlet of the coreholder:

$$\lambda_o = \frac{k_o'}{\mu_o} = \frac{q_o/A}{\Delta P_o/L}, \quad (3.2)$$

where λ_o is the mobility of the light crude oil; k_o' is the end-point effective permeability to the light crude oil; μ_o is the light crude oil viscosity under the test conditions; A and L are the cross-sectional area and length of the composite core plugs. All these six coreflood tests were conducted at the same reservoir temperature of $T_{\text{res}} = 51.1 \text{ }^\circ\text{C}$ and $P_{\text{prod}} = 15.0 \text{ MPa}$ to ensure that the miscibility between the light crude oil and injected CO_2 could be achieved. Moreover, based on the calculation (Figure 3.4) from the CMG WinProp module, CO_2 becomes a much condensed supercritical fluid with a highly reduced isothermal compressibility coefficient of 0.0456 MPa^{-1} at 15.0 MPa and $51.1 \text{ }^\circ\text{C}$, which is beneficial for co-injecting low-compressibility CO_2 with incompressible water phase. Each of these six CO_2 -based coreflood tests was terminated after a total of 2.0 PV of CO_2 was injected.

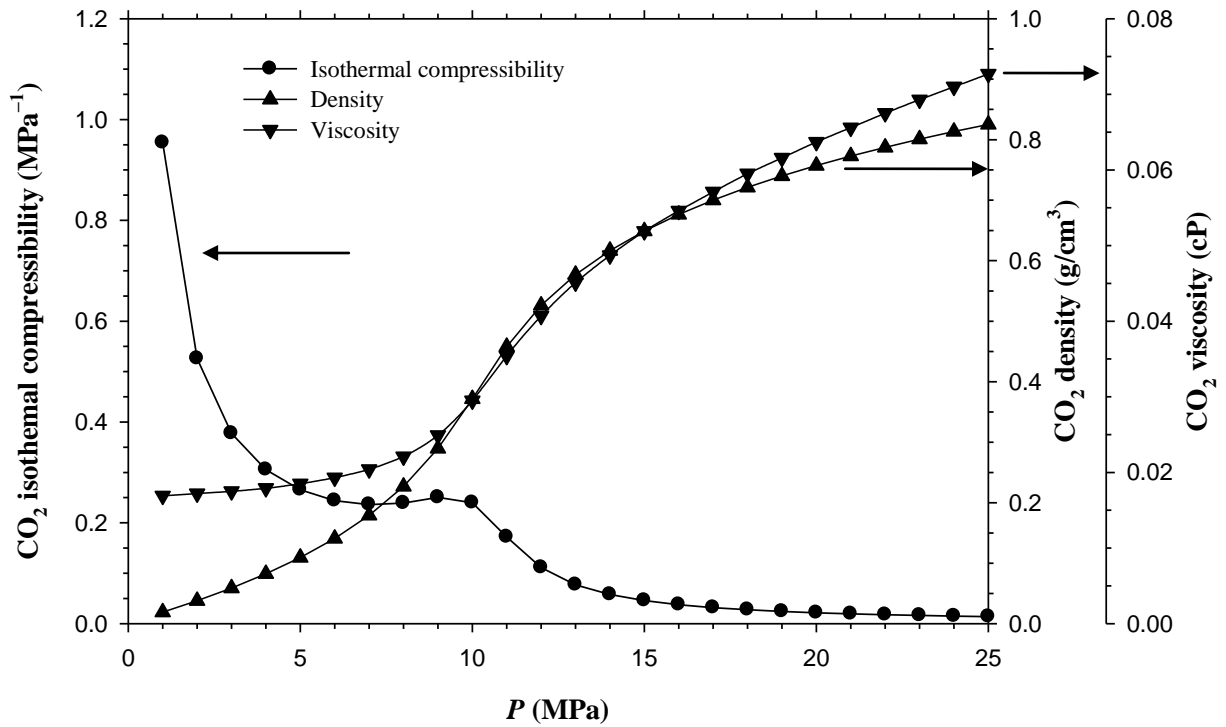


Figure 3.4 Calculated CO₂ isothermal compressibility, density and viscosity versus pressure data at the reservoir temperature of $T_{\text{res}} = 51.1$ °C by using the CMG WinProp module.

CHAPTER 4 RESULTS AND DISCUSSION

4.1 Petrographic and Mineralogical Properties

The detailed petrographic and mineralogical properties of five Steelman reservoir rock samples are listed in Tables 4.1a and 4.1b, respectively. The porosity distributions of these samples are found to be highly variable. A digital photograph (Figure 4.1a) shows a tight core plug from the Midale layer and a vuggy core plug from the Frobisher layer. A photomicrograph with some pin-point vugs within the matrix material of a tight rock sample is shown in Figure 4.1b. More specifically, the blue colour represents the porosity as a blue epoxy was used to mount the thin section. The white rhombic crystals and the smaller white grains are dolomite grains, which are the major component of the matrix. The yellowish brown material is anhydrite nodules and the black opaque grains are pyrite. Two thin-section photomicrographs (Figures 4.1c and d) illustrate a vug and a fracture in a vuggy rock sample, respectively. The dark material in these two figures is the matrix of oolitic limestone. Figure 4.1c shows that the vug has been lined with calcite spar. As shown in Figure 4.1d, the calcite spar acts as a bridging material in the fracture. Thus this fracture was a natural one, which was not induced during the coring process.

The rock samples from the Midale layer are identified as Lithofacies #1 and the rock samples from the Frobisher layer are identified as Lithofacies #2. The petrographic properties of these two Lithofacies were found to be rather different. Based on the thin-section analysis results, Lithofacies #1 is classified as fossiliferous wackestones and mainly consists of silt-sized and microcrystalline dolomite. There are small amounts of k-

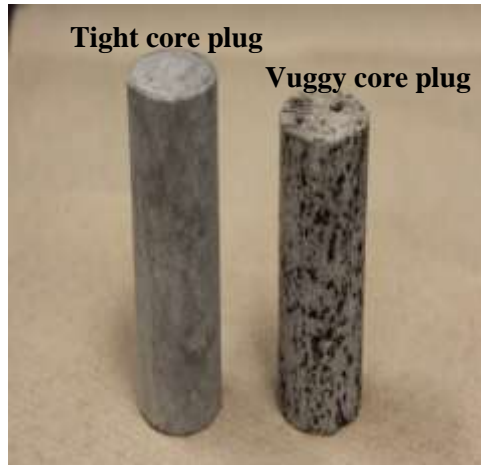
Table 4.1 (a) Petrographic properties of five Steelman rock samples.

Sample No.	1	2	3	4	5
Well No.	101/13-19-004-05W2/00		101/15-14-004-06W2/00		101/03-04-004-05W2/00
Depth (m)	1426.2	1453.3	1454.5	1483.2	1491.1
Petrofacies	Lithofacies #1	Lithofacies #2	Lithofacies #1	Lithofacies #2	Lithofacies #2
Rock type	fossiliferous wackestone	peloidal grainstone	fossiliferous wackestone	peloidal grainstone	calcareous mudstone
Pore type (fabric selective)					
Microporosity	abundant	abundant	abundant	abundant	abundant
Interparticle	–	trace	–	minor	–
Intraparticle	minor	minor	–	–	–
Pore type (non fabric selective)					
Pin-point vug	minor–trace	minor–common	common	common	minor–common
Vug	minor	abundant	–	major	abundant
Fracture	–	–	–	minor	–
Reservoir characteristics					
Estimated ϕ (%)	5–20	15–25	15–25	5–15	15–25
Estimated k_{\max} (mD)	<2.0	10–100	<2.0	<2.0	>500

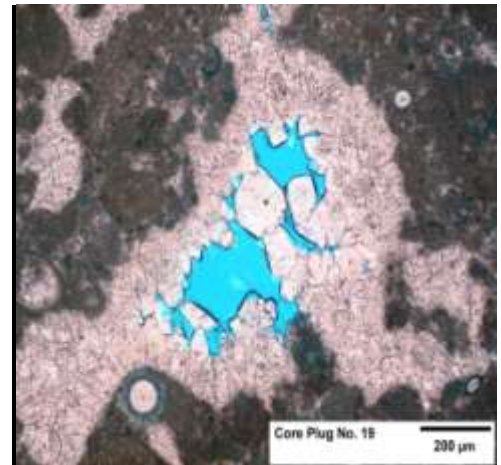
Table 4.1 (b) Mineralogical properties of five Steelman rock samples.

Component	Density (g/cm ³)	Sample composition (wt.%)				
		#1	#2	#3	#4	#5
Quartz	2.65	3.3	3.0	2.1	2.6	0.7
K-feldspar	2.58	7.5	0.0	2.3	0.0	0.0
Calcite	2.71	21.9	97.0	11.5	97.4	99.3
Dolomite	2.84	67.3	0.0	84.1	0.0	0.0
Total		100.0	100.0	100.0	100.0	100.0
Density* (g/cm ³)		2.79	2.71	2.82	2.71	2.71

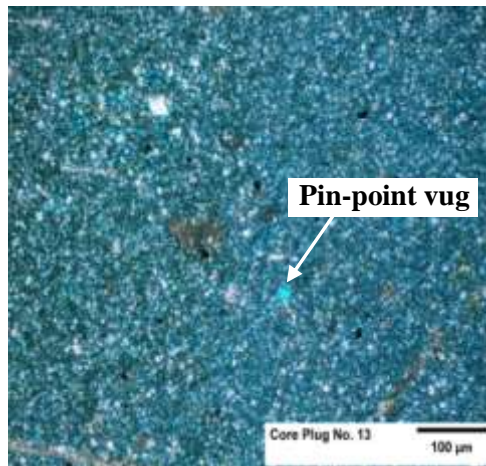
*The calculated grain density of the bulk rock sample.



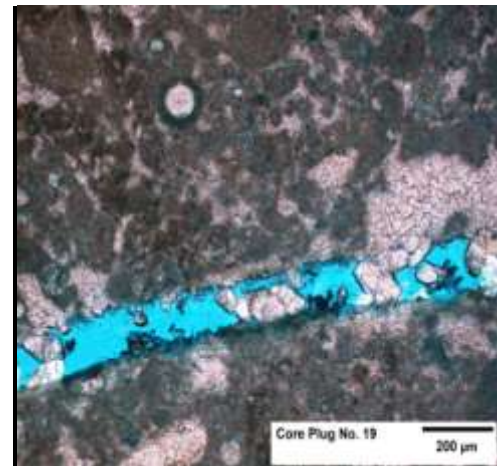
(a)



(c)



(b)



(d)

Figure 4.1 (a) Digital photograph of two rock samples from the Midale layer (tight core plug) and the Frobisher layer (vuggy core plug); (b) Photomicrograph of the tight rock sample with pin-point vugs; (c) Photomicrograph of the vuggy rock sample with a vug; and (d) Photomicrograph of the vuggy rock sample with a natural fracture.

feldspar, monocrystalline quartz, chalcedony, pyrite, clay, carbonaceous material and phosphate. The main source of porosity is the micro-intergranular porosity from the microcrystalline dolomite and the total porosity is estimated to be 5–25%, whereas the measured porosities range from 10.58% to 14.31% prior to the coreflood tests in this study. Since the micropores are too small, the absolute permeability is estimated to be lower than 2.0 mD. The measured absolute permeabilities of the tight reservoir core plugs are lower than 0.1 mD. Due to the variation in grain-size in Lithofacies #1, fine solids may migrate through the pore network and block pore-throats, leading to a large permeability reduction [Moghadasi *et al.*, 2004].

On the other hand, Lithofacies #2 is classified as peloidal grainstones and calcareous mudstones. The rock samples of Lithofacies #2 are dominantly composed of calcite with a small amount of quartz in the form of silt-sized monocrystalline quartz grains. The main sources of porosity are vugs, pin-point vugs, and microporosity. The total estimated porosity ranges from 5% to 25% and the measured porosities are 11.70–13.12% prior to the coreflood tests. The thin-section analysis result also shows that the micropores in Lithofacies #2 are even smaller than those in Lithofacies #1. With the existence of the high-permeability vugs and fractures, the estimated absolute permeability is in an extremely large range from lower than 2.0 mD to higher than 500 mD. The measured permeabilities of the vuggy reservoir core plugs are in the range of 2.122–11.379 mD, which indicates that the overall connectivities among the vugs are poor. In comparison with the estimated porosity and permeability from the thin-section analysis, the measured values prior to the coreflood tests in this work are more specific and accurate.

4.2 Mutual Interactions Between the Light Crude Oil and CO₂

4.2.1 Measured equilibrium IFTs and MMP

In this study, the equilibrium IFTs between the Steelman light crude oil and CO₂ at different equilibrium pressures were measured by applying the ADSA technique for the pendant drop case. The measured equilibrium IFTs between the Steelman light crude oil and CO₂ at seventeen different equilibrium pressures of $P_{eq} = 1.08\text{--}18.66$ MPa and $T_{res} = 51.1^\circ\text{C}$ are plotted in Figure 4.2. It is found that the measured equilibrium IFT is reduced almost linearly with the equilibrium pressure in two distinct pressure ranges: Range I ($P_{eq} = 1.08\text{--}8.74$ MPa) and Range II ($P_{eq} = 8.74\text{--}18.66$ MPa). The measured equilibrium IFTs at different pressures are between different intermediate to heavy HCs of the original light crude oil with dissolved CO₂ and the CO₂ phase with different amounts of light to intermediate HCs extracted in the second and possibly first equilibrium pressure ranges [Cao and Gu, 2013b]. On the basis of the measured data in Figure 4.2, the equilibrium IFT γ_{eq} (mJ/m²) is correlated to the equilibrium pressure P_{eq} (MPa) by applying the linear regression in the above-mentioned two equilibrium pressure ranges, respectively:

$$\gamma_{eq} = -2.109 P_{eq} + 22.858 \quad (1.08 \text{ MPa} \leq P_{eq} \leq 8.74 \text{ MPa}, R^2 = 0.996), \quad (4.1)$$

$$\gamma_{eq} = -0.341 P_{eq} + 8.046 \quad (8.74 \text{ MPa} \leq P_{eq} \leq 18.66 \text{ MPa}, R^2 = 0.948). \quad (4.2)$$

For the Steelman light crude oil–CO₂ system, the linear regression equation of the measured equilibrium IFT versus equilibrium pressure data for Range I intersects with the abscissa (i.e., $\gamma_{eq} = 0$) at $P_{eq} = 10.8$ MPa. Therefore, the multi-contact miscibility (MCM) pressure or the MMP of this light crude oil–CO₂ system at $T_{res} = 51.1^\circ\text{C}$ is determined to be 10.8 MPa by applying the VIT technique. The applicability, reliability,

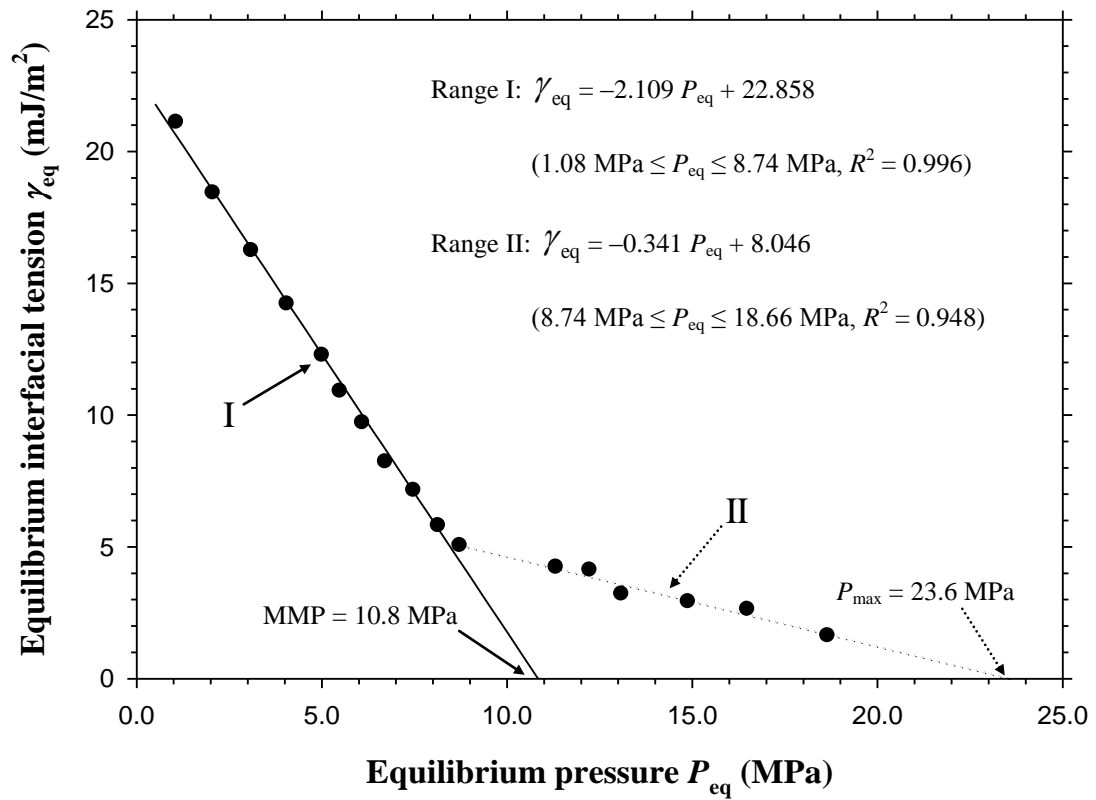


Figure 4.2 Measured equilibrium interfacial tensions (IFTs) between the Steelman light crude oil and CO₂ at different equilibrium pressures and $T_{res} = 51.1$ °C.

and accuracy of the VIT technique for determining the MMP have been discussed in the literature [Rao, 1997; Rao and Lee, 2002; Nobakht *et al.*, 2008]. In addition, the miscibility pressure between the intermediate to heavy HCs of this light crude oil and CO₂ is found to be $P_{\max} = 23.6$ MPa from the extrapolation of the linear regression equation for Range II, which is roughly referred to as the first-contact miscibility (FCM) pressure.

4.2.2 Oil-swelling effect and light-HCs extraction phenomenon

After the pendant oil drop was formed and surrounded by CO₂ phase inside the high-pressure cell, it was observed that its volume and shape were changed continuously. At a low equilibrium pressure, the pendant oil drop initially swelled slightly and then shrank slowly. The sequential digital images of the dynamic pendant oil drops and their drop volumes at $P_{\text{eq}} = 4.1$ MPa and $T_{\text{res}} = 51.1$ °C are shown in Figure 4.3a at four different times, $t = 0, 850, 900,$ and $3,600$ s. It is clearly seen from this figure that the dynamic pendant oil drop volume was increased slightly at the beginning ($t \leq 850$ s) due to the initial oil-swelling effect as CO₂ was gradually dissolved into the crude oil. Afterwards, the dynamic pendant oil drop volume was reduced considerably as a result of the subsequent slow light-HCs extraction from the oil phase to CO₂ phase. This indicates that although two-way mass transfer may occur at all times, the oil-swelling effect due to CO₂ dissolution into the oil phase is more pronounced at the beginning ($t \leq 850$ s), whereas the oil-shrinking effect due to the subsequent slow light-HCs extraction from the oil phase to CO₂ phase becomes dominant at a large time (e.g., $t > 850$ s) [Yang and Gu, 2005].

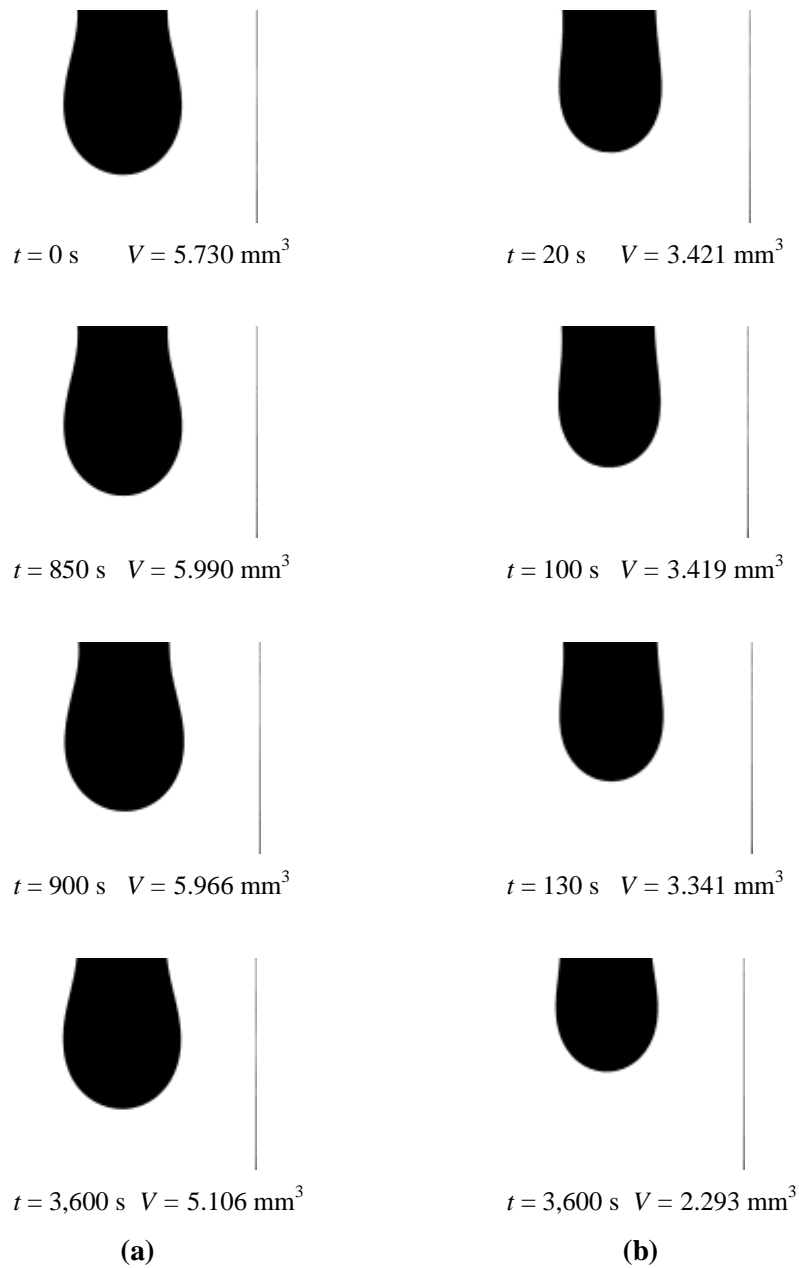


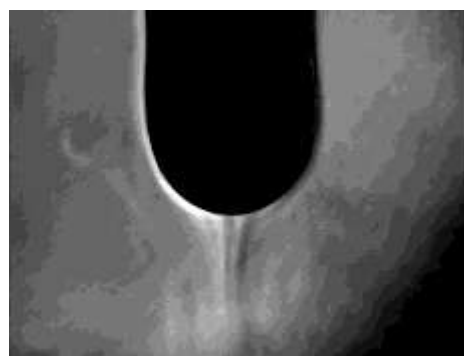
Figure 4.3 Sequential digital images of the Steelman crude oil pendant drops surrounded by CO₂ at **(a)** $P_{eq} = 4.1$ MPa during the initial oil-swelling process (e.g., at $t = 0, 850$ s) and the subsequent slow light-hydrocarbons (HCs) extraction process (e.g., at $t = 900, 3,600$ s); **(b)** $P_{eq} = 7.5$ MPa during the initial almost constant-volume stage (e.g., at $t = 0, 100$ s) and the subsequent slow light-HCs extraction process (e.g., at $t = 130, 3,600$ s).

At a higher equilibrium pressure, no initial volume increase happened to the pendant oil drop from the very beginning. The sequential digital images of the dynamic pendant oil drops and their volumes at $P_{\text{eq}} = 7.5$ MPa and $T_{\text{res}} = 51.1$ °C are shown in Figure 4.3b at four different times, $t = 20, 100, 130,$ and $3,600$ s. At this relatively high equilibrium pressure, the intensity of the initial light-HCs extraction effect is equal to (if not stronger than) the intensity of the initial oil-swelling effect. The oil-shrinking effect and the oil-swelling effect were offset with each other in this period. As a result, the volume of the pendant oil drop kept almost constant at the beginning ($t \leq 100$ s) and then decreased continuously because the subsequent slow light-HCs extraction becomes dominant at a large time (e.g., $t > 100$ s).

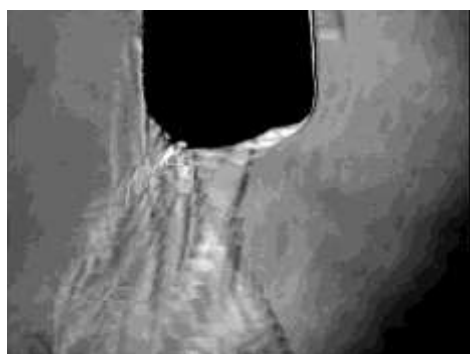
At an even higher equilibrium pressure, the initial quick light-HCs extraction became much stronger. The initial and quick light-HCs extraction process at the MMP = 10.8 MPa and $T_{\text{res}} = 51.1$ °C was observed and a series of six digital images of the light-HCs extraction by the supercritical CO₂ are shown in Figure 4.4. These digital images were taken at $t = 0, 5, 10, 60, 80,$ and 100 s after the original Steelman light crude oil was introduced and formed as a pendant oil drop and surrounded by CO₂. It is worthwhile to note that the light crude oil was continuously introduced from an original light crude oil sample cylinder and added into the existing pendant oil drop during this extraction process until a large and stable pendant oil drop was formed at the end for the equilibrium IFT measurement. As shown in Figure 4.4, the original oil drop formed at the needle tip was quickly extracted by CO₂ at the MMP and the actual reservoir temperature. In general, it took about 100 s for the initial and quick light-HCs extraction to be completed.



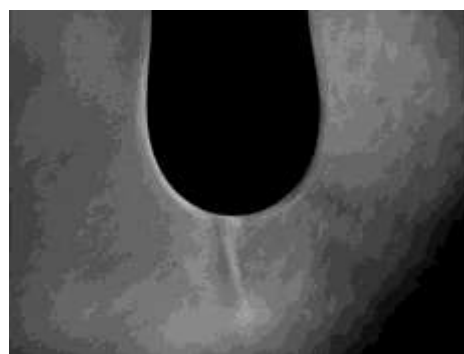
$t = 0 \text{ s}$



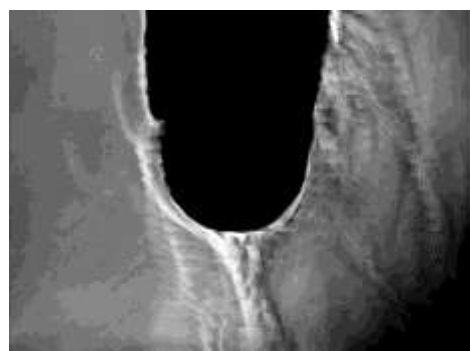
$t = 60 \text{ s}$



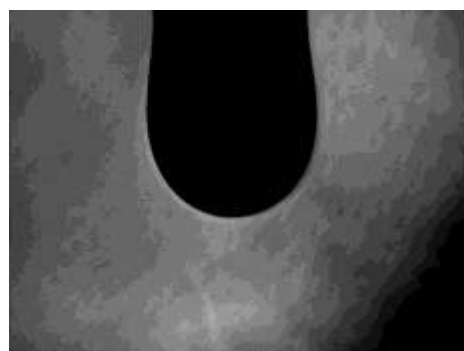
$t = 5 \text{ s}$



$t = 80 \text{ s}$



$t = 10 \text{ s}$



$t = 100 \text{ s}$

Figure 4.4 Sequential digital images of the initial and quick light-hydrocarbons (HCs) extraction by the supercritical CO_2 ($P_{\text{eq}} = \text{MMP} = 10.8 \text{ MPa}$ and $T_{\text{res}} = 51.1 \text{ }^\circ\text{C}$) at different times.

Similar to the CO₂ displacement front in an actual CO₂ flooding case, the CO₂ phase kept contacting the newly encountered fresh light crude oil and extracted its light HCs in this period. As indicated by this figure, the light-HCs extraction by the supercritical CO₂ at the MMP = 10.8 MPa and $T_{\text{res}} = 51.1$ °C was quick and strong. This figure also helps to better understand the concepts and processes of the MCM and FCM, as well as the major reason for a high oil RF of a miscible CO₂ flooding process.

4.3 CO₂-EOR in a Tight MPZ and in a Vuggy ROZ

4.3.1 Production pressure effect

In this study, four CO₂ secondary flooding tests (Tests #1–4) at different production pressures of $P_{\text{prod}} = 2.0, 6.5, 11.0,$ and 14.0 MPa were carried out in the tight reservoir core plugs to study the production pressure effect on CO₂ flooding in the tight MPZ. Three CO₂ tertiary flooding tests (Tests #8–10) at $P_{\text{prod}} = 6.5, 11.0,$ and 14.0 MPa were conducted in the waterflooded vuggy reservoir core plugs to evaluate CO₂-EOR in the vuggy ROZ. The detailed physical properties of the carbonate reservoir core plugs, experimental conditions, and oil RFs of these seven CO₂ coreflood tests are summarized in Table 4.2. The measured oil RFs in terms of the OOIP versus the injected PV of CO₂ in Tests #1–4 with the tight core plugs are shown in Figure 4.5a. As expected, the oil RF increased quickly with the injected PV of CO₂ and finally reached a maximum value. At a higher production pressure, the initial quick oil production stage had a higher oil production rate but was shorter. Figure 4.5b depicts the final oil RFs of these four tests at four different production pressures. This figure shows that the final oil RF is increased almost linearly and monotonously with the production pressure from 2.0 to 14.0 MPa.

Table 4.2 Physical properties of the composite carbonate reservoir core plugs from the Steelman oilfield, experimental conditions, oil recovery factors of ten CO₂-based coreflood tests at $q_{\text{brine}} = 0.025 \text{ cm}^3/\text{min}$, $q_{\text{CO}_2} = 0.1 \text{ cm}^3/\text{min}$, $T_{\text{res}} = 51.1 \text{ }^\circ\text{C}$, and the MMP = 10.8 MPa.

Core plugs	Test No.	CO ₂ flooding	k (mD)	ϕ (%)	S_{oi} (%)	P_{inj} (MPa)	P_{prod} (MPa)	RF _w (%)	S_{or} (%)	RF _{CO₂} ^a (%)	RF _{total} (%)	RF _{CO₂} ^b (%)
Tight	1	Secondary	0.091	13.29	43.59	10.4	2.0	—	—	50.88	50.88	—
	2		0.082	12.27	47.29	14.4	6.5	—	—	68.43	68.43	—
	3		0.086	14.31	39.40	18.8	11.0	—	—	79.20	79.20	—
	4		0.088	13.90	39.22	22.0	14.0	—	—	87.50	87.50	—
	5		0.019	11.22	37.02	25.0	9.0	—	—	82.05	82.05	—
	6	Tertiary	0.093	10.58	46.22	20.3	11.0	31.36	31.72	58.19	89.55	84.77
Vuggy	7	Secondary	6.631	13.12	33.57	11.2	11.0	—	—	35.96	35.96	—
	8	Tertiary	11.379	13.10	38.63	6.6	6.5	11.11	34.33	33.33	44.44	37.50
	9		2.122	13.12	41.14	11.4	11.0	10.42	36.86	62.50	72.92	69.77
	10		9.927	11.70	42.47	14.5	14.0	18.87	34.46	57.36	76.23	70.70

- Notes: k : absolute permeability of two carbonate reservoir core plugs
 ϕ : porosity of two carbonate reservoir core plugs
 S_{oi} : initial oil saturation
 P_{inj} : initial CO₂ injection pressure at the inlet of coreholder
 P_{prod} : production pressure at the outlet of coreholder
RF_w: oil recovery factor (RF) of waterflooding in terms of the original oil-in-place (OOIP)
 S_{or} : residual oil saturation after waterflooding
RF_{CO₂}^a: oil RF of CO₂ flooding in terms of the OOIP
RF_{total}: total oil RF of waterflooding and CO₂ flooding in terms of the OOIP
RF_{CO₂}^b: oil RF of CO₂ flooding in terms of the residual oil-in-place (ROIP)

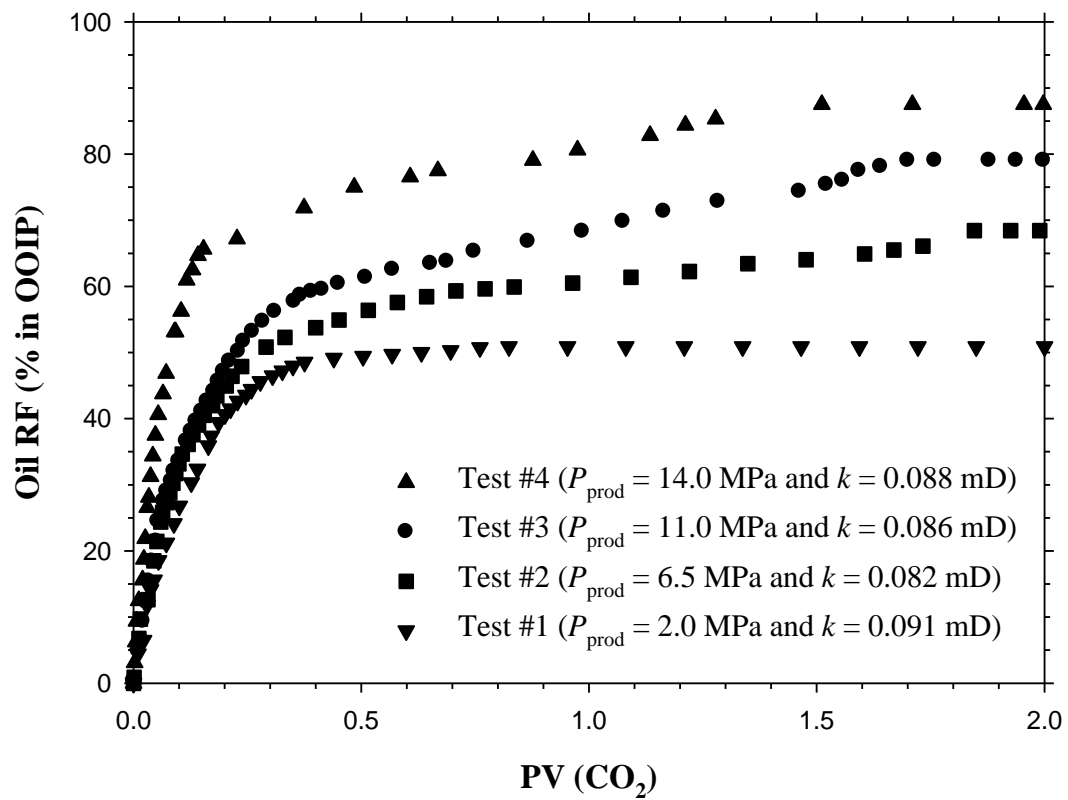


Figure 4.5 (a) Measured oil RFs of CO₂ secondary flooding versus the PV of injected CO₂ in Tests #1–4 with the tight core plugs.

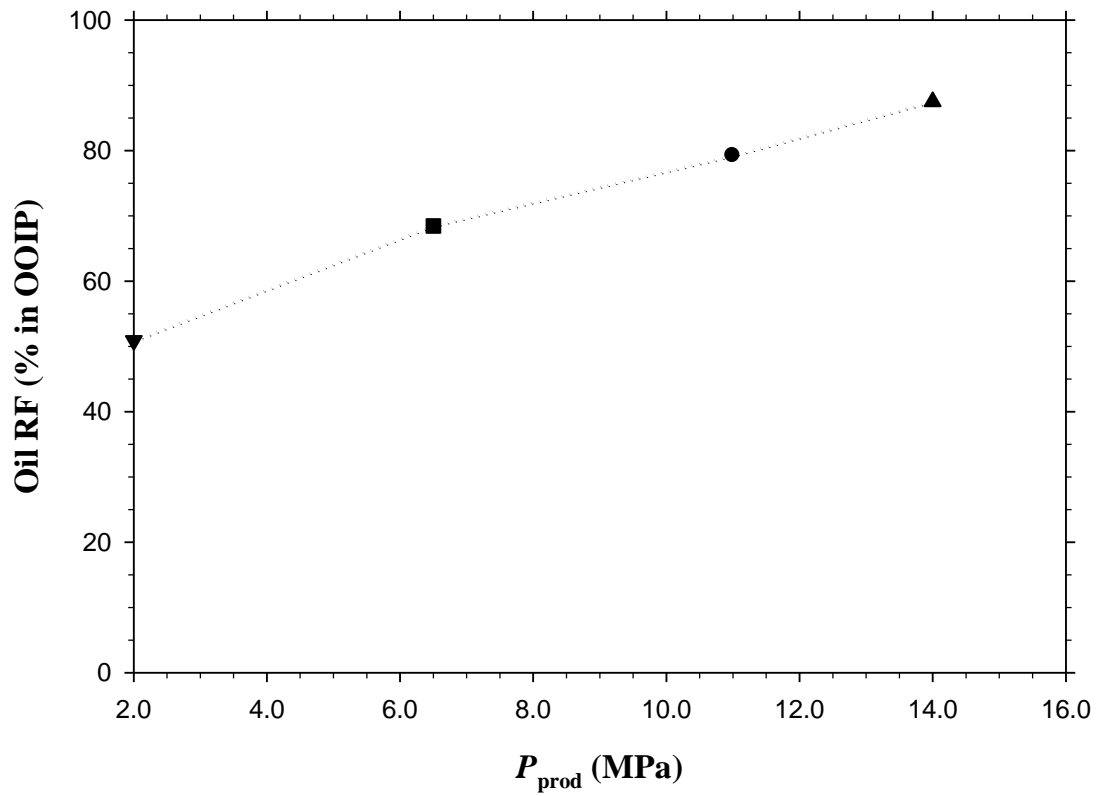


Figure 4.5 (b) Measured final oil RFs of CO₂ secondary flooding in terms of the OOIP versus the production pressure at $P_{\text{prod}} = 2.0$ MPa (Test #1), 6.5 MPa (Test #2), 11.0 MPa (Test #3), and 14.0 MPa (Test #4) with the tight core plugs.

The high final oil RFs indicate that miscible or even immiscible CO₂ secondary flooding is an effective method to recover the light oil from the tight MPZ [Gong and Gu, 2015a].

In Tests #1–4, CO₂ injection pressures at the inlet of the coreholder were much higher than the pre-specified production pressures at the outlet of the coreholder due to the ultra-low permeabilities of these tight carbonate reservoir core plugs, $k = 0.082\text{--}0.091$ mD. The initial CO₂ injection pressures in Tests #1–4 were equal to 10.4, 14.4, 18.8, and 22.0 MPa, corresponding to the production pressures of 2.0, 6.5, 11.0, and 14.0 MPa, respectively. In Test #4, the highest CO₂ injection pressure, which was close to the FCM pressure of $P_{\max} = 23.6$ MPa, led to the highest oil RF. For the two immiscible CO₂ flooding tests (Tests #1 and #2) in terms of their production pressures, the initial CO₂ injection pressures were either close to or higher than the MMP = 10.8 MPa. Consequently, CO₂ flooding process near the inlet of the coreholder was near-miscible (Test #1) or miscible (Test #2). With the strong IFT reduction and light-HCs extraction of the high-pressure CO₂ near the inlet, its microscopic displacement efficiency or oil RF in the tight core plugs is increased with the production pressure, as shown in Figure 4.5b.

Figures 4.6a–c show the measured oil RFs, gas production rates, and cumulative water production data in Tests #8–10 with the vuggy core plugs at three different production pressures. In these three waterflooding plus CO₂ tertiary flooding tests, water production started and water BT occurred almost immediately after waterflooding due to relatively high connate water saturations and relatively high permeabilities of the vuggy core plugs. The oil RFs of waterflooding in Tests #8–10 were equal to 11.11%, 10.42%, and 18.87%, respectively. The overall sweep efficiency of waterflooding was quite low in

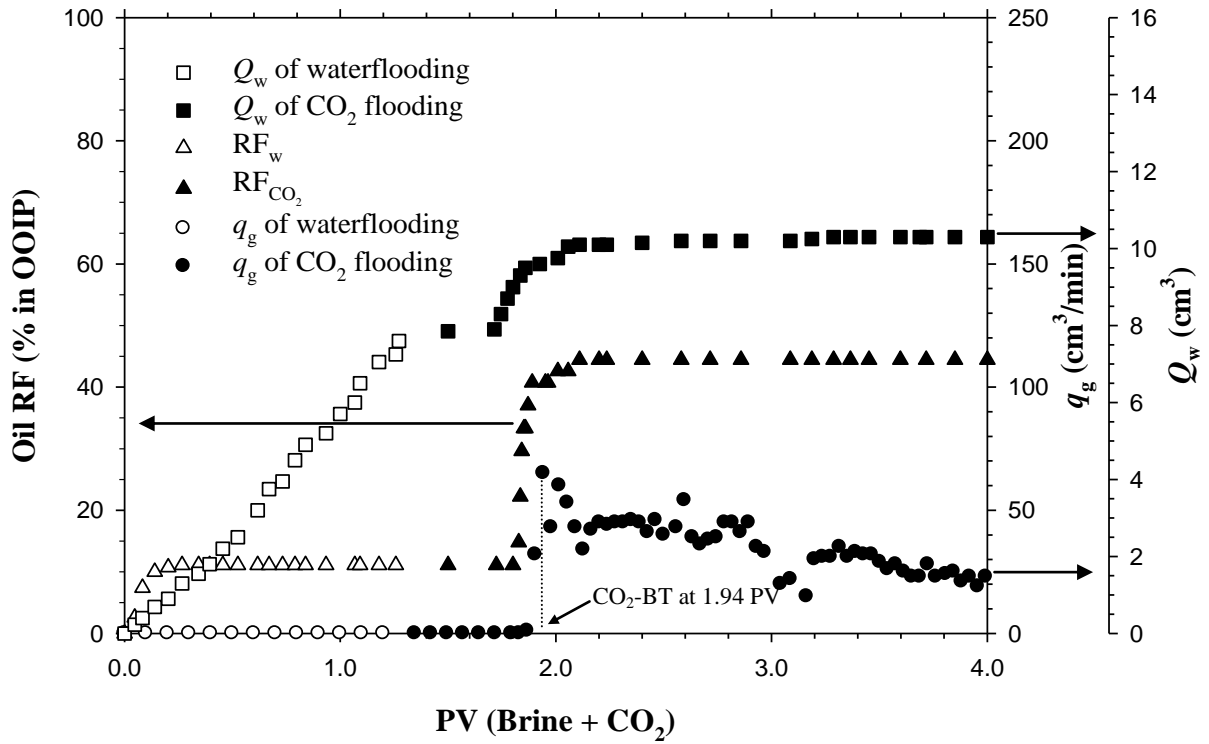


Figure 4.6 (a) Measured oil RFs, gas production rates (q_g), and cumulative water production data (Q_w) versus the PV of injected brine and CO₂ in Test #8 (waterflooding + immiscible CO₂ tertiary flooding) with the vuggy core plugs at $P_{\text{prod}} = 6.5$ MPa.

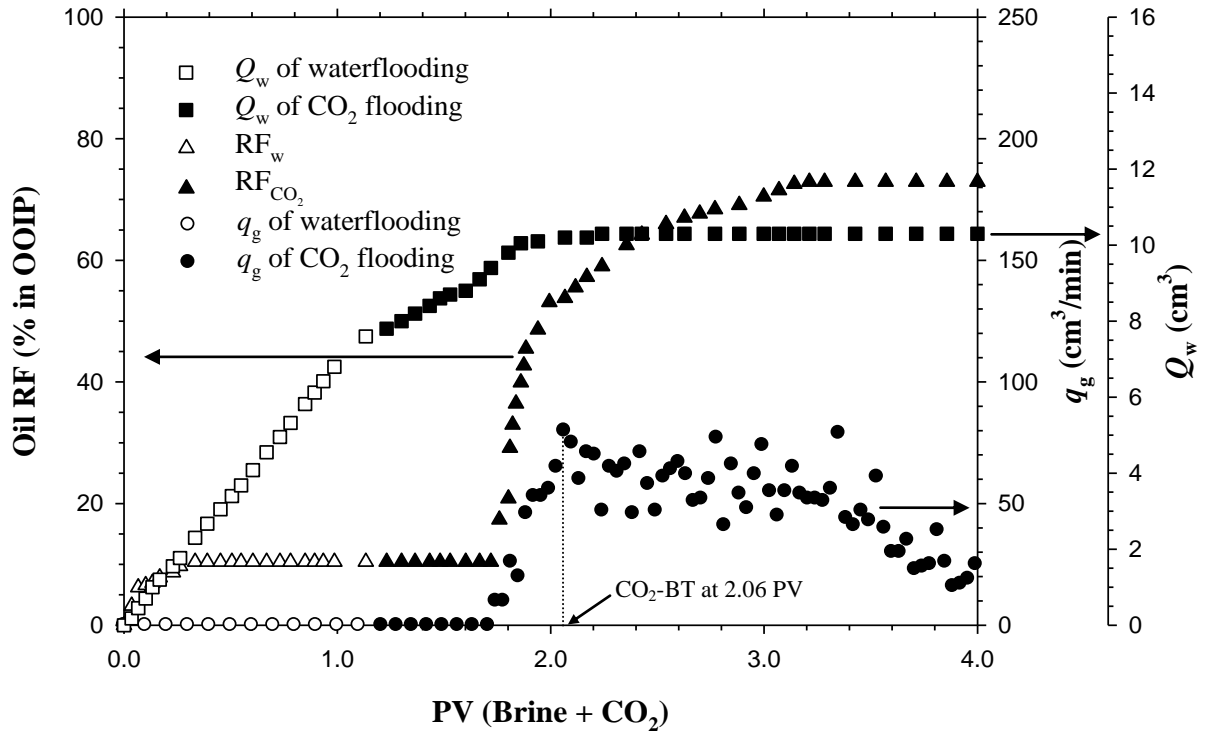


Figure 4.6 (b) Measured oil RFs, gas production rates (q_g), and cumulative water production data (Q_w) versus the PV of injected brine and CO₂ in Test #9 (waterflooding + miscible CO₂ tertiary flooding) with the vuggy core plugs at $P_{\text{prod}} = 11.0$ MPa.

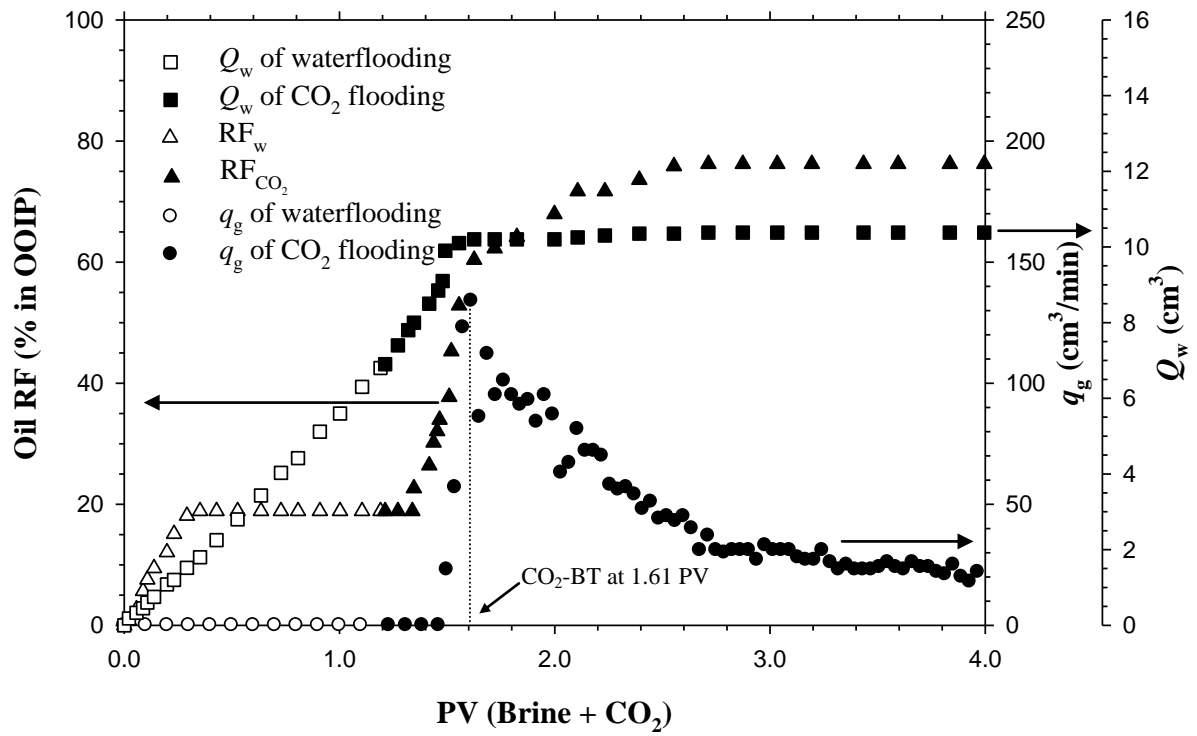


Figure 4.6 (c) Measured oil RFs, gas production rates (q_g), and cumulative water production data (Q_w) versus the PV of injected brine and CO₂ in Test #10 (waterflooding + miscible CO₂ tertiary flooding) with the vuggy core plugs at $P_{\text{prod}} = 14.0$ MPa.

the vuggy core plugs. After the vuggy ROZ was formed post waterflooding, the subsequent CO₂ tertiary flooding process can be approximately divided into three fluid production stages, based on the measured oil RFs, gas production rates, and cumulative water production data in Figures 4.6a–c. In the first stage, only water was produced and there was neither oil nor gas production. The injected CO₂ displaced and produced the mobile water through the vuggy core plugs. In the second stage, CO₂-saturated oil was produced quickly with a low to moderate gas production rate, while water production was quickly diminished as most mobile water had already been produced in the first stage. In the third stage, CO₂-BT occurred when the gas production rate reached a peak value and the oil production rate was reduced gradually. The light to intermediate HCs extraction by CO₂ becomes an important CO₂-EOR mechanism in the last stage [Cao and Gu, 2013b]. It is also found from these three figures that the gas production rate at the CO₂-BT and the total oil RF in terms of the OOIP were increased with the production pressure, whereas the cumulative water production remained almost the same in Tests #8–10. In addition, as indicated in Table 4.2, the CO₂ flooding processes in the waterflooded vuggy core plugs had much smaller pressure differences between the inlet and outlet of the coreholder than those in the tight core plugs.

Figure 4.6d summarizes and compares the total oil RFs of waterflooding and CO₂ tertiary flooding in terms of the OOIP, the oil RFs of CO₂ tertiary flooding in terms of the ROIP, and the oil RFs of CO₂ tertiary flooding after CO₂-BT in terms of the ROIP in Tests #8–10. It is seen from this figure that there is a sudden slope change at the MMP in each oil RF versus the production pressure curve for the vuggy core plugs. In this case, the oil RF dependence on the production pressure has a different trend when the

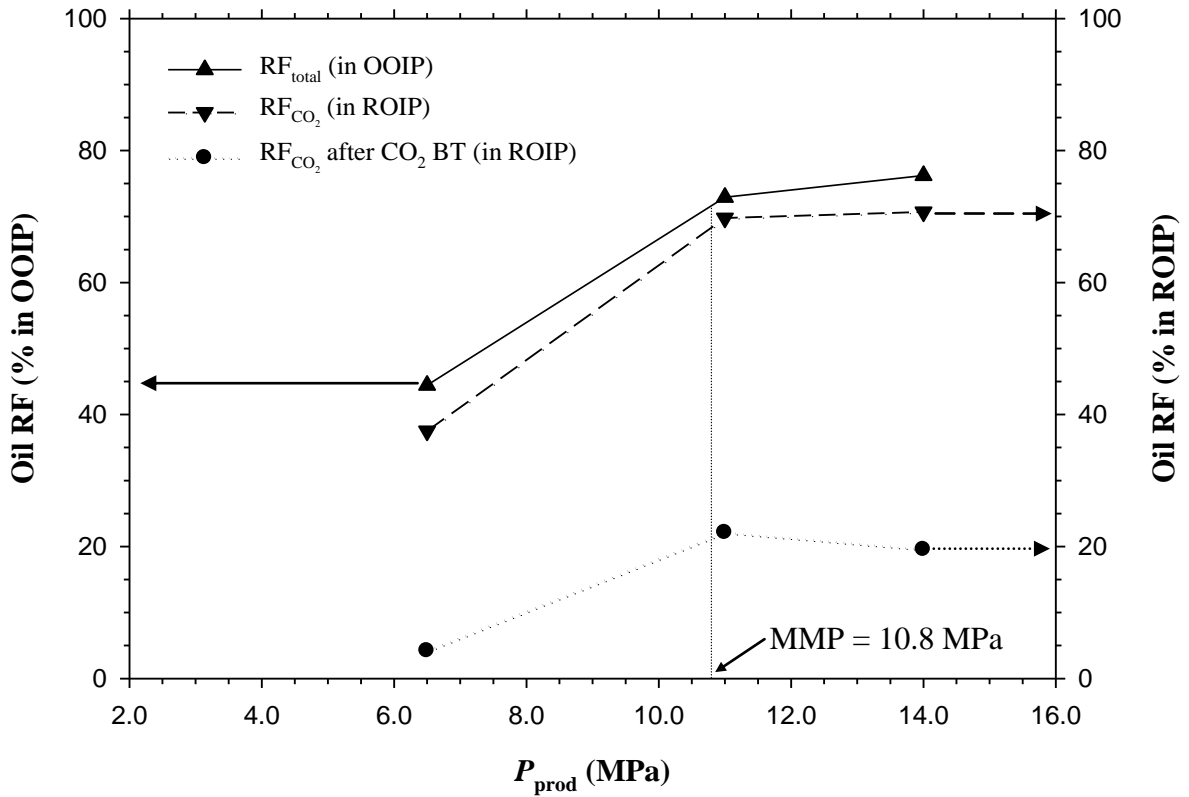


Figure 4.6 (d) Measured total oil RFs of waterflooding and CO₂ tertiary flooding in terms of the OOIP, oil RFs of CO₂ tertiary flooding in terms of the ROIP, and oil RFs of CO₂ tertiary flooding after CO₂-BT in terms of the ROIP versus the production pressure at $P_{\text{prod}} = 6.5$ MPa (Test #8), 11.0 MPa (Test #9), and 14.0 MPa (Test #10) with the vuggy core plugs.

production pressure is below or above the MMP [Gong and Gu, 2015a]. Overall, CO₂ tertiary flooding after waterflooding recovered 37.50%, 69.77%, and 70.70% of the ROIP in Tests #8–10, respectively. These experimental data indicate that the miscible CO₂ tertiary flooding process (Test #9 or #10) is far more effective than the immiscible CO₂ tertiary flooding process (Test #8) to recover the residual oil in the vuggy ROZ after waterflooding. Furthermore, two miscible CO₂ tertiary flooding tests at the production pressures of $P_{\text{prod}} = 11.0$ MPa (Test #9) and 14.0 MPa (Test #10) still recovered 22.09% and 19.53% of the ROIP in the third stage after CO₂-BT, respectively. After CO₂-BT, supercritical CO₂ can still effectively extract some light to intermediate HCs from the residual oil so that they are produced along with the CO₂ phase at a high production pressure. In the immiscible CO₂ tertiary flooding test at the production pressure of $P_{\text{prod}} = 6.5$ MPa (Test #8), however, the oil production was almost finished at the end of the second stage and only 4.17% of the ROIP was recovered in the third stage.

4.3.2 Permeability and vug effects

In this study, two CO₂ secondary flooding tests were undertaken with two different tight reservoir core plugs of $k = 0.086$ mD in Test #3 and 0.019 mD in Test #5 to examine the permeability effect on the oil RF in the tight MPZ. The measured oil RFs and gas production rates versus the injected PV of CO₂ in Tests #3 and #5 are plotted and compared in Figure 4.7. This figure shows that both the oil RF and the gas production rate in Test #5 ($k = 0.019$ mD) were lower than those in Test #3 ($k = 0.086$ mD) till 0.60 PV, whereas the CO₂-BT occurred at 0.29 PV in Test #5 and 0.17 PV in Test #3. These three experimental data indicate that miscible CO₂ displacement front moves more slowly

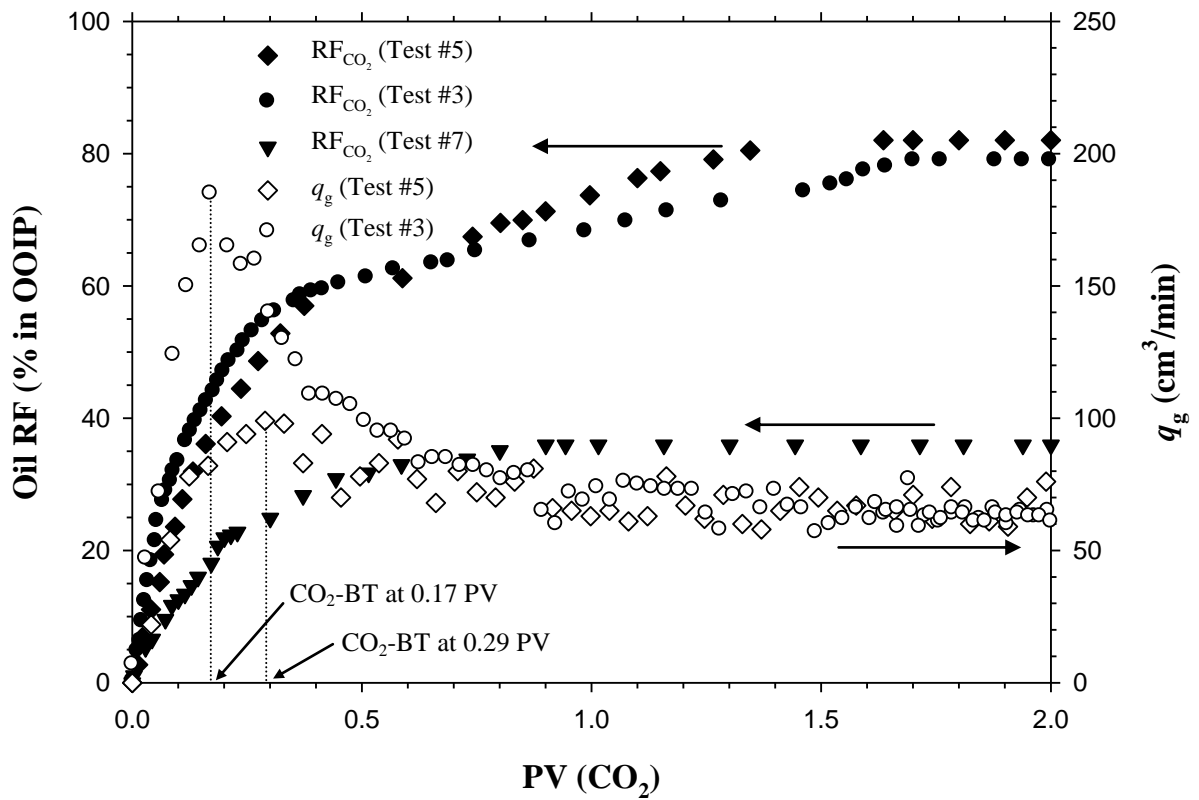


Figure 4.7 Measured oil RFs of CO₂ secondary flooding versus the PV of injected CO₂ in Test #3 ($k = 0.086$ mD for the tight core plugs and $P_{\text{prod}} = 11.0$ MPa), Test #5 ($k = 0.019$ mD for the tight core plugs and $P_{\text{prod}} = 9.0$ MPa), and Test #7 ($k = 6.631$ mD for the vuggy core plugs and $P_{\text{prod}} = 11.0$ MPa), as well as measured gas production rates (q_g) versus the PV of injected CO₂ in Tests #3 and #5.

and uniformly so that CO₂ interacts more strongly with the light oil in the lower-permeability core plugs at the early stage of CO₂ secondary flooding. After 0.60 PV, both the oil RF and the gas production rate in Test #5 surpassed those in Test #3 till 2.00 PV. It is worthwhile to note that in Test #5, CO₂ injection pressure was 25.0 MPa at the beginning, which was higher than the FCM pressure of $P_{\max} = 23.6$ MPa. It was the slower motion of miscible CO₂ displacement front and the higher injection pressure that jointly resulted in a slightly higher final oil RF in Test #5, though it had a lower production pressure of $P_{\text{prod}} = 9.0$ MPa than $P_{\text{prod}} = 11.0$ MPa in Test #3. On the other hand, the higher CO₂ injection pressure in Test #5 also indicates that CO₂ injectivity in the tighter MPZ is lower.

The third CO₂ secondary flooding test (Test #7) was performed in the vuggy reservoir core plugs of $k = 6.631$ mD and compared with Test #3 to study the vug effect on the oil RF in the vuggy ROZ, both of which were conducted at the same production pressure of $P_{\text{prod}} = 11.0$ MPa. As shown in Figure 4.7, unlike the miscible CO₂ secondary flooding in the tight core plugs (Test #3), the miscible CO₂ secondary flooding in the vuggy core plugs had a much lower oil production rate at the beginning and an extremely lower oil RF at the end. No more oil was produced after 0.90 PV and the final oil RF of Test #7 was only 35.96% of the OOIP. This is because the vugs and micro-fractures of the vuggy core plugs, as shown in Figures 4.1c and d, formed high-permeability channels for high-mobility CO₂ to readily breakthrough in Test #7. After CO₂-BT, the subsequently injected CO₂ followed the established high-permeability channels and left a large amount of the original light crude oil untouched. Obviously, miscible CO₂ secondary flooding is ineffective to recover the light oil from the vuggy zone due to the presence of vugs and

natural micro-fractures. Alternatively, miscible CO₂ tertiary flooding after waterflooding may be applied to achieve a high total oil RF in the vuggy zone.

4.3.3 Miscible CO₂ secondary/tertiary flooding

In this work, CO₂ injection timing was studied for both the tight and vuggy reservoir core plugs by comparing the miscible CO₂ secondary and tertiary flooding processes. Tests #3 and #6 were miscible CO₂ secondary and tertiary flooding tests in the tight core plugs. These two tests were conducted at the same production pressure of $P_{\text{prod}} = 11.0$ MPa to ensure that two CO₂ flooding processes were miscible along the entire coreholder. The measured oil RFs and gas production rates in Tests #3 and #6 as well as cumulative water production data in Test #6 are plotted and compared in Figure 4.8. It is worthwhile to note that there was no water production in the miscible CO₂ secondary flooding (Test #3). In the miscible CO₂ tertiary flooding after waterflooding process (Test #6), water production started almost from the beginning of waterflooding. The subsequent miscible CO₂ tertiary flooding started at 0.84 PV. As shown in Figure 4.8, the miscible CO₂ tertiary flooding process in the tight core plugs can also be roughly divided into three fluid production stages, similar to those in Tests #8–10 with the vuggy core plugs. The first water production stage produced neither oil nor gas. The second oil production stage prior to CO₂-BT had little water production but low to moderate gas production. The third gas production stage occurred after CO₂-BT with no water production but low to moderate oil production. In general, the residual oil after waterflooding was surrounded or shielded by the mobile water. The subsequently injected CO₂ first displaced the mobile water and then contacted the residual oil.

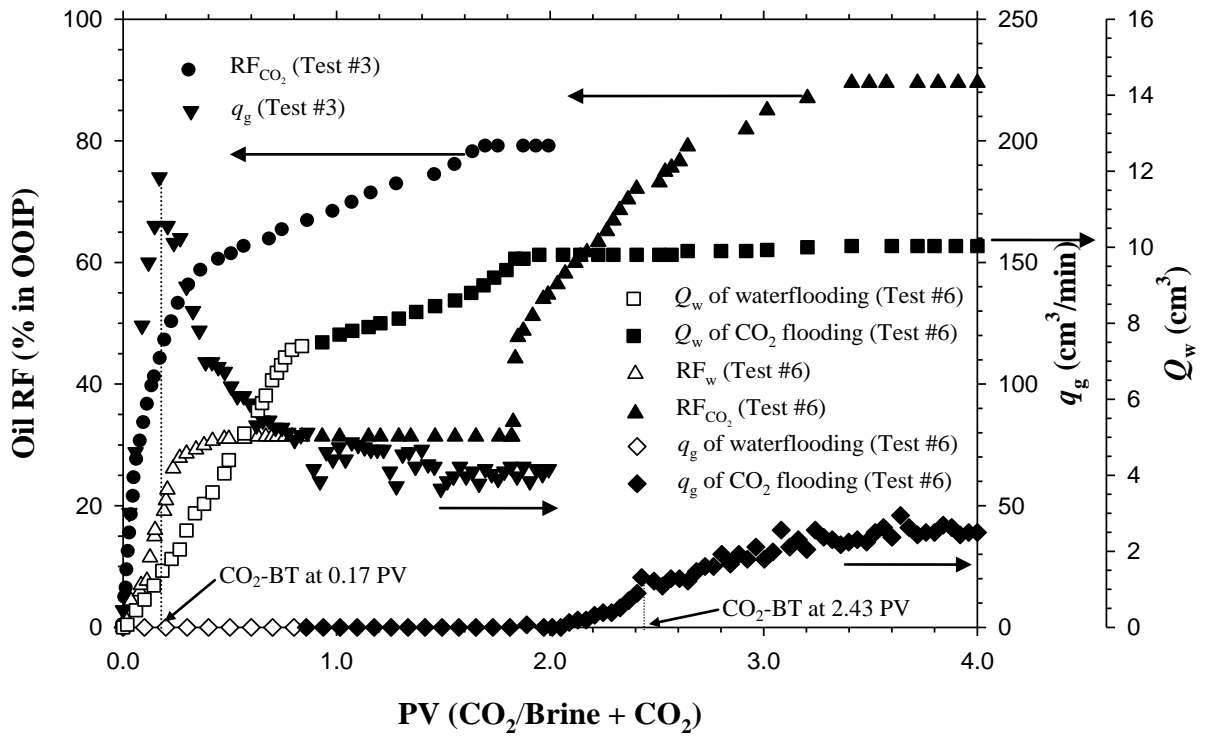


Figure 4.8 Measured oil RFs and gas production rates (q_g) versus the PV of injected CO₂ in Test #3 (miscible CO₂ secondary flooding) and injected brine and CO₂ in Test #6 (waterflooding + miscible CO₂ tertiary flooding) with the tight core plugs at $P_{\text{prod}} = 11.0$ MPa, as well as measured cumulative water production data (Q_w) versus the PV of injected brine and CO₂ in Test #6.

In Test #6, the waterflooding process recovered 31.36% of the OOIP and the subsequent miscible CO₂ tertiary flooding recovered 58.19% of the OOIP or 84.77% of the ROIP. The secondary waterflooding and the miscible CO₂ tertiary flooding in Test #6 jointly recovered 89.55% of the OOIP, which is much higher than the oil RF of waterflooding or CO₂ secondary flooding alone. On the other hand, in comparison with CO₂-BT at 0.17 PV for the miscible CO₂ secondary flooding (Test #3), CO₂-BT was significantly delayed to 1.59 PV of injected CO₂ in the miscible CO₂ tertiary flooding (Test #6) after waterflooding. The mobility of the subsequently injected CO₂ was well controlled by the initially injected water in Test #6. Moreover, the gas production rate in the CO₂ tertiary flooding (Test #6) was much lower than that in the CO₂ secondary flooding (Test #3), even after CO₂-BT. These experimental data indicate that the miscible CO₂ tertiary flooding after waterflooding is the most effective method to recover the light oil from the tight MPZ.

The measured oil RFs of the miscible CO₂ secondary (Test #7) and tertiary (Test #9) flooding processes in the vuggy core plugs are plotted and compared in Figure 4.9. The same production pressure of $P_{\text{prod}} = 11.0$ MPa was used in these two tests. Test #7 recovered 35.96% of the OOIP, which was much lower than 79.20% recovered in the miscible CO₂ secondary flooding in the tight core plugs (Test #3). Also, waterflooding in the vuggy core plugs (Test #9) resulted in an oil RF of 10.42%, which was much lower than 31.36% of waterflooding in the tight core plugs (Test #6). The vuggy core plugs led to a much lower oil RF of either CO₂ flooding or waterflooding because CO₂ or water flowed through the high-permeability channels more quickly and had a lower sweep efficiency. In Test #9 (Figure 4.6b), however, no CO₂ was produced until 0.57 PV CO₂

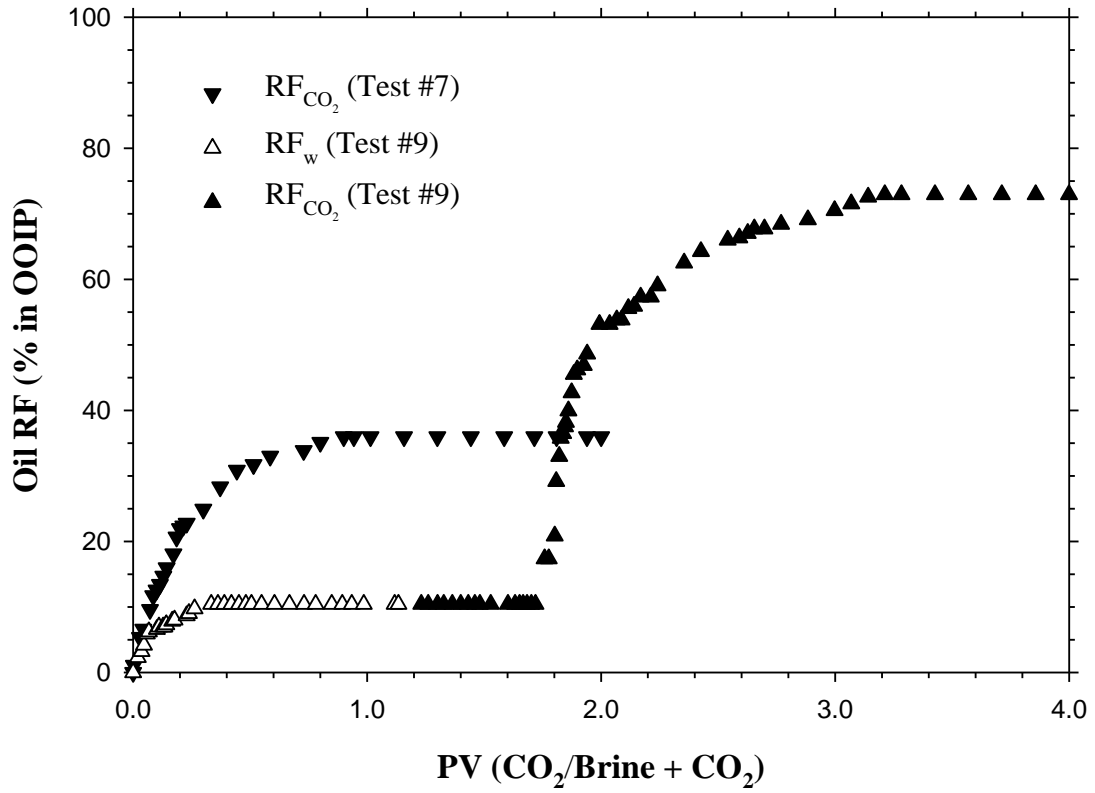


Figure 4.9 Measured oil RFs versus the PV of injected CO₂ in Test #7 (miscible CO₂ secondary flooding) and injected brine + CO₂ in Test #9 (waterflooding + miscible CO₂ tertiary flooding) with the vuggy core plugs at $P_{\text{prod}} = 11.0$ MPa.

was injected and the CO₂-BT did not occur until 0.93 PV CO₂ was injected. The CO₂ tertiary flooding delayed CO₂ production and BT so that its oil RF was higher than that of water or CO₂ injection alone. It was speculated that when CO₂ displaced water through the high-permeability channels, CO₂ bubbles were trapped in the poorly connected vugs and narrow pore throats and fractures. Thus, an additional pressure gradient was needed to overcome the threshold capillary pressure due to the so-called Jamin effect [Cosse, 1993]. Below certain pressure gradient, the trapped CO₂ bubbles forced the subsequently injected CO₂ to pass through the previously unswept areas and sweep the residual oil. As a result, the volumetric sweep efficiency or the oil RF was considerably increased. Hence, the miscible CO₂ tertiary flooding after waterflooding is also the most effective method to recover the light oil from the vuggy ROZ, where the porosity is widely distributed and the vugs are poorly connected.

4.4 Miscible CO₂-SWAG Injection in a Tight MPZ

4.4.1 Effective viscosities of the saline water–CO₂ mixtures

The effective viscosity of each saline water–CO₂ mixture is determined from Equation (3.1) and shown in Figure 4.10. It is found that the measured effective viscosity of the water–CO₂ mixture is increased with the water volume fraction. The increased effective viscosity of the water–CO₂ mixture indicates that low-viscosity CO₂ is viscosified by the co-injected water. In the EOR process, an increased viscosity of the displacing phase (i.e., the water–CO₂ mixture) will lead to an increased overall sweep efficiency and an increased oil RF. It is worthwhile to note that, usually, the effective

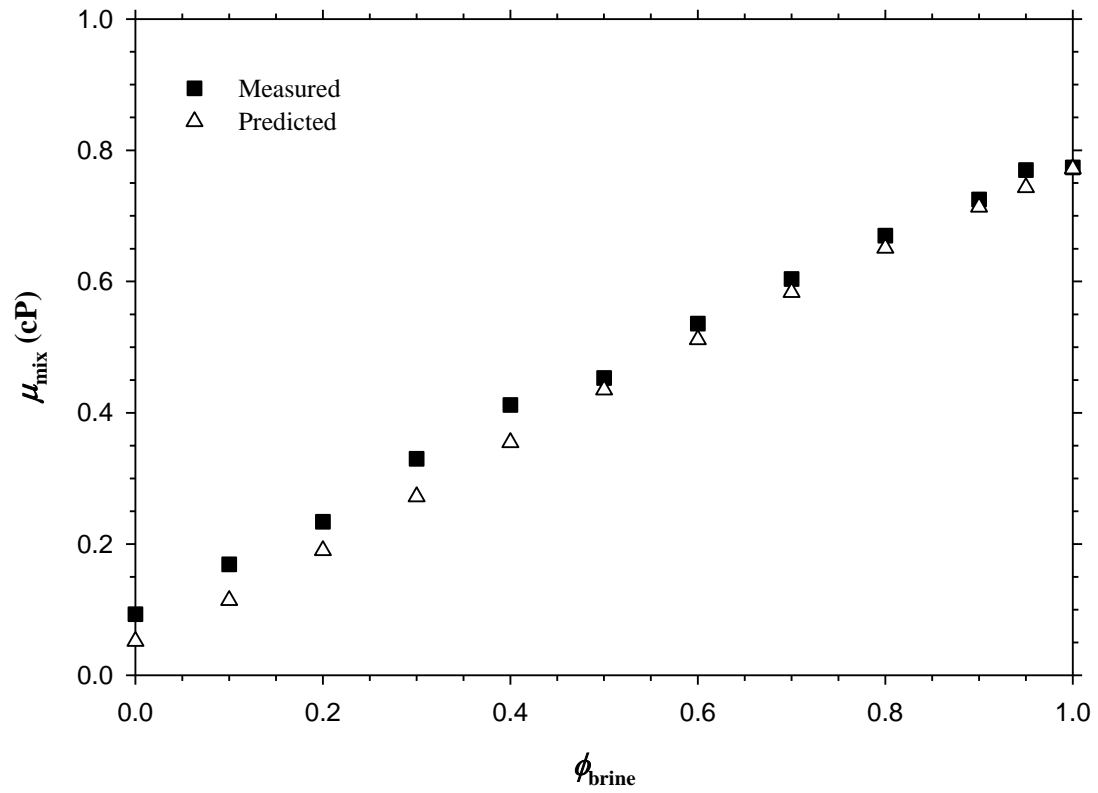


Figure 4.10 Measured and predicted effective viscosities (μ_{mix}) of the water-CO₂ mixtures at twelve increasing water volume fractions (ϕ_{brine}) at $P = 15.0$ MPa and $T_{\text{res}} = 51.1$ °C.

viscosity of a mixture of two immiscible phases (e.g., water and oil) is substantially higher than that of either phase if an emulsion is formed, such as the water-in-oil (W/O) or oil-in-water (O/W) emulsion [Arnold and Stewart, 2008]. Nevertheless, no such trend is found for the saline water–CO₂ mixtures tested in this study. As shown in Figure 4.10, the measured effective viscosities of the water–CO₂ mixtures with twelve increasing water volume fractions can be well modelled by applying the classical Arrhenius equation [Irving, 1977]:

$$\mu_{\text{mix}} = \mu_{\text{brine}}^{x_{\text{brine}}} \cdot \mu_{\text{CO}_2}^{x_{\text{CO}_2}}, \quad (4.3)$$

where μ_{mix} is the predicted effective viscosity of the water–CO₂ mixture; x_{brine} and x_{CO_2} are mole fractions of the synthetic brine and CO₂ in the water–CO₂ mixture, respectively; μ_{brine} and μ_{CO_2} are the calculated viscosities of the synthetic brine and supercritical CO₂ by using the CMG WinProp module. This fact suggests that the high-salinity synthetic brine and supercritical CO₂ mixture under the reservoir conditions has an ideal viscosity behaviour by following a simple mixing rule [Yener *et al.*, 1998; Gong and Gu, 2015b]. It is also found from Figure 4.10 that the predicted effective viscosities of the water–CO₂ mixtures at the high water volume fractions of $\phi_{\text{brine}} \geq 0.5$ were closer to the measured data. For the water–CO₂ mixtures of $\phi_{\text{brine}} < 0.5$, however, the predicted effective viscosities were always lower than the measured values. In this study, gas production was found to have large fluctuations when a water–CO₂ mixture of $\phi_{\text{brine}} < 0.5$ flew through the capillary tubing. It was speculated that this unstable flow behaviour or pattern might lead to a slight increase in the measured pressure drop or effective viscosity.

4.4.2 Three CO₂-EOR processes

In this study, three coreflood tests were conducted with three different injection schemes of miscible CO₂ secondary flooding (Test #11), waterflooding followed by miscible CO₂ tertiary flooding (Test #12), and miscible CO₂-WAG injection (Test #13) in the tight reservoir core plugs. The detailed physical properties of the composite reservoir core plugs, experimental conditions, and oil RFs of these three coreflood tests are summarized in Table 4.3. The measured oil RFs, average gas production rates, and cumulative water production data for Tests #11–13 are plotted in Figures 4.11–4.13. It is worthwhile to point out that there was no connate water production in the miscible CO₂ secondary flooding and that there was no gas production in the waterflooding.

Figure 4.11 shows that in the miscible CO₂ secondary flooding, both oil and gas were produced rapidly from the beginning. The early produced gas was mainly composed of CO₂, which was dissolved into the oil phase and co-produced with it. Then the average gas production rate reached its peak value at 0.41 PV, which is referred to as the PV of CO₂-BT. At this time, some continuous gas channels might be formed inside the composite core plugs from the inlet to outlet of the coreholder. After CO₂-BT occurred, the oil production rate was reduced gradually, while the average gas production rate was always in the high range of 24–56 cm³/min. It is also found that in the first 0.41 PV of injected CO₂, 51.56% of the OOIP was produced. In contrast, the subsequently injected 1.59 PV CO₂ recovered 31.25% of the OOIP. After CO₂-BT, the injected CO₂ tends to flow through the established gas channels. Therefore, the increased oil RF is mainly attributed to the light-HCs extraction by the supercritical CO₂ in the late oil production period [Cao and Gu, 2013b].

Table 4.3 Physical properties of the composite reservoir core plugs collected from the Tatagwa oilfield, experimental conditions, oil recovery factors of six water- and CO₂-based coreflood tests at $q_{\text{mix}} = 0.1 \text{ cm}^3/\text{min}$, $P_{\text{prod}} = 15.0 \text{ MPa}$, and $T_{\text{res}} = 51.1 \text{ }^\circ\text{C}$.

Test No.	Injection Scheme	k (mD)	ϕ (%)	S_{oi} (%)	q_{brine} (cm ³ /min)	q_{CO_2} (cm ³ /min)	Injected WGR	RF _w (%)	RF _{total} (%)	ΔP_{ave} (kPa)	M
11	CO ₂ secondary flooding	7.10	15.16	58.82	–	0.100	0:1	–	82.81	66	7.58
12	Waterflooding	4.44	15.70	57.26	0.100	–	1:0	40.94	65.67	332	1.28
	CO ₂ tertiary flooding				–	0.100	0:1	–		202	2.10
13	CO ₂ -WAG injection	0.98	16.47	45.30	0.100	0.100	1:3	–	83.02	–	–
14	CO ₂ -SWAG injection	10.08	14.40	56.04	0.025	0.075	1:3	–	96.21	998	0.46
15		5.60	15.40	50.28	0.050	0.050	1:1	–	76.36	432	0.94
16		10.06	14.33	57.28	0.075	0.025	3:1	–	85.42	714	0.63

- Notes: k : absolute permeability of three composite reservoir core plugs
 ϕ : porosity of three composite reservoir core plugs
 S_{oi} : initial oil saturation
 q_{brine} : volume injection rate of the synthetic brine under the specified reservoir conditions
 q_{CO_2} : volume injection rate of CO₂ under the specified reservoir conditions
 Injected WGR: injected water–gas ratio (WGR) in terms of the volume injection rates under the specified reservoir conditions
 RF_w: oil recovery factor (RF) of waterflooding in terms of the original oil-in-place (OOIP)
 RF_{total}: total oil RF of waterflooding and CO₂ flooding in terms of the OOIP
 ΔP_{ave} : average stable pressure drop between the inlet and outlet of the coreholder
 M : mobility ratio of the injected fluid(s) to the light crude oil

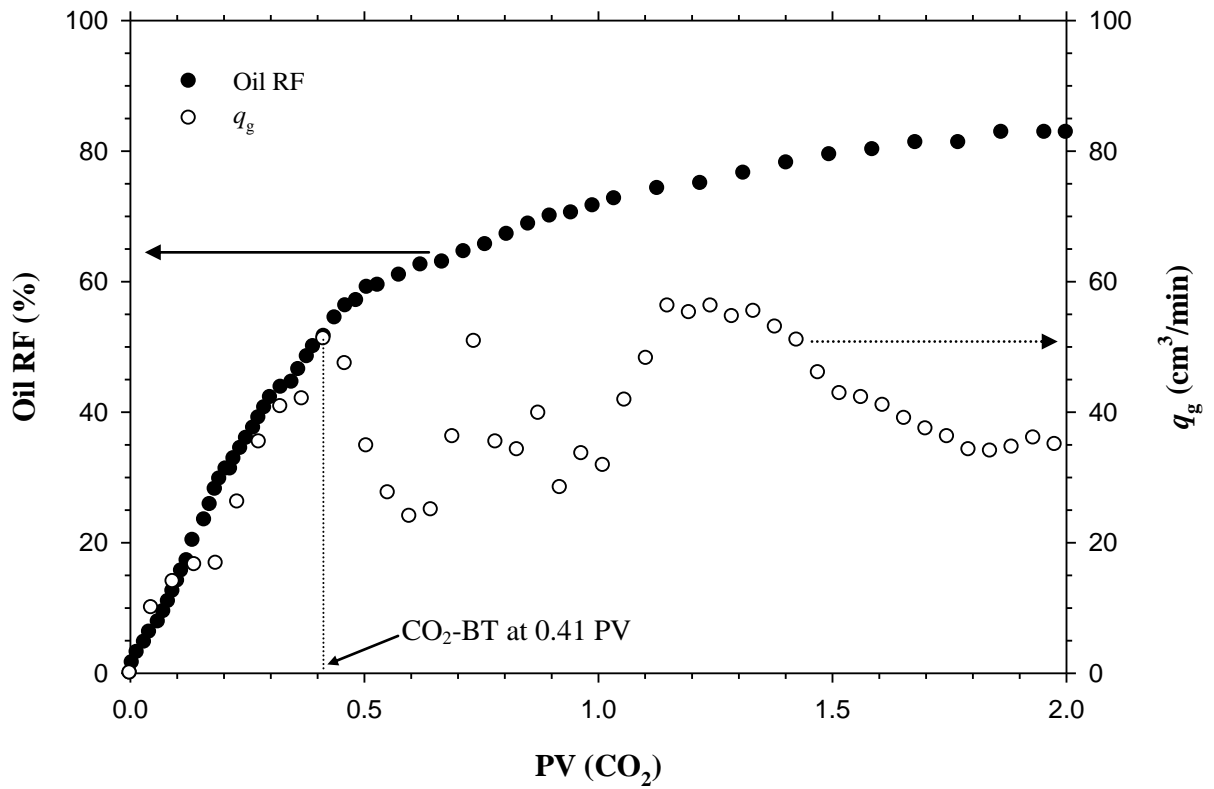


Figure 4.11 Measured oil RFs and average gas production rates (q_g) versus the PVs of injected CO₂ in Test #11 (miscible CO₂ secondary flooding).

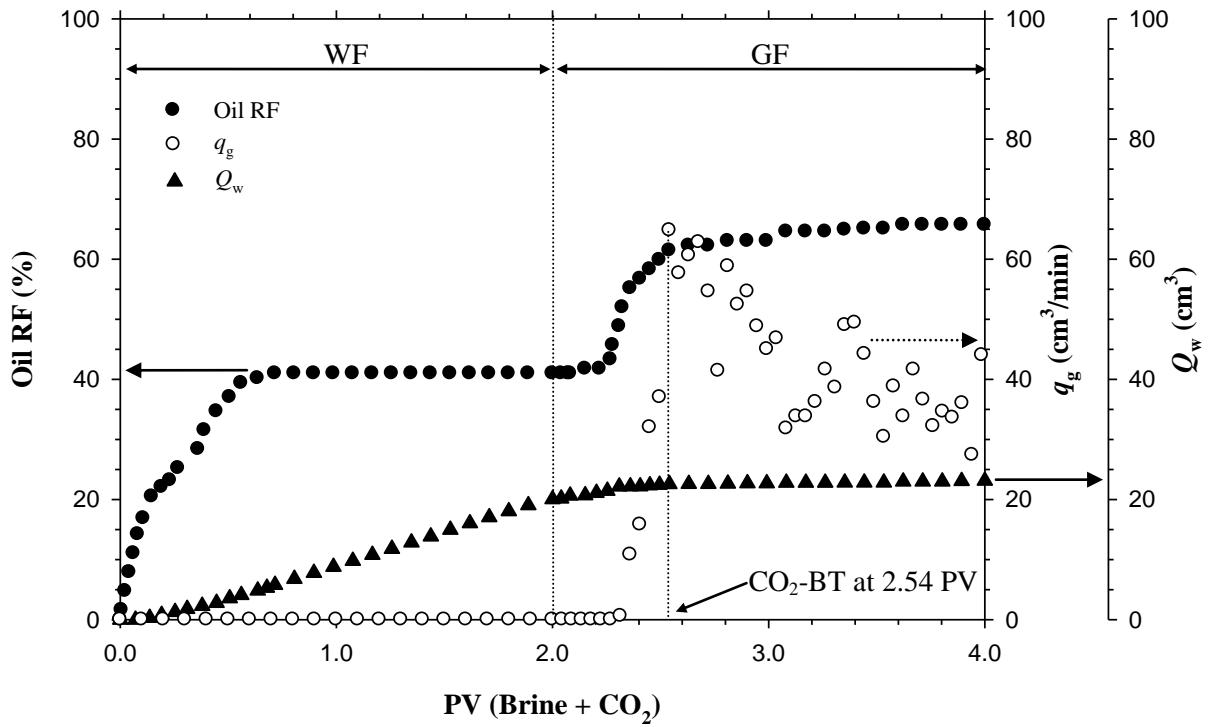


Figure 4.12 Measured oil RFs, average gas production rates (q_g), and cumulative water production data (Q_w) versus the PVs of injected brine and CO₂ in Test #12 (waterflooding followed by miscible CO₂ tertiary flooding).

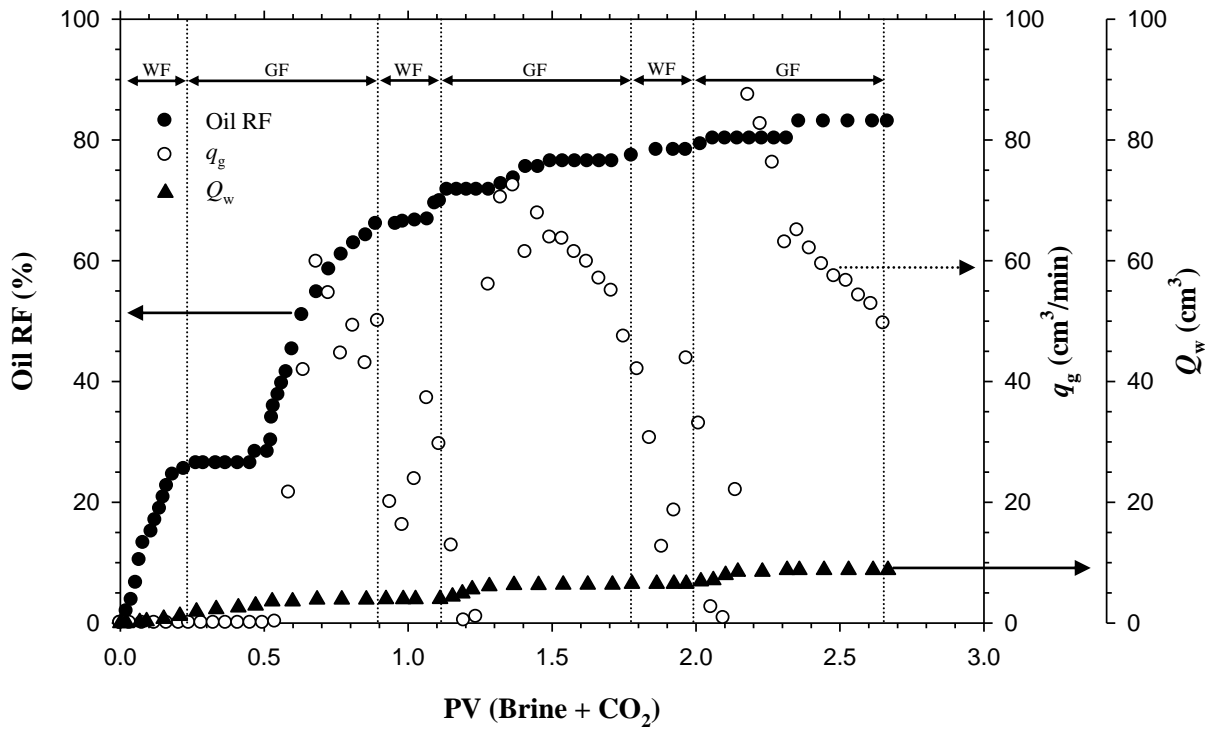


Figure 4.13 Measured oil RFs, average gas production rates (q_g), and cumulative water production data (Q_w) versus the PVs of injected brine and CO₂ in Test #13 (miscible CO₂-WAG injection with a slug size of 0.222 PV and a slug ratio of 1:3).

Figure 4.12 depicts the measured oil RFs, average gas production rates, and cumulative water production data versus the PVs of injected brine and CO₂ in the waterflooding followed by miscible CO₂ tertiary flooding (Test #12). As shown in this figure, the oil RF was increased almost linearly at the beginning of the waterflooding till 0.25 PV. In this early quick oil production period, the injected water volumetrically displaced the light crude oil inside the composite reservoir core plugs. Then the oil production rate started to decrease and the cumulative water production was increased gradually as water was co-produced with the oil. At 0.72 PV, the composite core plugs were already watered-out. Afterward, the cumulative water production increased linearly with the PV of injected water and no oil was produced till the end of waterflooding.

The subsequent miscible CO₂ tertiary flooding can be approximately divided into three different fluid production stages, based on the measured fluid production trends. At the beginning, only water was produced and there was neither oil nor gas production. The injected CO₂ displaced and produced the mobile water through the core plugs. In the second stage, CO₂-saturated oil was produced quickly with a low to moderate average gas production rate, while water production was quickly diminished as most mobile water had already been produced in the first stage. Finally, CO₂-BT occurred and the oil production rate was reduced gradually. The CO₂-BT took place at 0.54 PV of injected CO₂. In this test, some water channels might be fully developed inside the core plugs after the mature waterflooding. Hence, the subsequently injected CO₂ preferentially followed the water channels and broke through the core plugs. Besides, a large amount of water was left inside the core plugs prior to the miscible CO₂ tertiary flooding. The large amount of water blocked the residual crude oil from being contacted by the supercritical

CO₂ and thus hindered the light crude oil–CO₂ miscibility development, which is also known as the waterblocking effect [Lin and Huang, 1990]. As a result, the microscopic displacement efficiency was lowered in the miscible CO₂ tertiary flooding post the mature waterflooding, in comparison with that in the miscible CO₂ secondary flooding.

The measured oil RFs, average gas production rates, and cumulative water production data of the miscible CO₂-WAG injection (Test #13) are plotted in Figure 4.13. In this test, a total of three WAG cycles were conducted with the slug size of 0.222 PV and the slug ratio of 1:3. The WAG slug size represents the volume of the first fluid (i.e., water) injected. On the other hand, the WAG slug ratio denotes the volume ratio of the first fluid (i.e., water) to the second fluid (i.e., CO₂) in each cycle at the reservoir conditions. The oil RFs of the three WAG cycles were found to be 66.04%, 11.32%, and 5.66%, respectively. More specifically, 79.55% of the produced oil was recovered in the first WAG cycle and 60.24% of the produced oil was recovered during three CO₂-slug injection periods. In the WAG injection, the average gas production rate was always decreased substantially in each water-slug injection period. This fact shows that the injected small water slug helped to effectively control the mobility of the subsequently injected CO₂ and stabilize its displacement front. It is also found from Figure 4.13 that nevertheless, CO₂-BT occurred at 0.46 PV of injected CO₂ in the first WAG cycle. In the next two cycles, it happened sooner at 0.26 PV and 0.18 PV, respectively. These experimental data indicate that CO₂ mobility-control by the injected water slug was compromised after more WAG cycles were conducted. At a later time, some water and gas channels were developed inside the core plugs. It is worthwhile to note that waterflooding followed by miscible CO₂ tertiary flooding (Test #12) can be considered as

miscible CO₂-WAG injection of one cycle only with a large slug size of 2.0 PV and a slug ratio of 1:1. With a much reduced slug size (0.222 PV) and a smaller slug ratio (1:3), Test #13 had an oil RF of 83.02%, which was much higher than 65.67% in Test #12. Accordingly, an even higher oil RF may be achieved by applying a CO₂-EOR process with an infinitely reduced slug size, such as miscible CO₂-SWAG injection.

4.4.3 WGR effects

In this study, three miscible CO₂-SWAG injection tests with different injected WGRs of 1:3, 1:1, and 3:1 were conducted in the tight reservoir core plugs to examine the WGR effect on the oil recovery process. The detailed physical properties of the composite reservoir core plugs, experimental conditions, and oil RFs of these three coreflood tests are tabulated in Table 4.3. The measured oil RFs, average gas production rates, and cumulative water production data for Tests #14–16 are plotted in Figures 4.14a–c, respectively. As shown in these three figures, gas production was delayed or gas mobility was well controlled in each miscible CO₂-SWAG injection test. In all three tests, no apparent gas-BTs occurred and the average gas production rates were always in a range of 0–30 cm³/min, which was much lower than those in Tests #11–13. In particular, gas production in Test #15 with the injected WGR of 1:1 was delayed to total 1.40 PV, which was equivalent to 0.70 PV of injected CO₂. Gas production in Test #16 with the injected WGR of 3:1 was much delayed to total 2.04 PV or 0.51 PV of injected CO₂. In these three CO₂-SWAG injection tests, water production was also delayed to total 1.54 PV, 0.50 PV, and 0.69 PV, respectively. Overall, the mobilities of both CO₂ and water phases were substantially reduced in the miscible CO₂-SWAG injection.

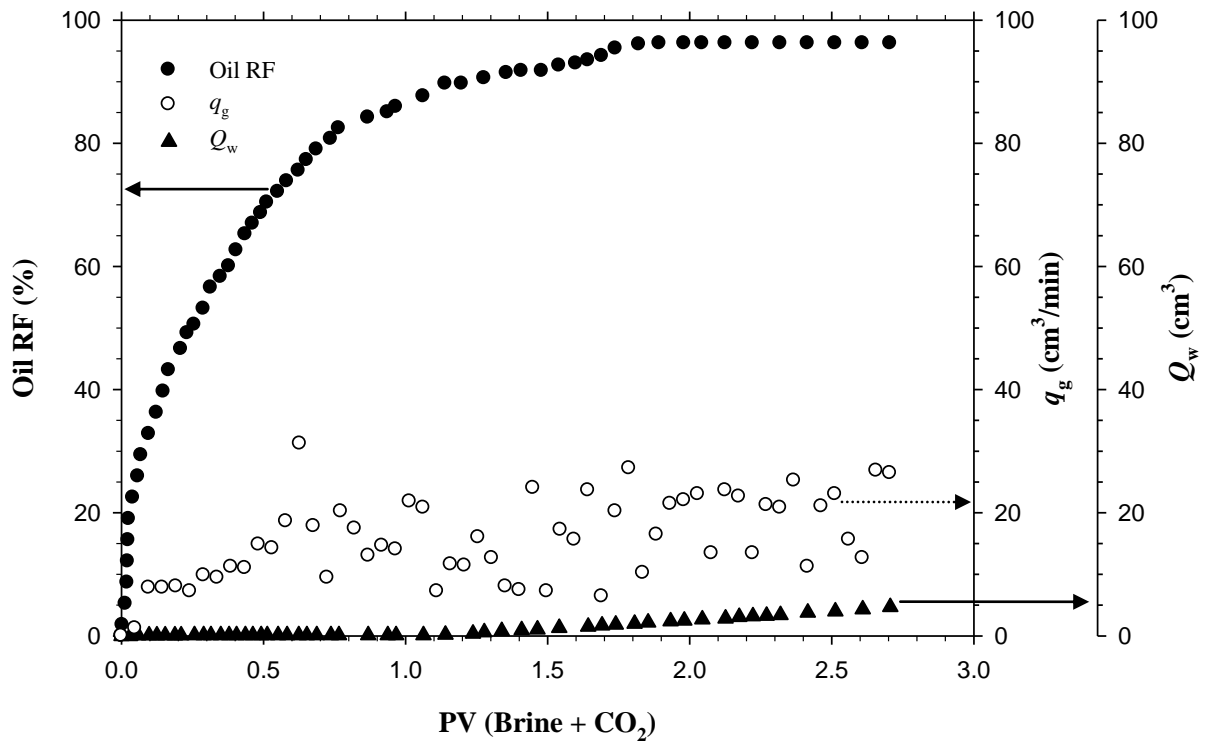


Figure 4.14 (a) Measured oil RFs, average gas production rates (q_g), and cumulative water production data (Q_w) versus the PVs of injected brine and CO₂ in Test #14 (miscible CO₂-SWAG injection with the injected WGR of 1:3 in volume).

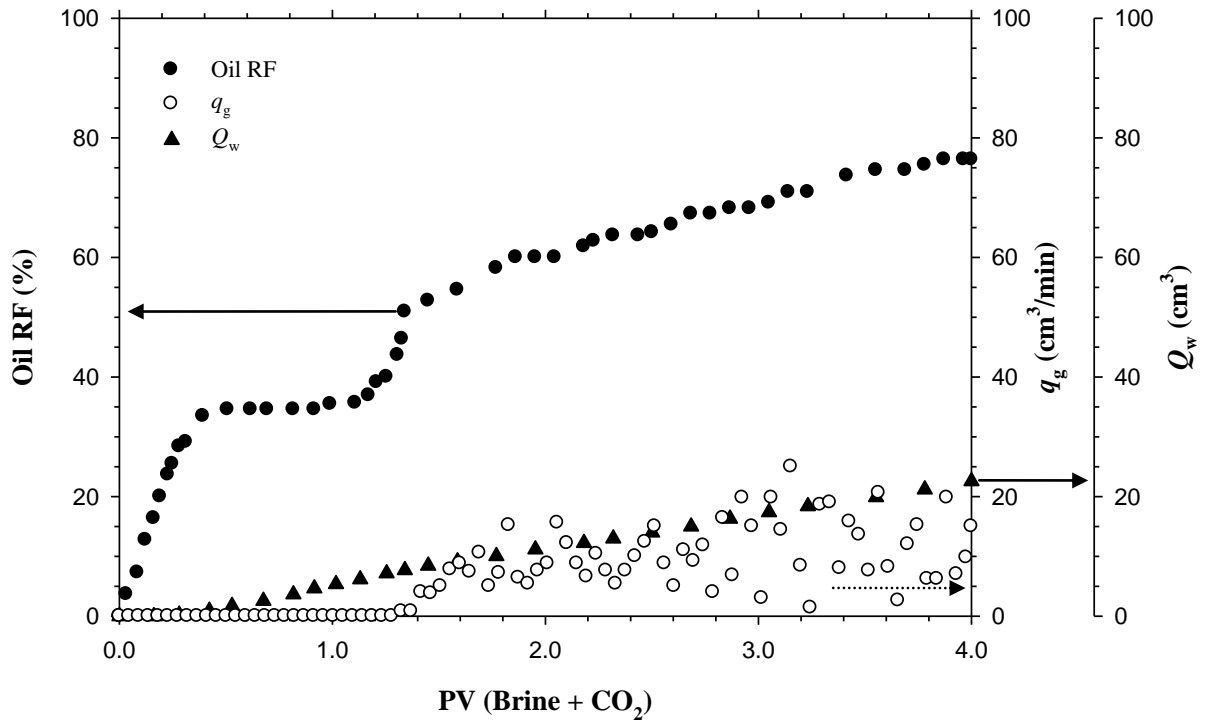


Figure 4.14 (b) Measured oil RFs, average gas production rates (q_g), and cumulative water production data (Q_w) versus the PVs of injected brine and CO₂ in Test #15 (miscible CO₂-SWAG injection with the injected WGR of 1:1 in volume).

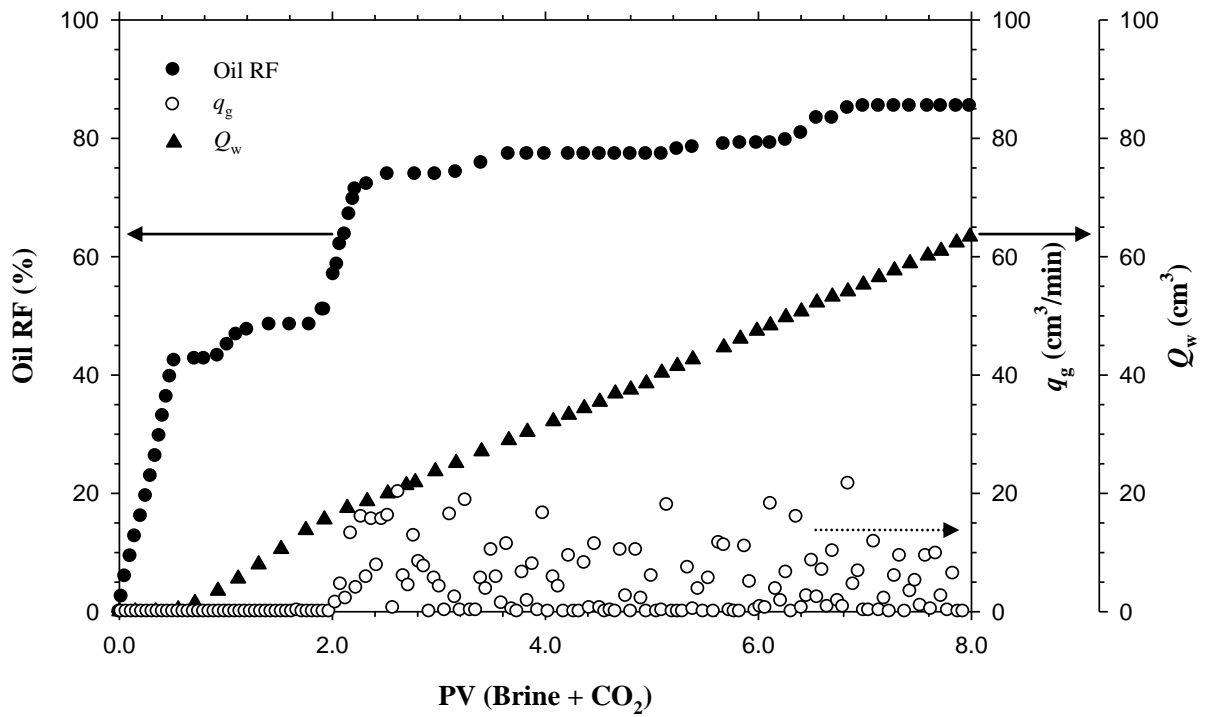


Figure 4.14 (c) Measured oil RFs, average gas production rates (q_g), and cumulative water production data (Q_w) versus the PVs of injected brine and CO₂ in Test #16 (miscible CO₂-SWAG injection with the injected WGR of 3:1 in volume).

In general, the miscible CO₂-SWAG injection combines both waterflooding and CO₂ injection. Inevitably, the oil recovery trend of CO₂-SWAG injection is similar to that of waterflooding or CO₂ flooding to some extent. As shown in Figure 4.14a, the entire oil recovery process of CO₂-SWAG injection with a relatively low injected WGR of 1:3 in Test #14 was similar to the miscible CO₂ secondary flooding (Test #11). The quick oil production together with low gas production started almost immediately from the beginning. The oil production rate was reduced gradually and the final oil RF reached a maximum value. No apparent CO₂-BT was found, whereas the water production was much delayed and only a small amount of water was produced at the end. In this case, the CO₂ displacement front moved faster than the water displacement front in the tight reservoir core plugs with a miscible CO₂ bank being formed ahead of the water-CO₂ mixture.

In Tests #15 and #16 with relatively higher injected WGRs as shown in Figures 4.14b and c, the entire oil recovery processes were more similar to the waterflooding followed by miscible CO₂ tertiary flooding (Test #12) and can be approximately divided into four fluid production stages. First, there was neither water nor gas production in the first oil production stage. In the second water production stage, oil production was quickly diminished and no gas was produced yet. In these two stages, the injected CO₂ was likely dissolved into the light crude oil. Then CO₂-diluted light crude oil was produced rapidly in the third quick oil production stage with a much decreased water production rate and a fluctuated gas production rate. In the final production stage, the oil production rate was reduced gradually and water was produced steadily, while the gas production rate continued to fluctuate. Most oil was produced in the first linear and third quick oil

production stages. In these two CO₂-SWAG tests, the water displacement front was ahead of the CO₂ displacement front and formed a water bank. Consequently, the light crude oil inside the tight core plugs is easily trapped or blocked by the injected water.

4.4.4 Mobilities of water, CO₂, and water–CO₂ mixtures

Figure 4.15 shows the measured pressure drops between the inlet and outlet of the coreholder during the flooding processes in Tests #11–16. The miscible CO₂-WAG injection (Test #13) had the highest pressure drops due to the lowest permeability of the composite reservoir core plugs used in this test. Its pressure drop was increased substantially in each water-slug injection period because the high-salinity brine is much more viscous than the supercritical CO₂. In contrast, the other three CO₂-EOR schemes (Tests #11, #12, and #14–16) had much more stable pressure drops. It is also seen from Figure 4.15 that the measured pressure drop became stable near the end of each of these five tests when a steady-state flow was achieved.

In the literature, Heller *et al.* [1985] assumed that the steady CO₂-foam flow in porous media was uniform. They defined the CO₂-foam mobility as the ratio of the superficial flow velocity to the steady-state pressure gradient. More recently, Shetty *et al.* [2014] made a similar assumption for the CO₂-SWAG injection in order to calculate the mobility of the injected water–CO₂ mixture. In this study, as a first approximation, the water–CO₂ mixture was assumed to be a pseudo single-phase fluid in each miscible CO₂-SWAG injection test. Hence, an apparent mobility of the injected fluid(s) in each test was determined as:

$$\lambda_f = \frac{k_f'}{\mu_f} = \frac{q_{\text{mix}}/A}{\Delta P_{\text{ave}}/L}, \quad (4.4)$$

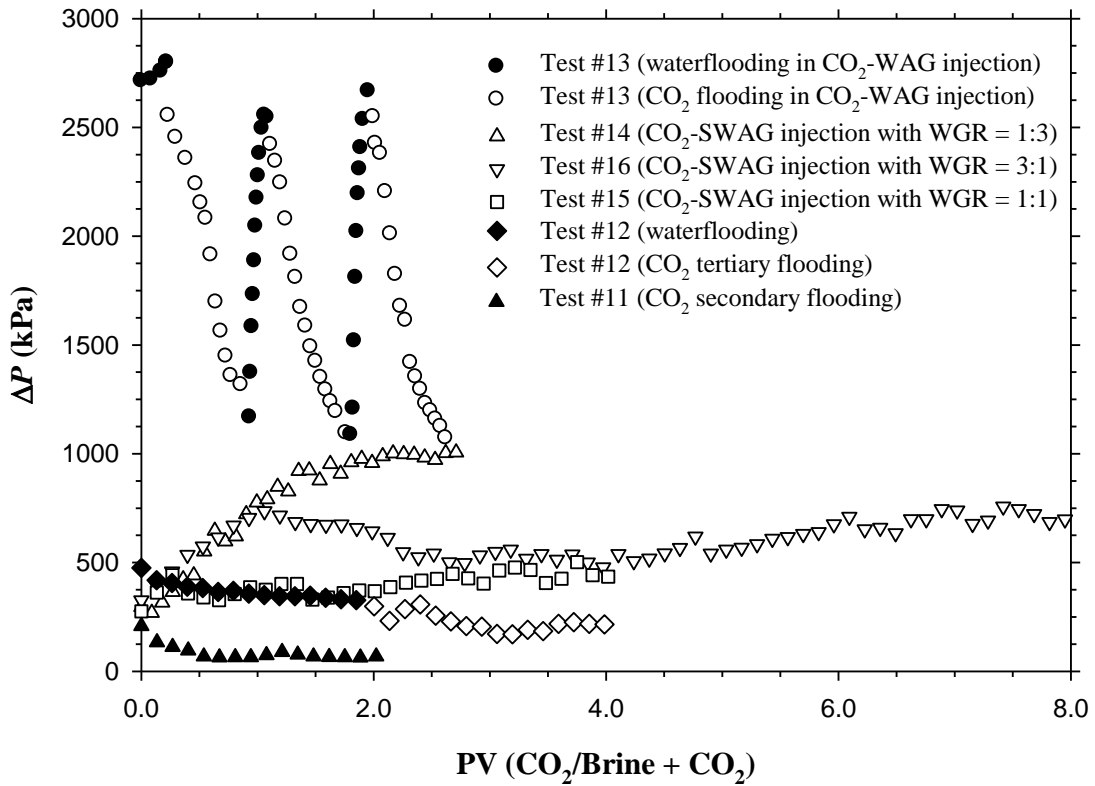


Figure 4.15 Measured pressure drops (ΔP) between the inlet and outlet of the coreholder versus the PVs of injected CO₂ in Test #11 (miscible CO₂ secondary flooding) or injected brine + CO₂ in Test #12 (waterflooding followed by miscible CO₂ tertiary flooding), Test #13 (miscible CO₂-WAG injection), and Tests #14–16 (miscible CO₂-SWAG injection).

where λ_f is the apparent mobility of the injected fluid(s); k_f' is the end-point effective permeability to the injected fluid(s); μ_f is the effective viscosity of the injected fluid(s) under the test conditions; q_{mix} is the total volume injection rate; A and L are the cross-sectional area and length of the composite reservoir core plugs; ΔP_{ave} is an average steady-state pressure drop between the inlet and outlet of the coreholder near the end of each test, which is listed in Table 4.3. In order to eliminate the influence of a different absolute permeability of the composite core plugs used in each test, the mobility ratio of the apparent mobility of the injected fluid(s) to the mobility of the light crude oil is defined:

$$M = \frac{\lambda_f}{\lambda_o}, \quad (4.5)$$

where M is the mobility ratio of the injected fluid(s) to the light crude oil; and λ_o is the mobility of the light crude oil, which was measured and determined from Equation (3.2) prior to each coreflood test.

Table 4.3 and Figure 4.16 summarize the mobility ratios of miscible CO₂ to oil in Test #11 (miscible CO₂ secondary flooding) and Test #12 (miscible CO₂ tertiary flooding), water–CO₂ mixtures to oil in Tests #14–16 (miscible CO₂-SWAG injection tests with different injected WGRs), and water to oil in Test #12 (waterflooding). It is found that the miscible CO₂ secondary flooding had the highest mobility ratio of $M = 7.58$ between the injected supercritical CO₂ and oil in the tight reservoir core plugs under the test conditions due to an extremely low CO₂ viscosity, as shown in Figure 4.10. This high mobility ratio can cause the instability of the displacement front to induce viscous

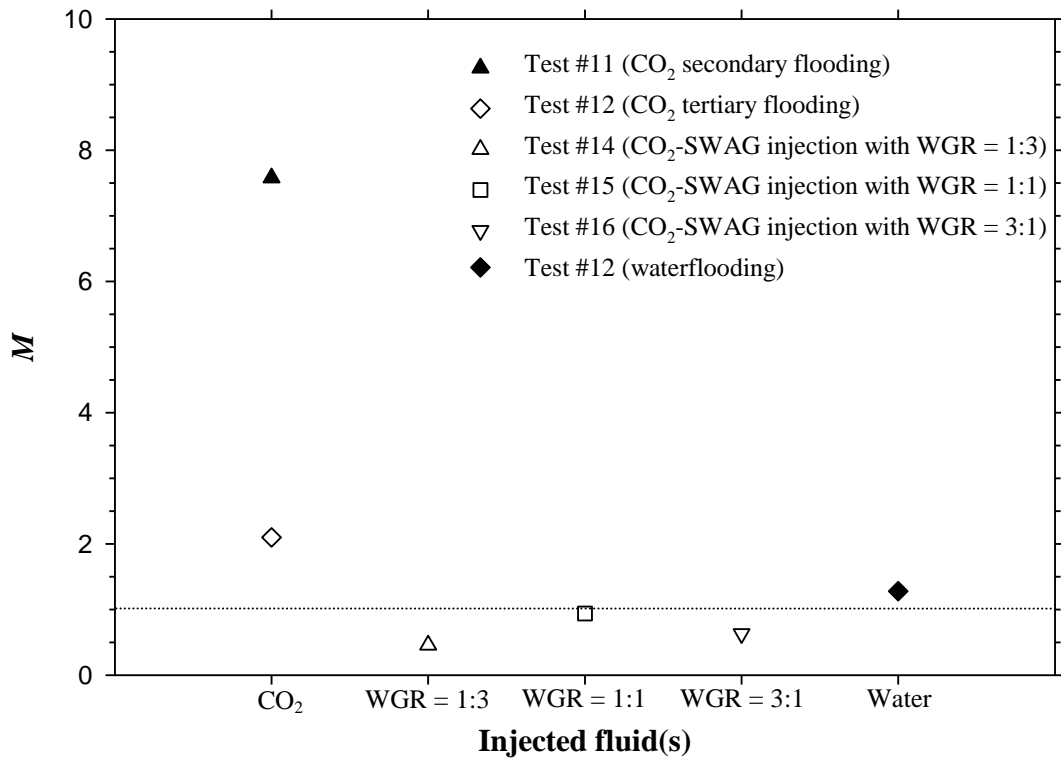


Figure 4.16 Mobility ratios (M) of injected CO₂ to oil in Test #11 (miscible CO₂ secondary flooding) and Test #12 (miscible CO₂ tertiary flooding); injected water–CO₂ mixtures to oil in Test #14 (miscible CO₂-SWAG injection with the injected WGR = 1:3), Test #15 (miscible CO₂-SWAG injection with the injected WGR = 1:1), and Test #16 (miscible CO₂-SWAG injection with the injected WGR = 3:1); and injected water to oil in Test #12 (waterflooding).

fingering or an early CO₂-BT. After the mature waterflooding in Test #12, nevertheless, the mobility of CO₂ was reduced in the miscible CO₂ tertiary flooding, which was due to a trapped water phase after the waterflooding and a possible relative permeability hysteresis [Fatemi and Sohrabi, 2013]. In comparison with the mobility of CO₂, the mobility of much viscous water was considerably reduced in the tight core plugs. Three CO₂-SWAG injection tests had the lowest and most favourable mobility ratios ($M < 1$), especially in Test #14 with the injected WGR of 1:3 and Test #16 with the injected WGR of 3:1, though the effective viscosities of the three water–CO₂ mixtures were lower than the water viscosity. In this case, a much reduced effective permeability of the multi-phase fluid flow resulted in the lowest mobility of each water–CO₂ mixture. Thus a stable and uniform displacement front was formed in the miscible CO₂-SWAG injection with a favourable mobility ratio between the displacing fluids (i.e., the water–CO₂ mixture) and the displaced fluid (i.e., the light crude oil).

4.4.5 Oil RFs

The total oil RFs of the miscible CO₂ secondary flooding, waterflooding followed by miscible CO₂ tertiary flooding, miscible CO₂-WAG injection, and three miscible CO₂-SWAG injection tests are listed in Table 4.3. These oil RFs in different oil recovery stages of each test are also plotted and compared in Figure 4.17. It is found from Table 4.3 and Figure 4.17 that waterflooding in Test #12 had an oil RF of 40.94%, which was much lower than 82.81% of miscible CO₂ secondary flooding (Test #11). Waterflooding has a low microscopic displacement efficiency due to a high IFT between the injected water and crude oil phases. Furthermore, at the same amount of 2.0 PV of injected CO₂ or CO₂ consumption, the miscible CO₂ tertiary flooding after the mature waterflooding in

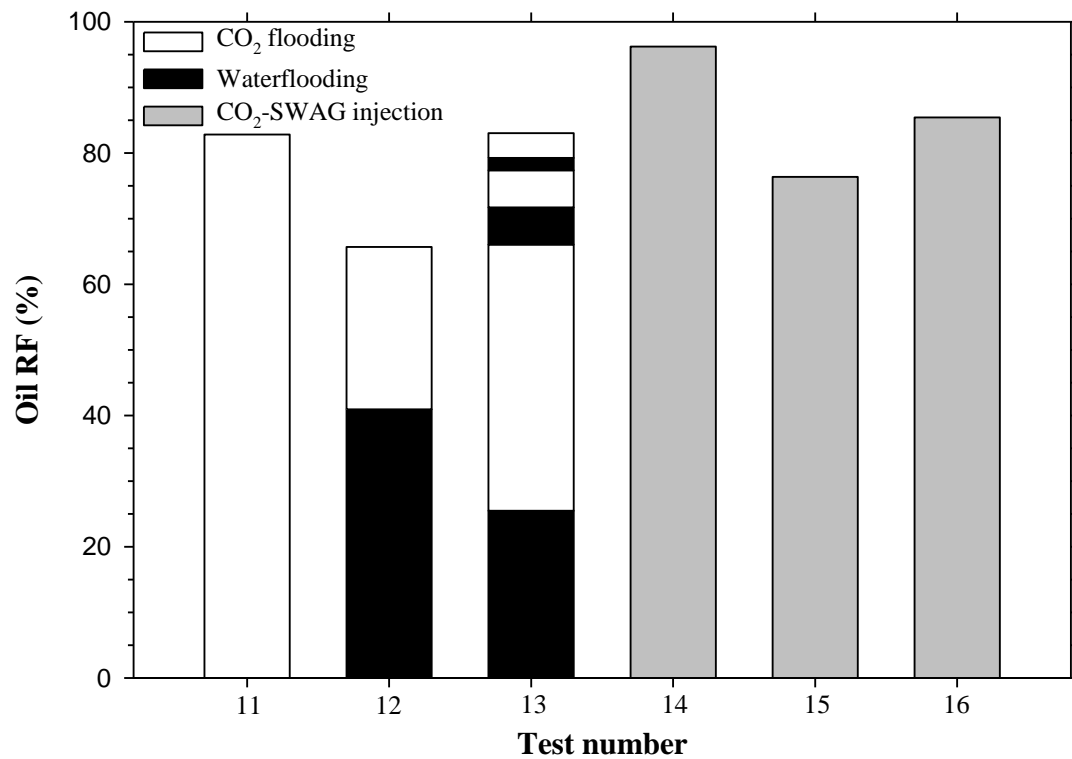


Figure 4.17 Comparison of the measured oil RFs in six coreflood tests, each of which used the same amount of 2.0 PV of injected CO₂.

Test #12 had the lowest total oil RF among the six tests. The oil RF was increased in the miscible CO₂-WAG injection (Test #13) but was only marginally higher than that of the miscible CO₂ secondary flooding. In consideration of its more complicated field operations and the unstable pressure drop (Figure 4.15), the miscible CO₂-WAG injection with the slug size of 0.222 PV and slug ratio of 1:3 is considered to be less attractive than the miscible CO₂ secondary flooding in the tight Bakken formation.

On the other hand, miscible CO₂-SWAG injection with the injected WGR of 1:3 (Test #14) had the highest oil RF and oil production rate (Figure 4.14a). The lowest mobility ratio led to the most uniform displacement front (i.e., the highest volumetric sweep efficiency) in this test. In Tests #15 and #16 with higher injected WGRs of 1:1 and 3:1, however, both the oil RF and the oil production rate (Figures 4.14b and c) were lower. The oil RF of Test #15 was even lower than that of the miscible CO₂ secondary flooding (Test #11). In these two tests, the water bank formed ahead of the CO₂ displacement front caused a severe waterblocking effect. In order to contact and possibly recover the residual oil, CO₂ had to slowly diffuse through the water-barrier phase and miscibly displace the oil phase. This is also a major reason why the oil RF of Test #16 (WGR = 3:1) with the longest injection period was only 9.06% of the OOIP higher than that of Test #15 (WGR = 1:1). At the same CO₂ consumption of 2.0 PV, miscible CO₂-SWAG injection in Test #14 with the injected WGR of 1:3 had the highest oil RF and oil production rate with well-controlled gas production and low water consumption. It is a substantially weakened waterblocking effect and a well-controlled CO₂ mobility in this test that jointly led to the optimum miscible CO₂-SWAG injection [Gong and Gu, 2015b].

CHAPTER 5 CONCLUSIONS AND RECOMMENDATIONS

5.1 Conclusions

This study experimentally analyzed and differentiated different oil recovery processes of water- and CO₂-based enhanced oil recovery (EOR) methods in a tight main pay zone (MPZ) and in a vuggy residual oil zone (ROZ). It further examined the feasibility of conducting miscible CO₂ simultaneous water-and-gas (CO₂-SWAG) injection in a tight MPZ. The following major conclusions can be drawn from this study:

- 1) The minimum miscibility pressure (MMP) of the Steelman light crude oil–CO₂ system in the multi-contact miscibility (MCM) development was measured to be 10.8 MPa and its first-contact miscibility (FCM) pressure was found to be 23.6 MPa at the reservoir temperature of $T_{\text{res}} = 51.1$ °C, respectively;
- 2) At a low equilibrium pressure and the reservoir temperature, the initial oil swelling and the subsequent slow light-hydrocarbons (HCs) extraction by CO₂ were observed. At the MMP and reservoir temperature, there was an initial and quick light-HCs extraction by the supercritical CO₂;
- 3) The production pressure had different effects on the CO₂ flooding process in the tight MPZ and in the vuggy ROZ. For the tight MPZ, the final oil recovery factor (RF) was increased almost linearly with the production pressure in the range of 2.0–14.0 MPa. For the vuggy ROZ, however, there was a sudden slope change at the MMP in the oil RF versus production pressure curve;
- 4) For miscible CO₂ secondary flooding in the carbonate reservoir core plugs with different petrographic properties, it was found that a higher final oil RF and a delayed CO₂ breakthrough (BT) were achieved in the tight core plugs with a lower

- permeability. However, miscible CO₂ secondary flooding was ineffective with a low final oil RF and the oil production was almost diminished after the initial oil production stage in the vuggy core plugs with high-permeability vugs and micro-fractures;
- 5) The oil recovery processes of miscible CO₂ tertiary flooding after waterflooding in the tight MPZ and vuggy ROZ were similar. They had three fluid production stages, namely the first water production stage, the second oil production stage, and the third gas production stage. In comparison with waterflooding and miscible CO₂ secondary flooding, miscible CO₂ tertiary flooding after waterflooding was found to be the optimum oil recovery method in both oil zones, which was attributed to an effectively controlled CO₂ mobility by pre-injected water;
 - 6) The measured effective viscosity of the high-salinity water and supercritical CO₂ mixture was increased with the water volume fraction under the reservoir conditions of $P = 15.0$ MPa and $T_{\text{res}} = 51.1$ °C. The saline water–CO₂ mixture demonstrates ideal viscosity behaviour and its measured effective viscosity can be well modelled by using the Arrhenius equation;
 - 7) With the same CO₂ consumption of 2.0 PV, the miscible CO₂-SWAG injection with a injected water–gas ratios (WGRs) of 1:3 gave the best performance in the tight core plugs with the highest oil production rate and oil RF, well-controlled gas production, and low water consumption, in comparison with miscible CO₂ secondary flooding, miscible CO₂ tertiary flooding after waterflooding, and miscible CO₂-WAG injection;

- 8) In three miscible CO₂-SWAG injection tests with different injected WGRs of 1:3, 1:1, and 3:1 in volume under the actual reservoir conditions, water productions were substantially delayed, in comparison with that of waterflooding;
- 9) In three miscible CO₂-SWAG injection tests with the injected WGRs of 1:3, 1:1, and 3:1, no apparent CO₂-BT occurred and the average gas production rates were much lower than those of miscible CO₂ secondary flooding, miscible CO₂ tertiary flooding after waterflooding, and miscible CO₂-WAG injection. These two facts indicate that CO₂ mobility was well controlled by the co-injected water phase;
- 10) The entire oil recovery process of miscible CO₂-SWAG injection with a relatively low WGR of 1:3 was very similar to that of the miscible CO₂ secondary flooding. In this case, the CO₂ displacement front moved faster than the water displacement front in the tight reservoir core plugs and a miscible CO₂ bank might be formed ahead of the water-CO₂ mixture. On the other hand, in the miscible CO₂-SWAG injection tests with relatively high WGRs of 1:1 and 3:1, the oil recovery processes were more similar to that of the waterflooding followed by miscible CO₂ tertiary flooding. In this case, the water displacement front was ahead of the CO₂ displacement front and a water bank might be formed, which caused the waterblocking effect;
- 11) Three miscible CO₂-SWAG injections with the injected WGRs of 1:3, 1:1, and 3:1 had the lowest and most favourable mobility ratios of $M < 1$ in the tight reservoir core plugs, in comparison with CO₂ flooding or waterflooding alone. Therefore, it was a substantially weakened waterblocking effect and a well-controlled CO₂ mobility that jointly resulted in the optimum CO₂-SWAG injection with the injected WGR of 1:3 in the tight Bakken formation; and

- 12) A desired injected WGR for a miscible CO₂-SWAG injection is found if a miscible CO₂ bank is formed ahead of the water-CO₂ mixture and enough water is injected to control the CO₂ mobility in the water-CO₂ mixture.

5.2 Recommendations

On the basis of this thesis study, the following recommendations are made for future studies:

- A series of miscible CO₂ soaking tests can be conducted to recover the residual oil from the vuggy core plugs and compared with CO₂ secondary and tertiary flooding processes in this study. The oil recovery process will be mainly controlled by CO₂ diffusion process if CO₂ soaking is applied. Several related factors, such as soaking pressure and time, can be optimized;
- Comprehensive numerical modeling work can be undertaken by using the CMG GEM module to simulate the CO₂ flooding process in the upper tight MPZ and the lower ROZ of a carbonate reservoir simultaneously. It is of practical importance to optimize several factors, such as well patterns and CO₂ injection locations, and obtain an optimum total oil RF from both zones together;
- Near-miscible or even immiscible CO₂-SWAG injection tests can be further carried out and compared with the miscible CO₂-SWAG injection tests in this study to investigate pressure effects on the co-injection process and the final oil RF. Besides, chemically modified brine phases (e.g., surfactant solutions) can be tested to co-inject with CO₂, aiming to generate foam in the flooding process. Injectivity issue and oil recovery process of this modified CO₂-SWAG injection can be explored as well;

- A high-pressure visualization model can be built to visualize the water and CO₂ co-injection process. The fluid flow behaviour, sweep efficiency, oil-swelling and waterblocking effects can be visualized and analyzed; and
- Based on the pressure drops and fluid production data of the CO₂-SWAG injection tests in this study, the effective or relative permeabilities of water and CO₂ during these flooding processes can be further determined theoretically or by using some commercial simulators. The WGR effects on CO₂ mobility and reservoir fluid flow behaviour can be further analyzed in a quantitative manner.

REFERENCES

- Akbar, M., Vissapragada, B., Alghamdi, A.H., Allen, D., Herron, M., Carnegie, A., Dutta, D., Olesen J.R., Chourasiya, R.D., Logan, D., Stief, D., Netherwood, R., Russell, S.D., Saxena, K. A Snapshot of Carbonate Reservoir Evaluation. *Oilfield Review*, 12(4), 20–21, 2000.
- Aleidan, A.A., Mamora, D.D. SWACO₂ and WACO₂ Efficiency Improvement in Carbonate Cores by Lowering Water Salinity. Paper SPE 137548, Canadian Unconventional Resources and International Petroleum Conference. Calgary, Alberta, October 19–21, 2010.
- Algharaib, M.K., Gharbi, R.B., Malallah, A., Al-Ghanim, W. Parametric Investigations of a Modified SWAG Injection Technique. Paper SPE 105071, SPE Middle East Oil and Gas Show and Conference, Kingdom of Bahrain, March 11–14, 2007.
- Arnold, K., Stewart, M. *Surface Production Operations, Volume 1: Design of Oil Handling Systems and Facilities*. Gulf Professional Publishing: Houston, TX, 2008; pp 95–97.
- Aroonsri, A., Worthen, A.J., Hariz, T., Johnston, K.P., Huh, C., Bryant, S.L. Conditions for Generating Nanoparticle-Stabilized CO₂ Foams in Fracture and Matrix Flow. Paper SPE 166319, SPE Annual Technical Conference and Exhibition, New Orleans, LA, September 30–October 2, 2013.
- Asghari, K., Torabi, F. Laboratory Experimental Results of Huff-and-Puff CO₂ Flooding in a Fractured Core System. Paper SPE 110577, SPE Annual Technical Conference and Exhibition, Anaheim, CA, November 11–14, 2007.

- Attanucci, V., Aslesen, K.S., Hejl, K.A., Wright, C.A. WAG Process Optimization in the Rangely CO₂ Miscible Flood. Paper SPE 26622, SPE Annual Technical Conference and Exhibition, Houston, TX, October 3–6, 1993.
- Awan, A.R., Teigland, R., Kleppe, J. A Survey of North Sea Enhanced-Oil-Recovery Projects Initiated During the Years 1975 to 2005. *SPE Res. Eval. & Eng.*, 11(3), 497–512, 2008.
- Bargas, C.L., Montgomery, H.D., Sharp, D.H., Vosika J.L. Immiscible CO₂ Process for the Salt Creek Field. *SPE Res. Eng.*, 7(4), 397–402, 1992.
- Beliveau, D., Payne, D.A. Analysis of a Tertiary CO₂ Flood Pilot in a Naturally Fractured Reservoir. Paper SPE 22947, SPE Annual Technical Conference and Exhibition, Dallas, TX, October 6–9, 1991.
- Bellavance, J.F.R. Dollarhide Devonian CO₂ Flood: Project Performance Review 10 Years Later. Paper SPE 35190, Permian Basin Oil and Gas Recovery Conference, Midland, TX, March 27–29, 1996.
- Brinkman, F.P., Kane, T.V., McCullough, R.R., Miertschin, J.W. Use of Full-Field Simulation to Design a Miscible CO₂ Flood. *SPE Res. Eval. Eng.*, 2(3), 230–237, 1999.
- Cao, M., Gu, Y. Temperature Effects on the Phase Behaviour, Mutual Interactions and Oil Recovery of a Light Crude Oil–CO₂ System. *Fluid Phase Equilibria*, 356(1), 78–89, 2013a.
- Cao, M., Gu, Y. Physicochemical Characterization of Produced Oils and Gases in Immiscible and Miscible CO₂ Flooding Processes. *Energy & Fuels*, 27(1), 440–453, 2013b.

- Caudle, B.H., Dyes, A.B. Improving Miscible Displacement by Gas–Water Injection. *AIME*, 213(1), 281–284, 1958.
- Chen, S., Li, H., Yang, D., Tontiwachwuthikul, P. Optimal Parametric Design for Water-Alternating-Gas (WAG) Process in a CO₂-Miscible Flooding Reservoir. *J. Can. Petrol. Technol.*, 49(10), 75–82, 2010.
- Cheng, P., Li, D., Boruvka, L., Rotenberg, Y., Neumann, A.W. Automation of Axisymmetric Drop Shape Analysis for Measurements of Interfacial Tensions and Contact Angles. *Colloids. Surf.*, 43(2), 151–67, 1990.
- Choquette, P.W., Pray, L.C. Geologic Nomenclature and Classification of Porosity in Sedimentary Carbonates. *AAPG Bull.*, 54(2), 207–250, 1970.
- Christensen, J.R., Stenby, E.H., Skauge, A. Review of WAG Field Experience. *SPE Res. Eval. Eng.*, 4(2), 97–106, 2001.
- Cosse, R. *Basics of Reservoir Engineering: Oil and Gas Field Development Techniques*. Paris: Editions Technip, 1993.
- Crameik, T.D., Plassey, J.A. Carbon Dioxide Injection Project SACROC Unit, Scurry County, TX. Paper API 72-D00, Annual Meeting Papers, Division of Production, Houston, TX, March 6–8, 1972,
- Do, H.D., Pinczewski, W.V. Diffusion-Controlled Swelling of Reservoir Oil by Indirect Contact with Injection Gas. *Chem. Eng. Sci.*, 48(18), 3243–3252, 1993.
- Dong, M., Huang, S., Srivastava, R. A Laboratory Study on Near-Miscible CO₂ Injection in Steelman Reservoir. *J. Can. Petrol. Technol.*, 40(2), 53–61, 2001.

- Dong, M., Huang, S., Srivastava, R. Coreflood Studies of Tertiary CO₂ Flood in Naturally Fractured Midale Formation in Southeast Saskatchewan. *J. Can. Petrol. Technol.*, 41(2), 41–46, 2002.
- Dou, Q., Sun, Y., Sullivan, C. Rock-Physics-Based Carbonate Pore Type Characterization and Reservoir Permeability Heterogeneity Evaluation, Upper San Andres Reservoir, Permian Basin, West Texas. *J. Appl. Geophys.*, 74(1), 8–18, 2011.
- Espie, T. A New Dawn for CO₂ EOR. Paper IPTC 10935, International Petroleum Technology Conference. Doha, Qatar, November 21–23, 2005.
- Espinoza, D.A., Caldelas, F.M., Johnston, K.P., Bryant, S.L., Huh, C. Nanoparticle-Stabilized Supercritical CO₂ Foams for Potential Mobility Control Applications. Paper SPE 129925, SPE Improved Oil Recovery Symposium, Tulsa, OK, April 24–28, 2010.
- Fatemi, S. M., Sohrabi, M. Recovery Mechanisms and Relative Permeability for Gas/Oil Systems at Near-Miscible Conditions: Effects of Immobile Water Saturation, Wettability, Hysteresis, and Permeability. *Energy Fuels*, 27(5), 2376–2389, 2013.
- Gong, Y., Gu, Y. Water and CO₂ Flooding in Tight Main Pay Zone and Vuggy Residual Oil Zone of a Carbonate Reservoir, *Ind. Eng. Chem. Res.*, MS. ID: IE-2015-008104, submitted on February 28, 2015a.
- Gong, Y., Gu, Y. Miscible CO₂ Simultaneous Water-and-Gas (CO₂-SWAG) Injection in the Bakken Formation, *in preparation*, 2015b.
- Gozalpour, F., Ren, S.R., Tohidi, B. CO₂ EOR and Storage in Oil Reservoir. *Oil Gas Sci. Technol.*, 60(3), 537–546, 2005.

- Grattoni, C.A., Dawe, R.A. Gas and Oil Production from Waterflood Residual Oil: Effects of Wettability and Oil Spreading Characteristics. *J. Petrol. Sci. Eng.*, 39(3), 297–308, 2003.
- Green, D.W., Willhite, G.P. *Enhanced Oil Recovery*. Textbook Series, Vol. 6, SPE Richardson, TX, 1998.
- Grigg, R.B., Gregory, M.D., Purkale, J.D. Effect of Pressure on Improved Oilflood Recovery from Tertiary Gas Injection. *SPE Res. Eng.*, 12(3), 179–187, 1997.
- Grogan, A.T., Pinczewski, W.V. The Role of Molecular Diffusion Processes in Tertiary CO₂ Flooding. *J. Petrol. Technol.*, 39(5), 591–602, 1987.
- Hamouda, A.A., Alipour Tabrizy, V. The Effect of Light Gas on Miscible CO₂ Flooding to Enhance Oil Recovery from Sandstone and Chalk Reservoirs. *J. Petrol. Sci. Eng.*, 108(1), 259–266, 2013.
- Han, L., Gu, Y. Optimization of Miscible CO₂-WAG Injection in the Bakken Formation. *Energy & Fuels*, *in press*, 2014.
- Heidari, P., Alizadeh, N., Kharrat, R., Ghazanfari, M.H., Laki, A.S. Experimental Analysis of Secondary Gas Injection Strategies. *Petrol. Sci. Technol.*, 31(8), 797–802, 2013a.
- Heidari, P., Kharrat, R., Alizadeh, N., Ghazanfari, M.H. A Comparison of WAG and SWAG Processes: Laboratory and Simulation Studies. *Energy Sources, Part A: Recovery, Utilization, and Environmental Effects*, 35(23), 2225–2232, 2013b.
- Heller, J.P., Lien, C.L., Kuntamukkula, M.S. Foamlike Dispersions for Mobility Control in CO₂ Floods. *SPE J.*, 25(4), 603–613, 1985.

- Holm, L. W. CO₂ Flooding: Its Time Has Come. *J. Petrol. Technol.*, 34(12), 2739–2745, 1982.
- Holm, L.W., Josendal, V.A. Mechanisms of Oil Displacement by Carbon Dioxide. *J. Petrol. Technol.*, 26(12), 1427–1438, 1974.
- Honarpour, M.M., Nagarajan, N.R., Grijalba, A.C., Valle, M., Adesoye, K. Rock-Fluid Characterization for Miscible CO₂ Injection: Residual Oil Zone, Seminole Field, Permian Basin. Paper SPE 133089, SPE Annual Technical Conference and Exhibition, Florence, Italy, September 19–22, 2010.
- Huang, E.T.S., Tracht, J.H. The Displacement of Residual Oil by Carbon Dioxide. Paper SPE 4735, SPE Improved Oil Recovery Symposium, Tulsa, OK, April 22–24, 1974.
- Irving, J.B. *Viscosity of Binary Liquid Mixtures: A Survey of Mixture Equations*. NEL Report No. 630, National Engineering Lab: Glasgow, Scotland, 1977.
- Jamshidnezhad, M. Oil Recovery by Miscible SWAG Injection. Paper SPE 115710, SPE Russian Oil and Gas Technical Conference and Exhibition, Moscow, Russia, October 28–30, 2008.
- Juanes, R., Blunt, M.J. Impact of Viscous Fingering on the Prediction of Optimum WAG Ratio. *SPE J.*, 12(4), 486–495, 2007.
- Kim, J., Dong, Y., Rossen, W.R. Steady-State Flow Behavior of CO₂ Foam. *SPE J.*, 10(4), 405–415, 2005.
- Koperna, G.J., Melzer, L.S., Kuuskraa, V.A. Recovery of Oil Resources from the Residual and Transitional Oil Zones of the Permian Basin. Paper SPE 102972, SPE Annual Technical Conference and Exhibition, San Antonio, TX, September 24–27, 2006.

- Kulkarni, M.M., Rao, D.N. Experimental Investigation of Miscible and Immiscible Water-Alternating-Gas (WAG) Process Performance. *J. Petrol. Sci. Eng.*, 48(1), 1–20, 2005.
- Kuuskræa, V.A. QC Updates Carbon Dioxide Projects in OGJ's Enhanced Oil Recovery Survey. *Oil Gas J.*, 110(7), 72–77, 2012.
- Kuuskræa, V.A., Godec, M.L., Dipietro, P. CO₂ Utilization from “Next Generation” CO₂ Enhanced Oil Recovery Technology. *Energy Procedia*, 37(1), 6854–6866, 2013.
- Lin, E.C., Huang, E.T. The Effect of Rock Wettability on Water Blocking During Miscible Displacement. *SPE Res. Eng.*, 5(2), 205–212, 1990.
- Ma, T.D., Rugen, J.A., Stoitsits, R.F., Voungren, G.K. Simultaneous Water and Gas Injection Pilot at the Kuparuk River Field, Reservoir Impact. Paper SPE 30726, SPE Annual Technical Conference and Exhibition, Dallas, TX, October 22–25, 1995.
- McDow, N., Kent, D. Depositional Environments, Lithofacies and Reservoir Distribution of the Mississippian Midale Beds in the Tatagwa Neptune–Colgate Area of Southeastern Saskatchewan. Paper PETSOC SS-93-11, Technical Meeting/Petroleum Conference of the South Saskatchewan Section, Regina, Saskatchewan, October 18–20, 1993.
- Melzer, L.S., Koperna, G.J., Kuuskræa, V.A. The Origin and Resource Potential of Residual Oil Zones. Paper SPE 102964, SPE Annual Technical Conference and Exhibition, San Antonio, TX, September 24–27, 2006.
- Moghadasi, J., Müller-Steinhagen, H., Jamialahmadi, M., Sharif, A. Theoretical and Experimental Study of Particle Movement and Deposition in Porous Media During Water Injection. *J. Petrol. Sci. Eng.*, 43(3), 163–181, 2004.

- Monger, T.G., Coma, J.M. A laboratory and Field Evaluation of the CO₂ Huff 'n' Puff Process for Light-Oil Recovery. *SPE Res. Eng.*, 3(4), 1168–1176, 1988.
- Moritis, G. EOR Continues to Unlock Oil Resources. *Oil Gas J.*, 102(14), 49–52, 2004.
- Moritis, G. Special Report: EOR/Heavy Oil Survey, *Oil Gas J.*, 104(17), 37–57, 2006.
- Nobakht, M., Moghadam, S., Gu, Y. Determination of CO₂ Minimum Miscibility Pressure from the Measured and Predicted Equilibrium Interfacial Tensions. *Ind. Eng. Chem. Res.*, 47(22), 8918–8925, 2008.
- Orr, F.M., Heller, J.P., Taber, J.J. Carbon Dioxide Flooding for Enhanced Oil Recovery: Promise and Problems. *J. Am. Oil Chem. Soc.*, 59(10), 810A–817A, 1982.
- Peng, D.Y., Robinson, D.B. A New Two-Constant Equation of State. *Ind. Eng. Chem. Fundam.*, 15(1), 59–64, 1976.
- Poole, E.S. Evaluation and Implementation of CO₂ Injection at the Dollarhide Devonian Unit. Paper SPE 17277, Permian Basin Oil and Gas Recovery Conference, Midland, TX, March 10–11, 1988.
- Pyo, K., Damian-Diaz, N., Powell, M., Van Nieuwkerk, J. CO₂ Flooding in Joffre Viking Pool. Paper PETSOC 2003-109, Canadian International Petroleum Conference, Calgary, Alberta, June 10–12, 2003.
- Quale, E.A., Crapez, B., Stensen, J.A., Berge, L.I. SWAG Injection on the Siri Field—An Optimized Injection System for Less Cost. Paper SPE 65165, SPE European Petroleum Conference, Paris, France, October 24–25, 2000.
- Rao, D.N. A New Technique of Vanishing Interfacial Tension for Miscibility Determination. *Fluid Phase Equilibria*, 139(1), 311–324, 1997.

- Rao, D.N., Lee, J.I. Application of the New Vanishing Interfacial Tension Technique to Evaluate Miscibility Conditions for the Terra Nova Offshore Project. *J. Petrol. Sci. Eng.*, 35(3&4), 247–262, 2002.
- Riazi, M., Sohrabi, M., Jamiolahmady, M. Experimental Study of Pore-Scale Mechanisms of Carbonated Water Injection. *Transport Porous Media*, 86(1), 73–86, 2011.
- Robie, D.R., Roedell, J.W., Wackowski, R.K. Field Trial of Simultaneous Injection of CO₂ and Water, Rangely Weber Sand Unit, Colorado. Paper SPE 29521, SPE Production Operation Symposium, Oklahoma City, OK, April 2–4, 1995.
- Rojas, G.A., Farouq Ali, S.M. Dynamics of Subcritical CO₂/Brine Floods for Heavy-Oil Recovery. *SPE Res. Eng.*, 3(1), 35–44, 1988.
- Schechter, D.S., Grigg, R., Guo, B., Schneider, B. Wellman Unit CO₂ Flood: Reservoir Pressure Reduction and Flooding the Water/Oil. Paper SPE 48948, SPE Annual Technical Conference and Exhibition, New Orleans, LA, September 27–30, 1998.
- Shetty, S., Hughes, R.G., Afonja, G. Experimental Evaluation of Simultaneous Water and Gas Injection Using Carbon Dioxide. Paper SPE 169690, SPE EOR Conference at Oil and Gas West Asia, Muscat, Oman, March 31–April 2, 2014.
- Shyeh-Yung, J-G.J. Mechanisms of Miscible Oil Recovery: Effects of Pressure on Miscible and Near-Miscible Displacements of Oil by Carbon Dioxide. Paper SPE 22651, SPE Annual Technical Conference and Exhibition, Dallas, TX, October 6–9, 1991.

- Siagian, U.W.R., Grigg, R.B. The Extraction of Hydrocarbons from Crude Oil by High Pressure CO₂. Paper SPE 39684, SPE/DOE Improved Oil Recovery Symposium, Tulsa, OK, April 19–22, 1998.
- Sohrabi, M., Danesh, A., Jamiolahmady, M. Visualisation of Residual Oil Recovery by Near-Miscible Gas and SWAG Injection Using High-Pressure Micromodels. *Transport Porous Media*, 72(3), 351–367, 2008.
- Sohrabi, M., Fatemi, S.M. Experimental Investigation of Oil Recovery by Different Injection Scenarios under Low Oil/Gas IFT and Mixed-Wet Condition: Water-Flood, Gas Injection, WAG and SWAG Injection. Paper SPE 161074, Abu Dhabi International Petroleum Conference and Exhibition, Abu Dhabi, UAE, November 11–14, 2012.
- Sohrabi, M., Kechut, N.I., Riazi, M., Jamiolahmady, M., Ireland, S., Robertson, G. Coreflooding Studies to Investigate the Potential of Carbonated Water Injection as an Injection Strategy for Improved Oil Recovery and CO₂ Storage. *Transport Porous Media*, 91(1), 101–121, 2012.
- Song, C., Yang, D. Performance Evaluation of CO₂ Huff-n-Puff Processes in Tight Oil Formations. Paper SPE 167217, Unconventional Resources Conference Canada, Calgary, Alberta, November 5–7, 2013.
- Stephenson, D.J., Graham, A.G., Luhning, R.W. Mobility Control Experience in the Joffre Viking Miscible CO₂ Flood. *SPE Res. Eng.*, 8(3), 183–188, 1993.
- Stone, H.L. A Simultaneous Water and Gas Flood Design with Extraordinary Vertical Gas Sweep. Paper SPE 91724, SPE International Petroleum Conference in Mexico, Puebla Pue., Mexico, November 7–9, 2004.

- Tiffin, D.L., Yellig, W.F. Effects of Mobile Water on Multiple-Contact Miscible Gas Displacements. *SPE J.*, 23(3), 447–455, 1983.
- Walker, J.W., Turner, J.L. Performance of Seeligson Zone 20B-07 Enriched-Gas-Drive Project. *J. Petrol. Technol.*, 20(4), 369–373, 1968.
- Wang, X., Gu, Y. Oil Recovery and Permeability Reduction of a Tight Sandstone Reservoir in Immiscible and Miscible CO₂ Flooding Processes. *Ind. Eng. Chem. Res.*, 50(4), 2388–2399, 2011.
- Wang, G.C. A Study of Crude Oil Composition during CO₂ Extraction Process. Paper SPE 15085, SPE California Regional Meeting, Oakland, CA, April 2–4, 1986.
- Warner, Jr., H.R. An Evaluation of Miscible CO₂ Flooding in Waterflooded Sandstone Reservoirs. *J. Petrol. Technol.*, 29(10), 1339–1347, 1977.
- Willhite, G.P. *Waterflooding*, Textbook Series, Vol. 3, SPE, Richardson, TX, 1986.
- Wu, R.S., Batycky J.P. Evaluation of Miscibility from Slim Tube Tests. *J. Can. Petrol. Technol.*, 29(6), 63–70, 1990.
- Yang, D., Gu, Y. Interfacial Interactions Between Crude Oil and CO₂ Under Reservoir Conditions. *Petrol. Sci. Technol.*, 23(9&10), 1099–1112, 2005.
- Yener, M.E., Kashulines, P., Rizvi, S.S., Harriott, P. Viscosity Measurement and Modeling of Lipid–Supercritical Carbon Dioxide Mixtures. *J. Supercrit. Fluids*, 11(3), 151–162, 1998.
- Yu, J., Liu, N., Li, L., Lee, R.L. Generation of Nanoparticle-Stabilized Supercritical CO₂ Foams. Paper CMTC 150849, Carbon Management Technology Conference, Orlando, FL, February 7–9, 2012.

Zhang, S., She, Y., Gu, Y. Evaluation of Polymers as Direct Thickeners for CO₂ Enhanced Oil Recovery, *J. Chem. Eng. Data*, 56(4), 1069–1079, 2011.

Zhang, Y.P., Sayegh, S.G., Huang, S., Dong, M. Laboratory Investigation of Enhanced Light-Oil Recovery by CO₂/Flue Gas Huff-n-Puff Process. *J. Can. Petrol. Technol.*, 45(2), 24–32, 2006.

APPENDIX A

Safe Operating Procedure for Coreflood Tests

Student Name: Yanbin Gong	Academic Supervisor: Dr. Peter Gu
Activity/Experiment: High-Pressure Coreflood Test	
Equipment Specifications / Manufacturer Guidelines: 100 DX syringe pump: Capacity: 100 ml Flow range (ml/min): 0.00001–50 Flow Accuracy: 0.3% of set point Pressure Range (psi): 10–10,000 Standard Pressure Accuracy: 0.5% FS Standard Temperature Range: 5–40 °C Ambient Power: 100 Vac, 117 Vac, 234 Vac, 50/60 Hz Dimensions: Height :103 cm (40.5 in), Width: 27 cm (10.6 in), Depth: 47 cm (18.5 in) 260 DX syringe pump: Capacity: 260 ml Flow range (ml/min): 0.001–107 Flow Accuracy: 0.5% of set point Pressure Range (psi): 10–7,500 Standard Pressure Accuracy: 0.5% FS Standard Temperature Range: 5–40 °C Ambient Power: 100 Vac, 117 Vac, 234 Vac, 50/60 Hz Dimensions: Height :103 cm (40.5 in), Width: 27 cm (10.6 in), Depth: 47 cm (18.5 in) High-pressure cylinder (500 ml): Capacity: 500 ml Pressure Range (psi): 10–10,000	

Standard Temperature Range: 5–200°C Ambient Coreholder Maximum working Pressure (psi): 20,000 Maximum working Temperature: 315 °C		
Steps:	Hazards:	Safe Work Practices/Mitigation Strategies:
1. Clean core samples by using the Dean–Stark extractor for about one week	Three chemicals, i.e., toluene, methanol, and chloroform are used to clean the core plugs, They are highly toxic and volatile	<ul style="list-style-type: none"> • Do task inside a fume hood • Be careful when you pour these chemicals
2. Dry the core samples at 120 °C inside a lab oven for 10 hours	It might be a fire hazard due to the long-term heating	<ul style="list-style-type: none"> • Do it in the daytime and check it every hour • Always shut off the oven before leaving for the day
3. Place the cool downed core samples together with two distributors in series inside a shrinkable tube, and put them back to the lab oven for 1h at 120 °C	It might be a fire hazard	<ul style="list-style-type: none"> • Do it in the daytime and check it every hour • Always shut off the oven before leaving for the day
4. Place the core plugs into a rubber sleeve	None	<ul style="list-style-type: none"> • None
5. Assemble the rubber sleeve into a coreholder on a work bench	Coreholder is too heavy and could cause physical injury	<ul style="list-style-type: none"> • Wear the heavy-duty gloves and safety boots • Ask your classmates to help you to assemble the coreholder, if needed.
6. Connect the tubing before and after the coreholder	None	<ul style="list-style-type: none"> • None
7. Apply the overburden pressure of 3–5 MPa to the core samples	None	<ul style="list-style-type: none"> • None

8. Use the high pressure air to do the leakage test	High pressure air	<ul style="list-style-type: none"> • Keep your personal protective equipment (PPE) on all the time in the lab
9. Vacuum the coreholder by using a vacuum pump	Vacuum pump can produce a lot of heat during its working process, it might be a fire hazard	<ul style="list-style-type: none"> • Stop it for a while in every one hour • Keep the flammable materials away from the vacuum pump
10. Fill the oil, brine, and CO ₂ into three transfer cylinders	Cylinders are very heavy and could cause physical injury	<ul style="list-style-type: none"> • Wear the heavy-duty gloves and safety boots • Move any items away from your path before you move the transfer cylinders • Cart may be used to deliver these heavy transfer cylinders
11. Inject brine to measure the porosity and permeability of the core plugs	The whole system is under a high-pressure condition	<ul style="list-style-type: none"> • Keep you PPE on all the time in the lab • Ensure that the overburden pressure is 3–5 MPa higher than the injection pressure
12. Inject oil to achieve the connate water saturation	The whole system is under a high-pressure condition	<ul style="list-style-type: none"> • Keep you PPE on all the time in the lab • Ensure that the overburden pressure is 3–5 MPa higher than the injection pressure
13. Increase the BPR pressure to the preset production pressure	The whole system is under a high-pressure condition	<ul style="list-style-type: none"> • Keep you PPE in the lab • Gradually increase the BPR pressure to protect the BPR
14. Inject water or CO ₂ to displace the crude oil inside the coreholder	The whole system is under a high-pressure condition	<ul style="list-style-type: none"> • Ensure that the overburden pressure is 3–5 MPa higher than the injection pressure
15. Collect the produced oil by using an oil sample collector and measure the volume of produced gas by using a gas flow meter	Produced oil might spill	<ul style="list-style-type: none"> • Remember to change the oil sample collector before an overflow occur
16. Use a centrifuge to separate the produced oil and water, and record their volumes	None	<ul style="list-style-type: none"> • Place the centrifuge on a flat surface

APPENDIX B

Safe Operating Procedure for Viscosity Measurement with the Capillary Viscometer

Student Name: Yanbin Gong		Academic Supervisor: Dr. Yongan (Peter) Gu
Activity/Experiment: Viscosity measurement of a mixture consisting of two immiscible fluids		
Equipment Specifications / Manufacturer Guidelines: 100 DX syringe pump; 260 DX syringe pump; High-pressure cylinder (500 ml); High temperature-high pressure (HTHP) capillary viscometer: Tubing Size: Diameter: 1/16 in. O.D.×0.006 in. I.D., Length: 23 ft Working Pressure (psi): 15,000 Material: 316 SS		
Steps:	Hazards:	Safe Work Practices/Mitigation Strategies:
1. Find two high-pressure cylinders and fill each of them with one fluid need to be tested	The cylinders are heavy metal hazards	<ul style="list-style-type: none"> • Wear steel-toed boots • Wear heavy-duty work gloves when moving the cylinders • Put on the lab coat
2. Clean the capillary viscometer thoroughly with kerosene and ethanol in sequence	Ethanol evaporates easily and can be inhalation hazard	<ul style="list-style-type: none"> • Conduct in the fume hood
3. Dry the capillary viscometer by using pressurized air	None	<ul style="list-style-type: none"> • None
4. Put the capillary viscometer in the oven	None	<ul style="list-style-type: none"> • None

5. Connect all the cylinders, tubing, back-pressure regulator (BPR), and syringe pumps together	None	<ul style="list-style-type: none"> • None
6. Wrap the two high-pressure cylinders with heating tapes and connect the heating tapes to a temperature controller	None	<ul style="list-style-type: none"> • None
7. Turn on the temperature controller and set the target value to the desire temperature	Heating tape gets hot, if there are any hydrocarbons nearby, there could be a fire hazard	<ul style="list-style-type: none"> • Ensure you are able to stay nearby while the heating tape is running • Clean any oil stain around the cylinders
8. Turn on the oven and set the target value to the desire temperature	Oven gets hot, if there are any flammable items inside, there could be a fire hazard	<ul style="list-style-type: none"> • Ensure you are able to stay nearby while the oven is running • Clean any oil stain inside the oven
9. Co-inject the two immiscible fluids through the capillary viscometer by using two syringe pumps	None	<ul style="list-style-type: none"> • None
10. Increase the BPR pressure gradually to the desired pressure by using another syringe pump	The pressure of the whole system becomes high and the high pressure gas cylinder could be a explosive hazard	<ul style="list-style-type: none"> • Ensure eye goggles are proper wore • Change O-ring inside the gas cylinder after each test
11. Set the two injection pumps at different volume injection rates	The whole system is in HTHP conditions	<ul style="list-style-type: none"> • Must keep your PPE on the entire time
12. Read the pressures at two ends of the capillary viscometer	The whole system is in HTHP conditions	<ul style="list-style-type: none"> • Must keep your PPE on the entire time
13. When the experiments are done, decrease the BPR pressure to the atmosphere pressure by controlling the syringe pump	Fluids will be spouted if the BPR pressure is de ceased too fast	<ul style="list-style-type: none"> • Must keep your PPE on the entire time • Ensure the BPR pressure-decreasing rate is slow (e.g., 3 MPa/h)

14. Turn off the temperature controller and oven and unplug them	Oven and cylinders are still hot	<ul style="list-style-type: none"> • Must keep your PPE on the entire time
15. Turn off all three syringe pumps and unplug them	None	<ul style="list-style-type: none"> • None
16. Leave the oven and fluid cylinders to cool down	Oven and cylinders are still hot	<ul style="list-style-type: none"> • Must keep your PPE on the entire time
17. Disconnect the cylinders, viscometer, BPR, and syringe pumps	Fluids could be spilled out	<ul style="list-style-type: none"> • Must keep your PPE on the entire time • Clean any spilled fluids and ensure around area is clean